Field-test of nacelle-based lidar to explore its applications for Vattenfall as wind park operator

MASTER OF SCIENCE THESIS

Stefan Goossens

May 18, 2015

Stefan Goossens: *Field-test of nacelle-based lidar to explore its applications for Vattenfall as wind park operator,* Master of Science Thesis, © May 18, 2015

Field-test of nacelle-based lidar to explore its applications for Vattenfall as wind park operator

MASTER OF SCIENCE THESIS

For obtaining the degree of Master of Science in Aerospace Engineering
at Delft University of Technology

SUPERVISORS:

G.J.W. van Bussel (Delft University of Technology)
W.A.A.M. Bierbooms (Delft University of Technology)
J.P. Coelingh (Vattenfall)

Stefan Goossens

May 18, 2015 – version 2.5

Wind Energy Research Group, Faculty of Aerospace Engineering, Delft University of Technology
Vattenfall

Stefan Goossens: *Field-test of nacelle-based lidar to explore its applications for Vattenfall as wind park operator,* Master of Science Thesis, © May 18, 2015

ABSTRACT

To gain more insight in the applications of nacelle-based lidar and their benefits to Vattenfall as operator, a measurement campaign was conducted at wind park Slufterdam West. More specifically, a Wind Iris was installed on the nacelle of the most southern wind turbine (type GE 1.5s) and a sodar of type AQ500 was installed 235m to the southeast of this turbine. The Wind Iris proved to be a useful instrument for measurement of the power curve and mean yaw misalignment. The former was found to be in accordance with the contracted power curve and the latter turned out to be 1.5 degrees. In the wind regime where it is most relevant to the power curve (4–13 m/s), yaw misalignment was found to have no clear relationship with rotor speed and wind speed. Two methods were used to investigate the impact of yaw misalignment on the power curve, but no definitive conclusions could be drawn. Moreover, the Wind Iris was found to be a useful tool for investigating the blockage effect and results were in accordance with theory. A financial case study was carried out to evaluate implementation of the Wind Iris at Slufterdam. However, since there is no evidence that the turbines have yaw misalignment nor that small yaw misalignment is harming the power curve, implementation is currently not recommended. However, if the impact of yaw misalignment on the power curve can be quantified accurately, implementation can be financially viable.

ACKNOWLEDGMENTS

This thesis would not have been possible without the support from several people and organizations. First of all I would like to thank Jan Coelingh for providing this graduation opportunity and the supervision throughout the project. I am also very grateful for the frequent feedback and many ideas from Wim Bierbooms. Thanks to Jan and Wim, this project has been a very valuable and pleasant experience to me. I would also like to thank Gerard van Bussel for providing input and being chairman on the graduation committee. Moreover, I am grateful to Stephan de Roode for also participating in the committee.

I would also like to thank the people of Oldbaum Services for providing the Wind Iris and their technical support, especially from Erik Brown. The same goes for all Nuon colleagues in Amsterdam, especially Jorn Goldenbeld, Stathis Koutoulakos and all members of the Vattenfall Wind Resource team.

Finally I would like to extend my gratitude to my friends and family for the fun times, support and love.

CONTENTS

LIST OF FIGURES

1 INTRODUCTION

Meeting energy demand in a sustainable manner is a contemporary global challenge, and described as part of the 7th Millennium Development Goals to ensure environmental sustainability[25]. Wind energy might be part of the solution[38], and is topic of international academic research[46].

The market share of wind energy is related to many factors, including politics, social acceptance and financial feasibility. In light of reducing the Levelised Energy Cost (LEC) generated from wind energy, power company Vattenfall is continuously looking for new ways of monitoring and improving wind turbine yield. Recent publications have shown nacelle-based lidar to be a valuable tool for research[54][65][67], capturing the interest of Vattenfall's Wind Resource team. Specifically, they are interested in what a nacelle-based lidar can contribute to Vattenfall as operator, which became the central theme of this thesis.

To form an impression of the possibilities of nacelle-based lidar and the latest developments in the field, a literature review was conducted. The findings are reported in a separate document, but they are also summarized in Chapter 2. The literature review was concluded by five research objectives, which are discussed in Chapter 3. The introductory chapters are concluded by Chapter 4, which discusses the specifications of the wind turbine, site, measurement campaigns and instrumentation.

Consequently, Part i of this thesis addresses the first measurement campaign, comprising a sodar on wind park Slufterdam from April 2011 to April 2012. Measurements with this sodar, the nearby KNMI station at Hoek van Holland, and turbine data are used to get an initial idea of site conditions, wind speed measurement, power curve measurement and yaw misalignment.

Part ii discusses the second measurement campaign, comprising a sodar and nacelle-based lidar at wind park Slufterdam from September 2014 to January 2015. Part ii addresses the research objectives of Chapter 3, with topics including validation, power curve measurement, turbine gains and blockage.

In Part iii the conclusions and recommendations following from this thesis are discussed. These include answers to the research objectives and suggestions for further research.

Part iv contains the appendices of this thesis, including a derivation of lidar equations and a simulation of measurements to analyze measurement accuracy.

2 LITERATURE REVIEW

Prior to this thesis, a literature review was carried out and reported upon in a separate document, forming the foundation for this thesis. In the literature review there was a focus on the applications of lidar in the field of wind energy. By reviewing the latest articles, research opportunities have revealed themselves which were translated into research objectives for this thesis.

In short, the literature review revealed that lidar has been used extensively in wind energy research, especially since around 2006[20][57]. Nacelle-based lidar has been used successfully for power curve measurement[67], reduction of yaw error[15], wake research[61] and in feedforward controllers[63]. There is no consensus on the accuracy of lidar turbulence measurements[12][35][40][65], but researchers agree that it is a good tool for measuring averaged wind speed[65][67]. In Section 2.1 to Section 2.3, some aspects of the literature review are included.

The work following the literature review explores the use of forward-looking nacelle-based lidar (a *Wind Iris*) on one of the 1.5MW wind turbines of wind park Slufterdam in The Netherlands. The first goal is to independently determine the power curve using the Wind Iris and to what extend this instrument is appropriate in this process. Moreover, the blockage effect (i.e. deceleration of wind in front of the turbine), yaw misalignment and (rotor speed dependent) wind vane calibration will also be explored. Finally, a case study is carried out to determine under which conditions implementation of nacelle-based lidar is financially feasible. These goals are elaborated further and listed in Chapter 3.

2.1 THE HISTORY OF LIDAR

Lidar is first mentioned in literature in 1963 by Goyer and Watson, shortly after the first working laser in 1960[39]. In the former article, lidar is explained to be an acronym for "LIght Detection And Ranging", considering it is a device combining the principles of laser and radar. Northend considers the lidar to be *"an extremely useful device [in] the family of meteorological instrumentation"*[45]. However, lidar not only proves to be useful in meteorology, but also in the fields of remote sensing, agriculture, archeology, law enforcement, military, mining, astronomy, robotics and more[11][28][50].

In 1967, Northend recognizes the merit of lidar in meteorology, because it uses electromagnetic radiation in the UV, visible and infrared spectra, whereas radar uses radiation at much longer wavelengths, namely the microwave region[45]. This much shorter wavelength of lidar facilitates significantly more backscatter in atmospheric phenomena, hence making them more visible to the remote sensing device.

The 1970's and 1980's saw the introduction of accurate positioning systems such as global positioning systems (GPS), inertial measurement units (IMU), and inertial navigation systems (INS). These systems facilitated the introduction of airborne lidar, where a lidar on an airplane scans the Earth's surface for topographic data.[11]

Despite greater backscatter of lidar systems, currently radar is used to detect rain, because of their larger range[60]. In The Netherlands, two radars are used, one in De Bilt, and the other in Den Helder. Each radar has a range of around 150km and detects the intensity of the rain from the amount of backscatter: more backscatter means more precipitation. However, these radar systems have problems identifying drizzle, because these particles hardly reflect the relatively long wavelengths of the radar. Moreover, this type of precipitation is formed from low clouds, whereas the radar scans the clouds 1500m and up[19].

In 2013, Trombe et al. suggest the use of weather radars as the new eyes of wind farms[60]. Weather radars in The Netherlands have proven to be useful tools in detecting precipitation, and this is the key characteristic used by Trombe et al.. Precipitation namely has a strong correlation with wind fluctuation, i.e. if the radar detects precipitation, a change in wind can be expected. In this application the advantage of radar over lidar is the extended range, hence better detection of large meteorological phenomena such as weather fronts[60].

The appeal of lidar as a means to measure wind was reaffirmed in 1996 by Frehlich[16]. But it was not until recent years that lidar has attracted significant attention from wind energy researchers [29] [55] [62] [63] [65].

2.2 POSSIBILITIES AND LIMITATIONS

Lidar has all sorts of applications, as discussed in Section 2.1. However, in the field of wind energy, lidar has mostly been applied to determine yaw error[65], power performance (through power curve measurement)[65], wind shear[44], wind veer[44], perform wake measurements [5] and site assessment[34][52].

The main advantage of lidar is the ability to measure wind velocity remotely. This means lidar does not interfere with the flow at the measurement location, like in the case of cup anemometers and sonic anemometers. It does, however, interfere with the flow at the location of the device itself. This is why Wagner et al. suggest that nacelle-based lidar should only be applied on turbines *"of sufficient size that the nacelle mounted lidar does not significantly affect the flow through the turbine's rotor and around the nacelle and hence does not affect the wind turbine's performance."*[72]. This should not be an issue, since the turbine that is to be equipped with a nacelle-based lidar is a GE 1.5 S. This turbine has a hub height of 64.7m, rotor diameter of 70.5m, and a rated power of 1.5MW.

Another advantage of lidar over cup anemometers is the lack of inertial effects. Cup anemometers namely have to spin up and down before detecting a change in wind, causing a delay and a slight smoothing of the signal. However, this does not mean that lidar can measure turbulence accurately. In fact, a disadvantage of Doppler lidar is the spatial averaging, which occurs in order to determine the wind direction between two measuring points. Mann et al. conclude that investigated lidars (continuous wave and pulsed) cannot measure turbulence[40].

Another difference between lidar and cup anemometers is the point of measurement: cup anemometers measure the wind speed locally (i.e. at the position of the device), whereas lidar measures remotely (i.e. some distance away from the device). Currently ground-based lidar have a range of up to 20 km[34]. Weather radars, on the other hand, have a range up to 100km (X-band), between 200-300km (C-band) and beyond 450km (S-band)[60]. The KNMI weather radars in De Bilt and Den Helder are C-band, with a range of around 150 km[19].

2.3 APPLICATIONS

2.3.1 *Performance assessment: Power curve measurement*

An application of lidar in wind energy is performance assessment [14] [66] [69]. Considering the importance of accurate power curves to the operator, it is worthwhile to measure it. Power curves are typically based on the air density and hub height wind speed 2.5 rotor diameters in front of the turbine, which is the IEC standard[26]. However, the introduction of equivalent wind speed allows the electrical power to be determined more accurately than with a single point hub height wind speed[71]. This improved means of measuring the power curve namely takes the wind shear into account.

An example of a power curve made with help of a nacelle lidar is shown in Figure 1, where several distances from the hub have been used, although all at hub height[14]. This shows that the blockage effect (i.e. slowing of wind speed in front of the turbine) can be seen in the power curve and this means that the power curve should be based on the correct distance. It has been suggested that also the turbulence intensity should be taken into account when making power curves[21]. On a similar note, in 2014, Villanueva Lopez completed his masters thesis regarding factors influencing power curves, including shear and turbulence[64].

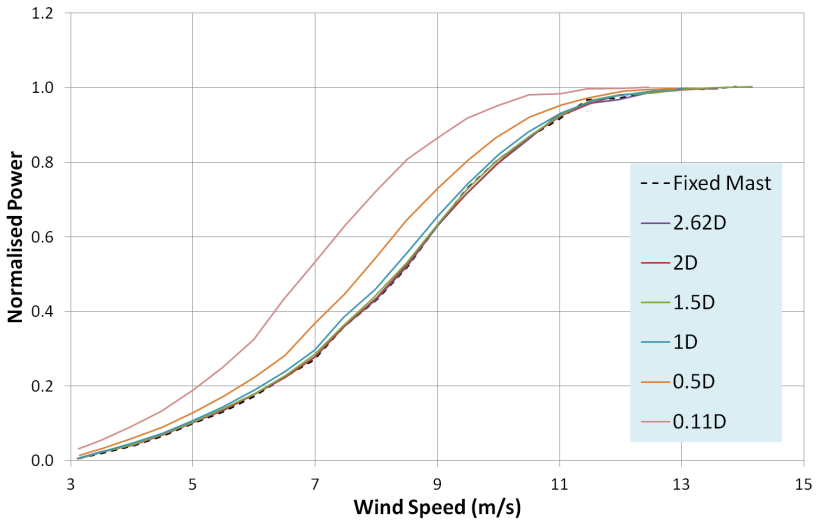

Figure 1: Power curves made using nacelle lidar and a met mast[14]

2.3.2 *Performance improvement: reduction of yaw error*

One of the crucial functions of a wind turbine is the ability to align itself with the wind. This allows the turbine to create the most electricity from the available wind. Any deviation from perfect alignment with the wind supposedly results in a loss of power, which is a key selling point for nacelle-based lidar.

The power loss due to yaw misalignment is discussed by Pedersen et al., who conclude that yaw and power are related by a $\cos ine^2$ of the angle[47][49], as shown in Figure 107[49]. Initially they expected a $\cos ine$ relationship, because the projected swept area is affected by yaw misalignment through a $\cos ine$, but this turns out to be an underestimation of the effect.

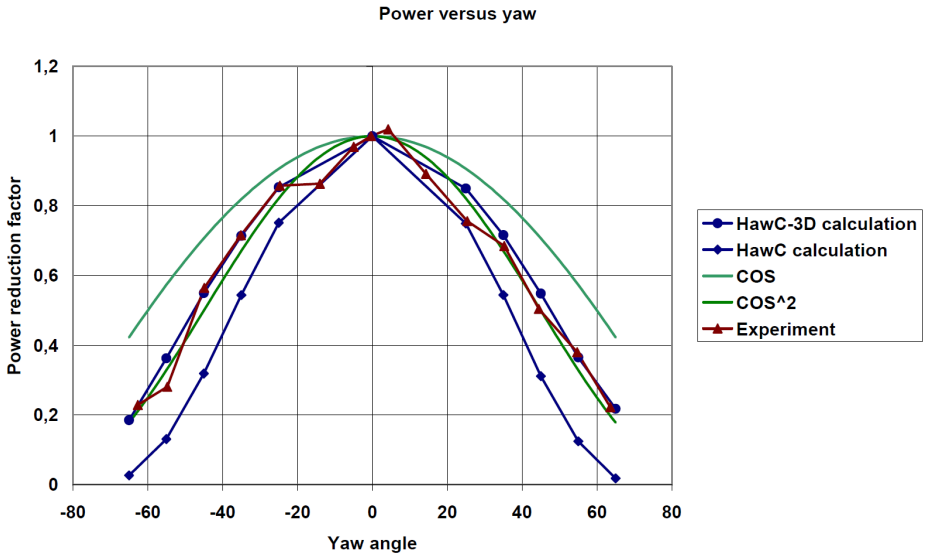

Figure 2: Relative power reduction as measured and simulated for a 75kW wind turbine at 8-9 m/s[49]

Power loss due to yaw misalignment is also discussed by Mikkelsen et al., with help of Equation 1.

$$P = \frac{1}{2} C_p A \rho U^3 \tag{1}$$

Unlike Pedersen et al., Mikkelsen et al. base their power loss estimation on the *rotor plane projected wind speed*, which is affected through a $cosine$ of the angle. This means that the power, however, is proportional to $cosine^3$, as opposed to the $cosine^2$ as found by Pedersen et al.. By assuming a 10° RMS (root mean square) yaw misalignment, a first order expansion can be made in Equation 2.

$$\begin{aligned} \overline{\cos(\theta_w)} &\approx 1 - \frac{1}{2}\overline{\theta_w^2} \\ \overline{\theta_w^2} &\approx \left(\pi \frac{10}{180}\right)^2 = 0.0305 \\ \overline{\cos(\theta_w)} &= 0.9848 \end{aligned} \tag{2}$$

Applying this to Equation 1 results in a power loss of 4.6% as shown in Equation 3[44][32]. In case of the $cosine^2$ relation, as suggested by Pedersen et al., this have been a 3.0% loss. It must be noted that these approximations only apply if the turbine operates below rated wind speed at all times. It is therefore not a good estimate of the loss in AEP.

$$\Delta P_{10° RMS} = 3\left(\frac{1}{2}\overline{\theta_w^2}\right) = 3 * 0.0152 = 0.0456 \tag{3}$$

Whether the relationship is $cosine^3$, $cosine^2$ or $cosine$ depends on the aeroelastic properties of the turbine, according to Fleming et al.[15]. They also mention two sources of yaw error: the first is that the wind direction changes more often than can be corrected for by the yaw controller. The second source of error is in the wind direction measurement, which is now typically done with a wind vane on the nacelle (i.e. in the wake of the blades). The second source is most easily addressed, since it requires little extra yaw motion. It could be done by either calibrating the existing system, or replacing it with a more accurate one[15].

In 2013, Kragh et al. report on their findings that the nacelle wind vane becomes more biased with higher rotor speeds, and derive a rotor-speed-dependent correction function. These findings are based on an empirical study with a research turbine and a nearby met mast[30]. Fleming et al. suggest that nacelle-based lidar is more suitable for the derivation of such correction functions, because they are turbine dependent and a lidar can be moved relatively easily from turbine to turbine. After determining the rotor-speed-dependent correction, power curves were created with the correction on and off, as shown in Figure 3. These result in a prediction of AEP increase of 2.4%[15]

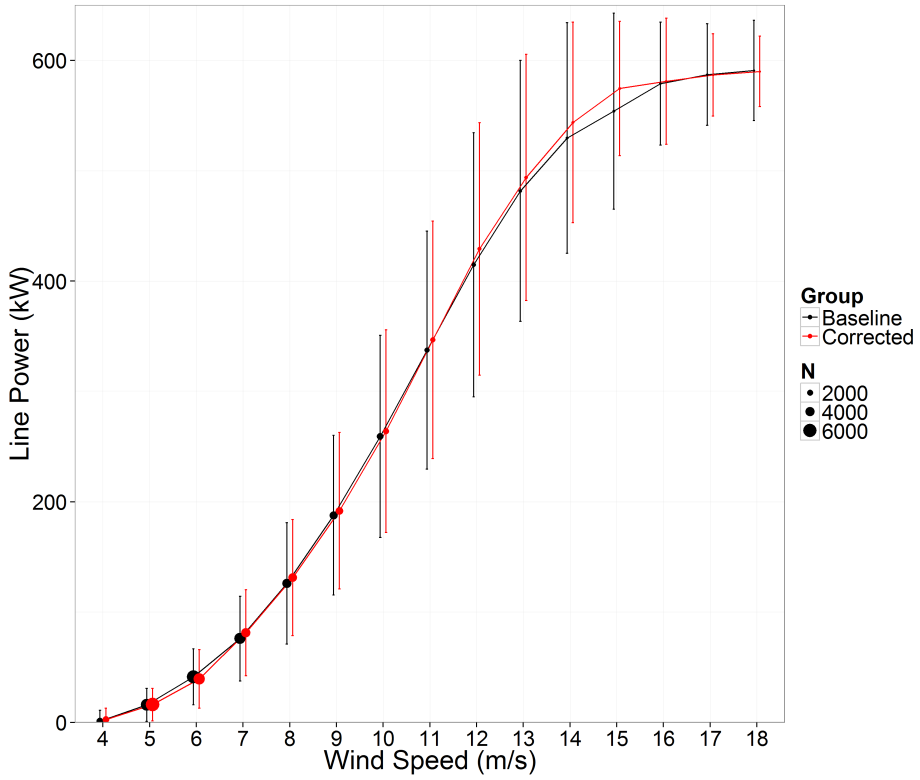

Figure 3: Comparison of power curves with and without lidar correction factor applied, using 10-s blocks. Points show mean while error bars indicate standard deviation. The size of the points indicates the number of samples in a given wind bin (N)[15]

Kragh and Hansen have also investigated the potential gain from reduced yaw error, and found an annual power loss due to yaw misalignment of approximately 0.2%[29]. In this recent study they have applied a met mast. However, in earlier work Kragh et al. have employed a spinner-based lidar to estimate the yaw error. By correlating data from the spinner-based lidar to that of a met-mast, it was found that the spinner-based lidar can determine the yaw error with a precision of a few degrees. When the method was applied to experimental data, an average yaw error of approximately 9° was found.

In case of complex terrain, it is also valuable to understand the behavior of turbines under flow inclination. If the turbine is located on an inclination, it will experience skewed inflow (wind with an upward/downward velocity component) as well as a yaw misalignment. Pedersen concludes that the AEP of inclined and flat airflow conditions can easily differ by more than 10%[47].

Besides the possibilities of reducing yaw misalignment with help of lidar aided feed-forward yaw controllers and lidar-aided calibration, it is also possible to reduce the yaw error with help of spinner-based anemometers. These are significantly cheaper and this application has already been illustrated in 2008 by Pedersen et al.[48]. These can be applied permanently in controllers, as well as temporarily for wind vane calibration with a dependence on rotor speed.

It must be noted that "average yaw misalignment" is a rather ambiguous term. If the yaw misalignment is averaged, it could be zero, even though the yaw is misaligned by $+10^\circ$ and -10° continuously. Averaging in this way gives insight in the *accuracy* of the yaw control, whereas averaging the absolute yaw misalignment gives insight in the *precision*. It is therefore worthwhile to take this into account and consider the RMS (root mean square) error, or consider the mean and standard deviation of the yaw misalignment.

Moreover, yaw control is associated with gyroscopic loads[42] and wear of the yaw bearing, which is why turbines typically yaw relatively slowly. Therefore a quick anticipation of incoming wind is not evident, even with a 10-20 s preview time associated with lidar[44]. In case of wind vane calibration this is also an issue: large wind turbines will often not be able to yaw as quickly as the wind.

2.3.3 *Wake research*

Various types of lidar can also be used to measure wind velocity in the wakes of wind turbines.[1][5][61]. As such, numerical simulations can be validated[1], and it has proven to be useful in gaining insight in wake meandering and wake expansion[5].

2.3.4 *Predictive controllers*

In recent years (since 2006[20], but mostly since 2012) a lot has been written about the application of lidar in controllers [7] [8] [9] [31] [53] [55] [63] [73] [74]. These all use upwind-looking lidar to anticipate the wind in order to help reduce loads on the tower and blades[53], improve power regulation[63], and reduce pitch activity[53]. Although *even the rough solution of the control problem provides good performance at low cost*[9], this technology is not yet applied in practice.

3

RESEARCH OBJECTIVES

The literature review was concluded by several research objectives, as listed below. These will be addressed in Chapter 13, Chapter 17, Chapter 18, Chapter 19 and Chapter 20 respectively. Some research objectives refer to literature, where a similar study has been conducted, or where this thesis could be seen as a follow-up.

1. Gain experience with the installation and operation of the Avent Wind Iris, as well as the collection and analysis of the data, considering that a good dataset is a prerequisite for further analysis.
2. Determine the power curve based on lidar[14] [21] [67] [69] [72].
3. Determine how much Slufterdam west 09 and the park can gain from the installation of a nacelle-based lidar.
    a) (Rotor speed dependent[15][30]) wind vane calibration[29][42].
    b) Determine if other turbines in the park can benefit from the installation of one nacelle-based lidar.
    c) Match yaw misalignment angle, power and wind speed to estimate the power loss due to yaw misalignment.
4. Estimate the blockage effect/compression zone in front of the turbine and compare to theory[14].
5. Determine under what conditions a nacelle-based lidar is financially feasible.

4 SPECIFICATIONS

This chapter discusses the specifications of the site and turbines under research, as well as the instrumentation used for measurements.

4.1 SITE AND TURBINE

The wind turbine that Vattenfall selected to place the nacelle-based lidar on is shown red in Figure 4. All turbines of Slufterdam West are property of Vattenfall, but the most southern turbine (turbine 9) was selected because there it faces southwest freely. This means that with the prevailing southwestern wind in The Netherlands, the Wind Iris will have an unimpeded view. With NE–NW wind, the lidar will allow for research in wake effects caused by the upwind turbines. The four southernmost turbines are shown in Figure 5.

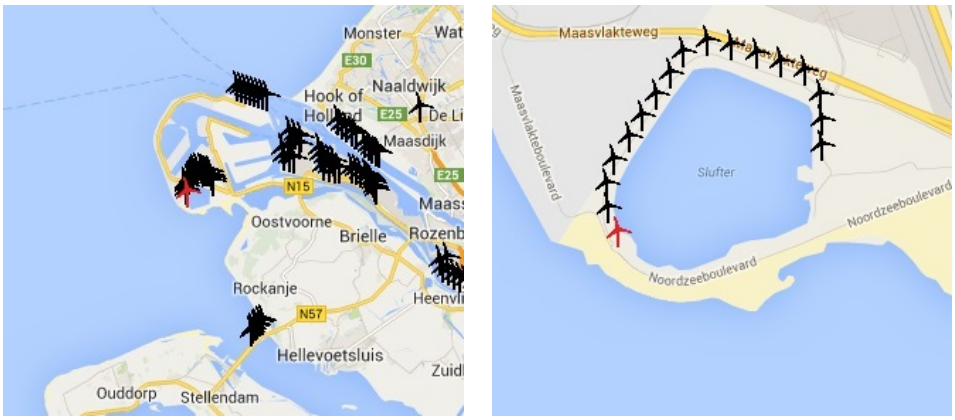

(a) (b)

Figure 4: The wind turbine selected by Vattenfall for nacelle-based lidar research[6]

Figure 5: Left to right: Wind Turbine 9, 8, 7 and 6 of Slufterdam West

The turbines on site are GE Wind 1.5s, with specifications shown in Table 1. They are variable speed full-span-pitch turbines.

Manufacturer, type	GE Wind 1.5S
Rated Power	1.5 MW
Hub height	64.7m
Rotor diameter D	70.5m
2.5D	176.25m
Nominal wind speed	approx. 12 m/s
Cut-in, cut-out, re-cut-in wind speed	4 m/s, 25 m/s, 19 m/s
Minimum, maximum rotor speed	11.1 rpm, 22.2 rpm
Yaw drive adjusting speed	approx 0.5°/s
Rotor shaft tilt angle	4°

Table 1: Specifications of the GE Wind 1.5s

The power curve as originally contracted is shown in Figure 6. This contract is currently expired, but it will still allow for comparison to the measured power curve.

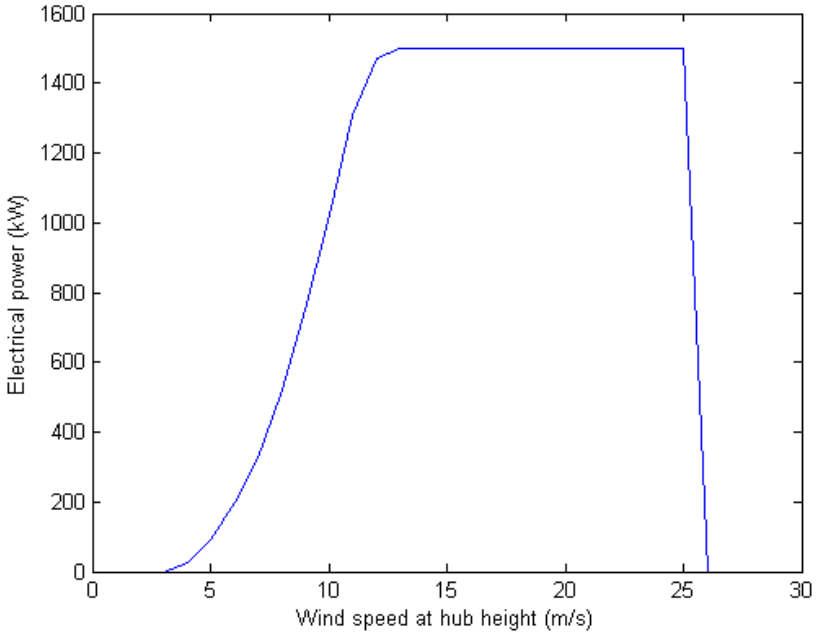

Figure 6: Power curve of the GE Wind 1.5s as originally warranted.

4.2 CAMPAIGN I

The first measurement campaign discussed in this report took place from April 2011 to April 2012. Data sources are a sodar on site (AQ-500 WindFinder), turbine data (from the scada system), and KNMI data (of station Hoek van Holland). The campaign is discussed in Part i of this report and gives a first impression of the site characteristics, anemometry, power curves, and yaw misalignment.

4.3 CAMPAIGN II

The second measurement campaign discussed in this thesis took place from 18 September 2014 until 26 January 2015. This campaign aims to address the research objectives as listed in Chapter 3.

Considering that the campaign involves data from four sources (nacelle-based lidar, turbine, sodar and KNMI data), an overview of the relevant events is shown in Table 2.

Event	Date
Installation Wind Iris	18 September 2014
Turbine in error until	23 September 2014
Installation Sodar	13 October 2014
Wind Iris power disconnected	10 December 2014
End of measurements Sodar	5 January 2015
Removal Wind Iris	26 January 2015

Table 2: Overview of events in second measurement campaign

4.3.1 *Nacelle-based lidar*

The Wind Iris (i.e. the nacelle-based lidar) was installed on 18 September 2014, although turbine 9 was in error until 23 sept 2014. Therefore the latter date is used as the start date of relevant measurements.

The data files of the Wind Iris show some missing data points in the beginning of December 2014, and communication with the Wind Iris was lost 10 December 2014. During the removal of the Wind Iris it was discovered that the power cable had been unplugged, possibly due to vibrations or maintenance in the nacelle. Whatever the cause of the unplugging was, the instrument did not take any measurements after 10 December. This means that for analyses involving both sodar and lidar, the period 14 October 2014 – 9 December 2014 is used, i.e. 56 days.

The Wind Iris is a 1.55µm pulsed Doppler lidar with two modes: ”accurate performance monitoring mode” and ”high frequency turbulence and control

mode". The ranges of these two modes are respectively 80–400m and 40–200m. Considering that the most interesting data is likely to be found between 2-4 rotor diameters (141-282m) away from the turbine[72], and the 2.5D point is 176.25m from the hub, the *accurate performance monitoring mode* is the most suitable and is selected. This 2.5D point is a recommendation by the IEC standards[26]. Data is logged in 1Hz as well as in 10min averages.

It must be noted that this nacelle-based lidar only allows for the computation of wind velocity and yaw misalignment (through measurement of the light frequencies and computation of the Doppler shift). This means that turbine data such as nacelle direction, rotor speed and power output are coupled afterwards.

4.3.2 *Sodar*

On 13 October 2014 a Sodar (once again an AQ-500 windfinder) was installed on site, allowing a direct comparison of measurements with the nacelle-based lidar. It is placed 235m to the southeast of turbine 9, so it can measure free stream when the wind is from the southwest, but is still relatively close to turbine 9. To determine the direction of the wind, the direction of the sodar must be known. Therefore the coordinates of two points in line with the sodar were determined with a hand-held GPS. These then allowed for the direction to be deduced, and this is 120 degrees from north. To check this result, two geographical reference points, also in line with the sodar were identified and located using Google maps. The points were determined to be 235m apart and at an angle of 124 degrees from north.

Part I

CAMPAIGN I

This part of the thesis discusses the first measurement campaign, which took place from April 2011 until April 2012. A sodar on site is used for resource assessment and a first look at anemometry, yaw misalignment and power curves.

5 DATA PROCESSING

Before the nacelle-based lidar (Wind Iris) was installed on September 18th 2014, sodar data collected at the site is analyzed. Measurements span 1 year, and were taken by the AQ-500 windfinder by AQSystem in the period April 2011 – April 2012. The dataset is combined with SCADA (supervisory control and data acquisition) data from the wind turbines at site, with parameters such as nacelle direction, active power and wind speed as measured by the anemometer on the turbine nacelle. Both the sodar and the scada data are 10-min averages, also logging date and time, which allowed the timeseries from both sources to be compared. Nearly all data processing is done with Matlab.

5.1 SODAR

The sodar at site takes measurements including wind speed and wind direction at numerous heights. It is ground-based and located close to turbine 8 and 9 of wind park Slufterdam West. The sodar and the two closest wind turbines are shown in Figure 7.

(a) AQ500 Windfinder (b) The closest wind turbines

Figure 7: The sodar on site

The sodar sometimes logs the value 9999, so this data is replaced by NaN. Windpro is used to manually identify measurement errors in wind speed and wind direction (36 datapoints in this case). These errors are marked and the datapoints are disabled. In the exported data the disabled datapoints are included, but are marked using the variable *SampleStatus* = 1. In Matlab these datapoints are then replaced by NaN.

The sodar and the two closest wind turbines (number 8 and 9) are shown on a map in Figure 8

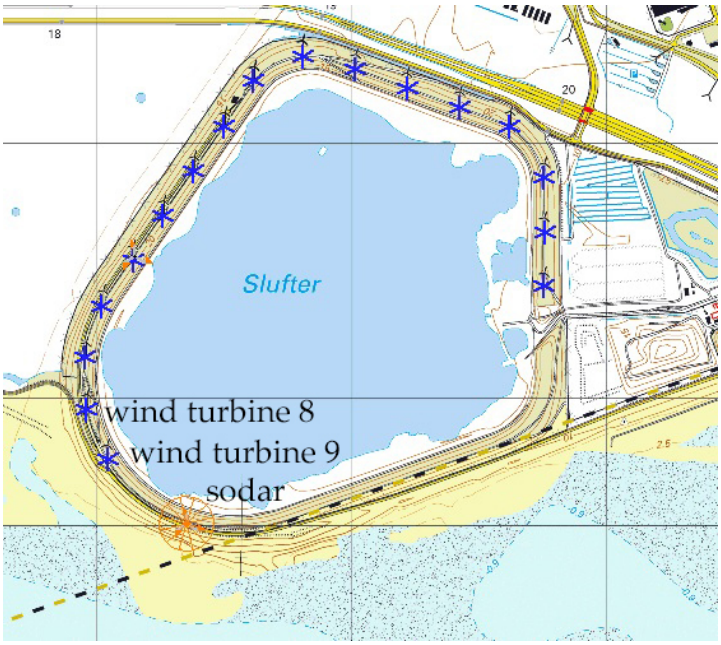

Figure 8: Map of wind turbines and sodar (campaign I) on the Slufterdam

5.2 SCADA

It seems there is a constant offset of around 53 degrees in nacelle direction of turbine 9. This can have several causes: For instance, the turbine's wind direction sensor (i.e. wind vane) could be offset by 53 degrees, causing turbine 9 to be constantly misaligned by 53 degrees. Another option is a problem with data logging, i.e. what is defined as direction 0. For the time being the latter is assumed and the data is offset by 53 degrees. This can be checked by comparing power curves: if the turbine is really offset by 53 degrees it must be significantly under-performing. A comparison in Chapter 9 reveals that this is not the case.

Moreover, there is also a time delay of 1 hour between the scada data and sodar data between April 2011 and October 2011, probably due to Daylight Saving Time. This offset was removed.

5.3 TIMESERIES AND FURTHER PROCESSING

Both sodar and SCADA data is put in Matlab timeseries objects. This allows for direction comparison of data from the two sets, considering they both logged the date and time.

However, the SCADA data and the synchronization step in Matlab creates interpolated data. This is replaced by NaN entries in the processing script.

Yaw misalignment is calculated by subtracting nacelle direction from wind direction (as detected by the sodar). An extra step is required in this process

since direction data jumps from 360 to 0 and back. This is solved with the following code:

```
for i=1:length(error.Data)
    if error.Data(i) < -180
        error.Data(i) = 360 + error.Data(i);
    elseif error.Data(i) > 180
        error.Data(i) = error.Data(i)-360;
    end
end
```

This method also makes sure that a yaw misalignment of 200 degrees, which corresponds to a yaw misalignment of -160 is registered as the latter. Consequently, the data can be plotted.

6 GENERAL SITE DATA

6.1 TEMPERATURE DISTRIBUTION

First, some general site characteristics are explored using solely the Sodar data (between April 2011 and April 2012), such as the temperature distribution, as shown in Figure 9. This figure shows an interesting pattern, almost like three normal distributions with different means combined. The temperature is focused around $-5°C$, $8°C$ and $17°C$, although mostly around $8°C$ and $17°C$. Note that the y axis should be interpreted as the number of 10 minute incidents. So for instance, between April 2011 and April 2012, the temperature was between $7°C$ and $8°C$ for 20000 minutes in total, i.e. around 14 days. This interesting pattern is also found when making a histogram of KNMI data of Hoek van Holland, a weather station 10km away.

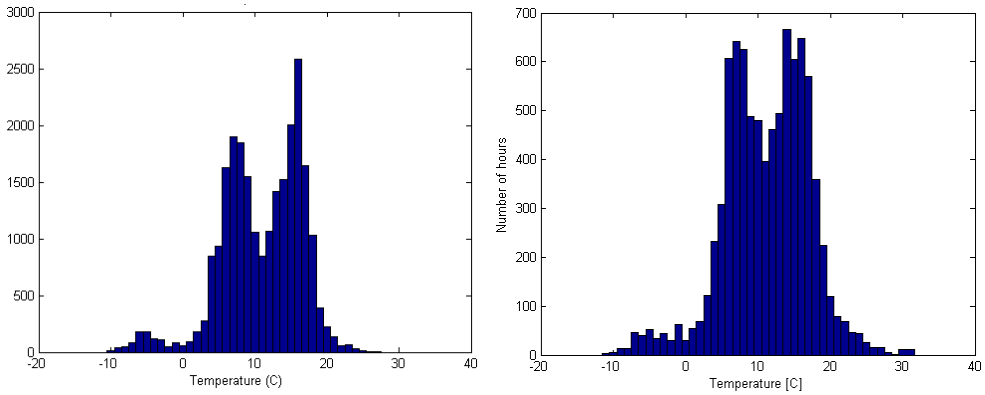

Figure 9: Temperature distribution as measured by Sodar (left) and by KNMI station at Hoek van Holland (right) in period April 2011 - April 2012

6.2 WIND DISTRIBUTION

Ten minute averages of the wind speed at 65m altitude are used to create a wind speed distribution, as shown in Figure 10. This is expected to follow a Weibull distribution, so a least squares fit was made with the method according to Windklimaat van Nederland from 1983[75], which was formed into a Matlab function by Bierbooms[3]. The least squares Weibull fit is found for $A = 9.42 m/s$ and $k = 2.0$, where the latter is typically found for coastal sites: onshore $k = 1.75$, coastal $k = 2.0$, offshore $k = 2.2$, at 10m height[75]. A fit was also made with WindPro (i.e. according to European Wind Atlas), resulting in $a = 9.50 m/s$ and $k = 2.05$, and both fits are also plotted in Figure 10.

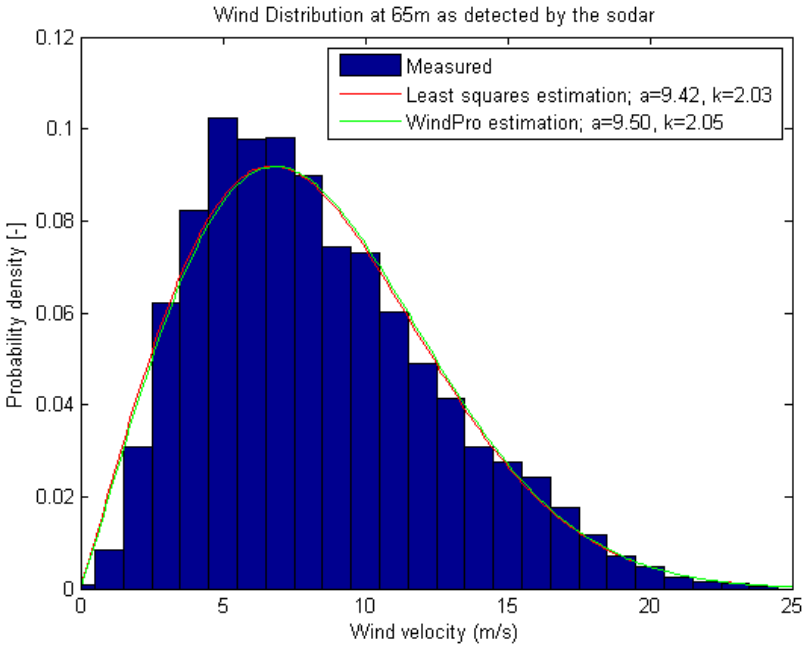

Figure 10: Wind speed distribution

To get an idea of how the Weibull parameters vary with height, the plots of Figure 11 were created. These show that the Weibull parameter "A" increases with height, since it is closely related to the mean wind speed. Parameter "k" is more or less constant with height.

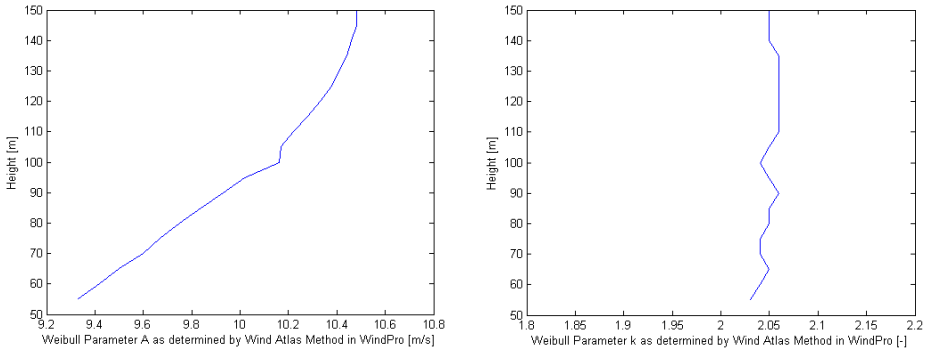

Figure 11: Weibull Parameters A and k as function of height as determined with the Wind Atlas Method in WindPro

Moreover, polar plots were created to get an idea of how the Weibull parameters vary with wind direction, as shown in Figure 12. This was done for heights 65m and 150m.

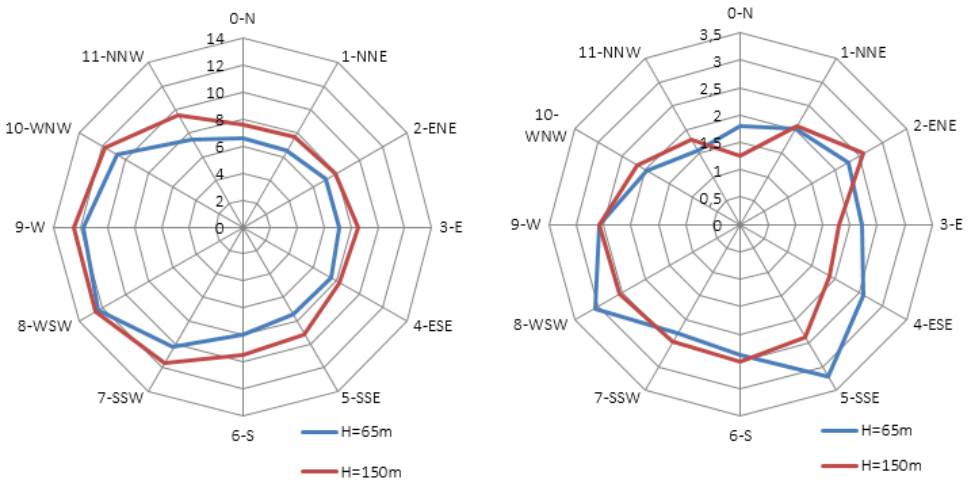

Figure 12: Weibull Parameters A (left) and k (right) at 65m and 150m as determined with the Wind Atlas Method in WindPro

6.3 WIND ROSE

Similarly, a wind rose can be made, showing the number of instances the wind was blowing from a certain direction. This is shown using 12 and 40 bins in Figure 13, of which the latter is plotted at the location of the sodar. These plots are based on data from 65m.

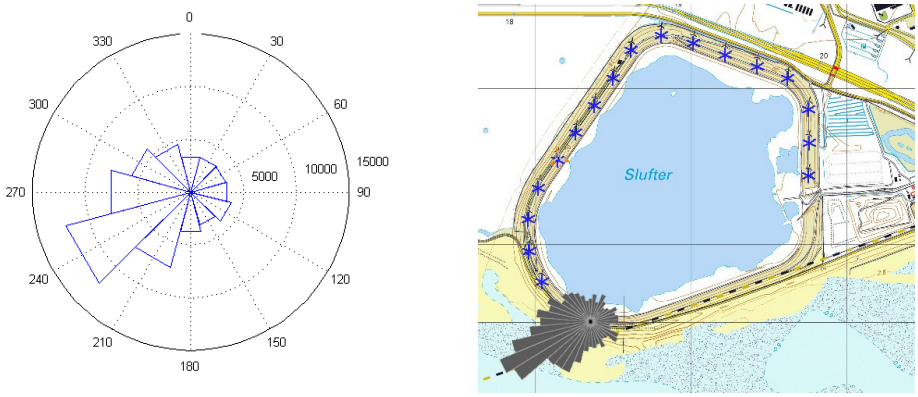

Figure 13: Wind rose, at 65m height

Similarly to the windrose, it is possible to show the mean wind speed per wind direction at 65m height. This is achieved in Matlab by first separating the wind speeds in 41 direction bins and then taking the average. This is shown in Figure 14, which shows for instance that if it the is blowing from the southwest, it had an average wind speed of 10 m/s. The figure closely resembles Figure 12, where Weibull parameter "A" is plotted for 12 wind directions. This is according to expectations, considering the relationship between mean wind speed "$\bar{u}$" and "A", as shown in Equation 4.

$$\bar{u} = A\Gamma\left(1 + \frac{1}{k}\right) \tag{4}$$

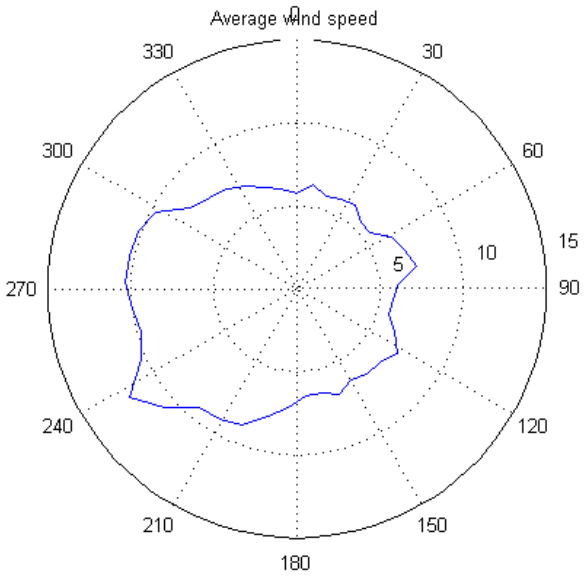

Figure 14: Polar plot of average wind speed at 65m height

7 ANEMOMETRY

A comparison is made between the sodar anemometry and nacelle-based cup anemometers on turbine 8 and turbine 9. This is done with three methods: using timeseries, scatter plots and histograms.

7.1 TIMESERIES

The most direct comparison is made by comparing signals as timeseries, as shown in Figure 15. This illustrates that there is a pretty good match between the three signals. The general trends are the same in all three plots, although there is some mismatch now and then.

Figure 15: Comparison of wind speed as measured by the sodar and nacelle cup anemometer of turbine 8 and 9

7.2 SCATTER PLOTS

The mismatch between the signals can be compared by making scatterplots, as shown in Figure 16 – Figure 18.

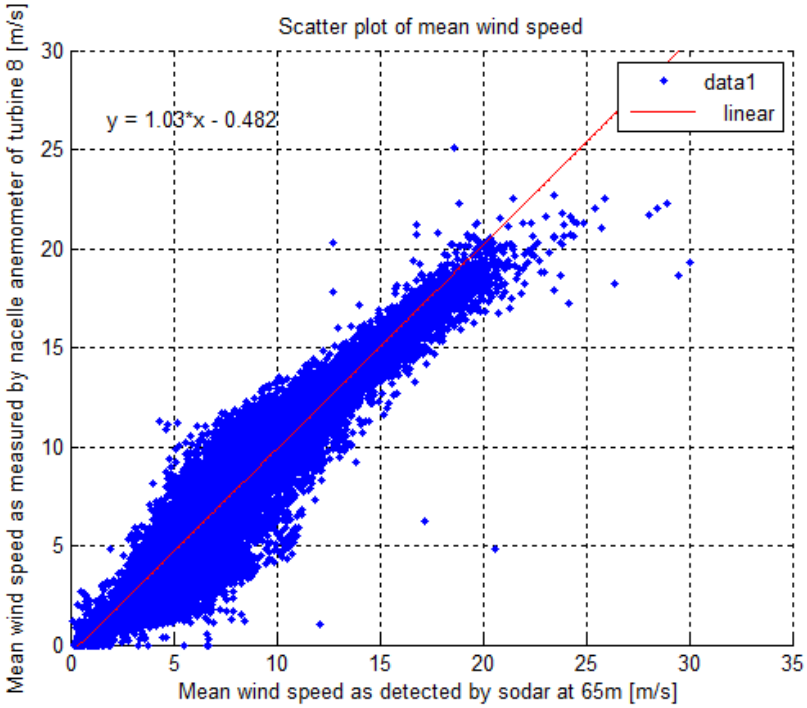

Figure 16: Nacelle anemometer 8 compared to sodar through a scatter plot. R^2 of the fit: 0.93

The scatter plots give more insight in the measurement, and reveal that the linear fits are all relatively close to $V_{sodar} = 1.0V_{nacelle} + 0.0$, although there is a 0.5 m/s offset in Figure 16. Nonetheless, this result suggests that the nacelle anemometer has been calibrated, since the theoretical speed at the hub is $V_{hub} = \frac{2}{3}V_{\infty}$. Moreover, there still is significant spread in the datapoints. This spread seems to be the largest when comparing the two nacelle anemometers, although these scatter plots give little insight in the density of the points. in fact, comparing the coefficients of determination, R^2, reveals that the spread is similar for all three plots.

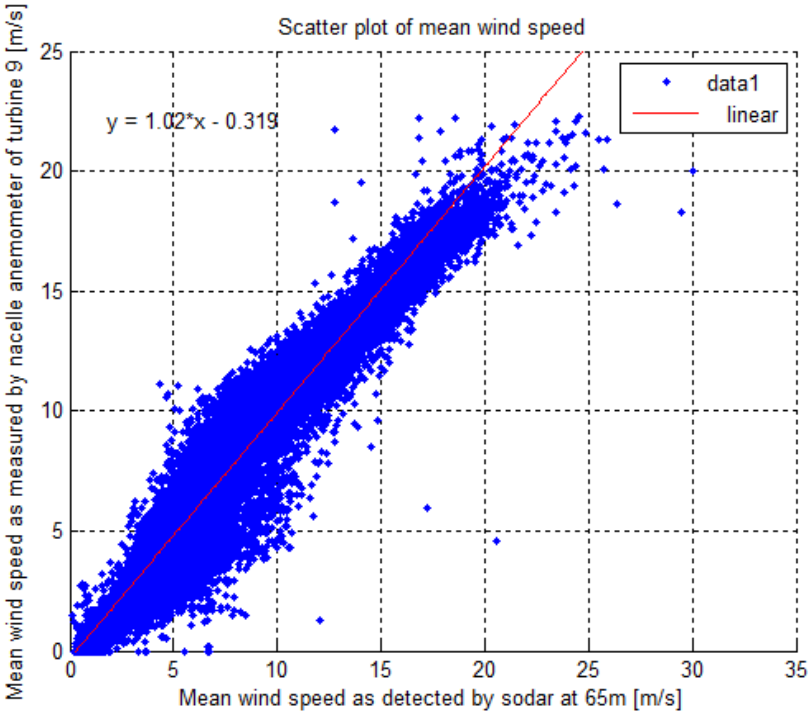

Figure 17: Nacelle anemometer 9 compared to sodar through a scatter plot. R^2 of the fit: 0.94

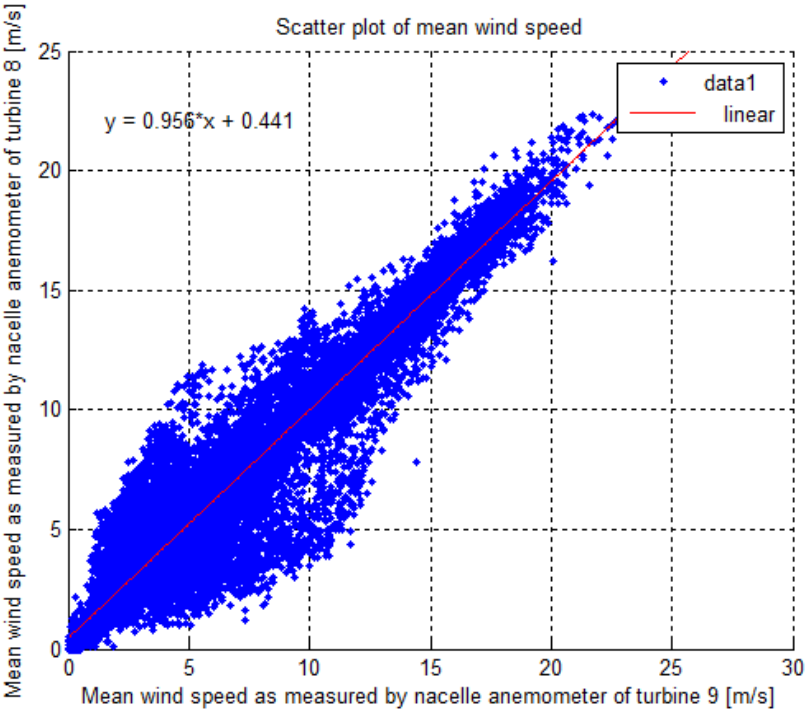

Figure 18: Nacelle anemometer 8 compared to nacelle anemometer 9 through a scatter plot. R^2 of the fit: 0.94

7.3 HISTOGRAMS

To gain more insight in density of the points in the scatter plots, histograms are made, as shown in Figure 19 – Figure 21. Comparing these suggests that the two nacelle anemometers are actually very well related, considering the tall, narrow peak. However, examining the mean, standard deviation σ (abbreviated SD) and Root Mean Square error (abbreviated RMS) reveals that the correlation is only slightly stronger than suggested by the strong peak.

In conclusion, the nacelle anemometers are suitable for getting an initial idea of the wind speed. However, they are not appropriate for determining the free stream wind speed with high accuracy. This finding is in accordance with expectations, since the anemometer is located in the wake of the rotor and is subject to the nacelle transfer function.

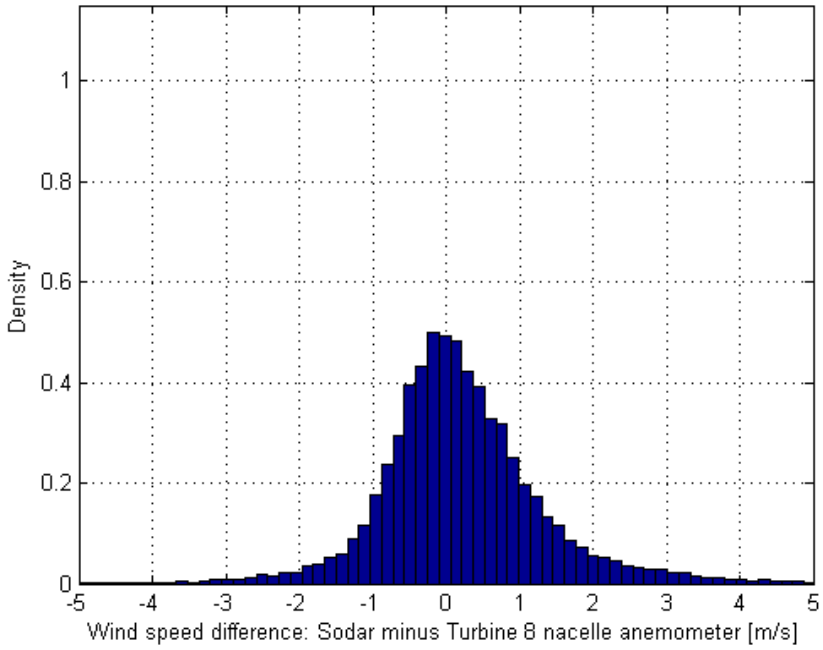

Figure 19: Nacelle anemometer 8 compared to sodar through a histogram. Mean: 0.22 m/s; RMS: 1.14 m/s; SD (σ): 1.11 m/s

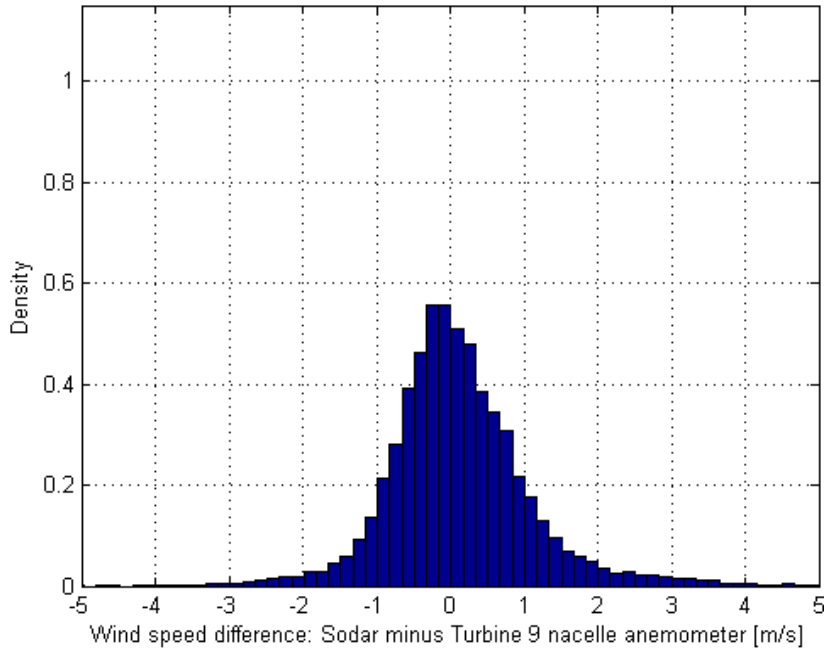

Figure 20: Nacelle anemometer 9 compared to sodar through a histogram. Mean: 0.12 m/s; RMS: 1.01 m/s; SD (σ): 1.00 m/s

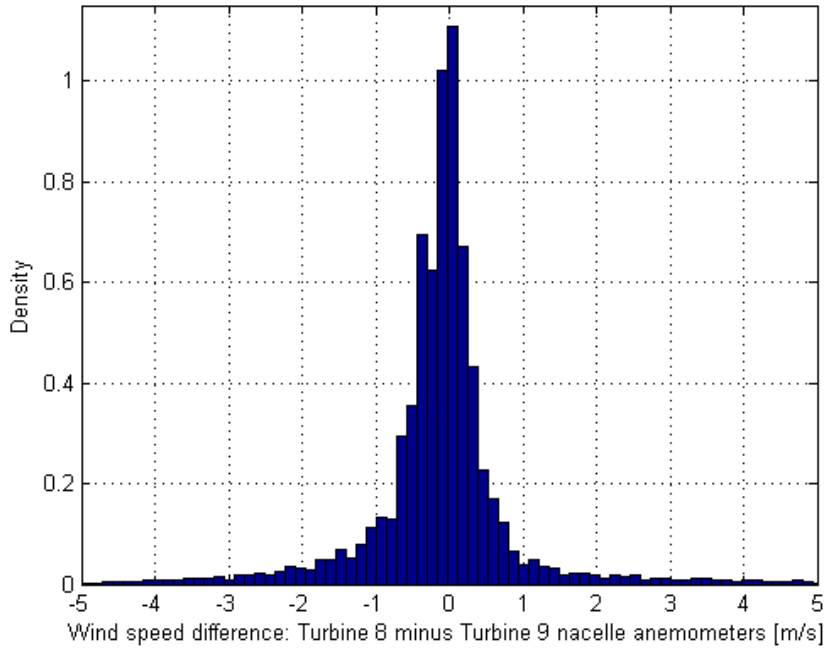

Figure 21: Nacelle anemometer 8 compared to nacelle anemometer 9 through a histogram. Mean: -0.10 m/s; RMS: 1.07 m/s; SD (σ): 1.07 m/s

8

YAW MISALIGNMENT

A direct comparison is possible between the wind direction and nacelle direction of turbine 8 and turbine 9, the two closest turbines to the sodar. This is shown using a time series plot in Figure 22. A 53 degree offset was found for turbine 9, but not for turbine 8. Examining the power curves reveals that this 53 degree offset is only present in the data and not in reality.

During installation of the nacelle-based lidar (i.e. campaign II) a time difference was discovered between universal time and the turbine's internal clock. This was corrected in the data of campaign I, to get the scada and sodar signals synchronized. A RMS (Root Mean Square) yaw misalignment of 19.4 degrees was found for turbine 8, but when neglecting yaw misalignment for wind speeds below cut-in wind speed, 4 m/s (as detected by the sodar at 65m altitude), the RMS yaw misalignment is reduced to 12.6 degrees. The mean yaw misalignment of turbine 8 (taking into account all previous data processing) is -0.72 degrees (Figure 24). The mean yaw misalignment of turbine 9 is 0.50 degrees, although this value is meaningless considering the implementation of the manual offset of 53 degrees.

It must be noted that it is a bit premature to speak of *yaw misalignment*, considering the nature of the measurements and the distance between the sodar and turbines. The term implies a problem with the turbine, whereas it would require more research to come to a conclusion on this matter. Using the nacelle-based lidar measurements a conclusion can be drawn with more certainty.

Figure 22: Nacelle direction of turbines 8 and 9 (corrected by 53°) compared to wind direction as measured by the Sodar at 65m through time series plot

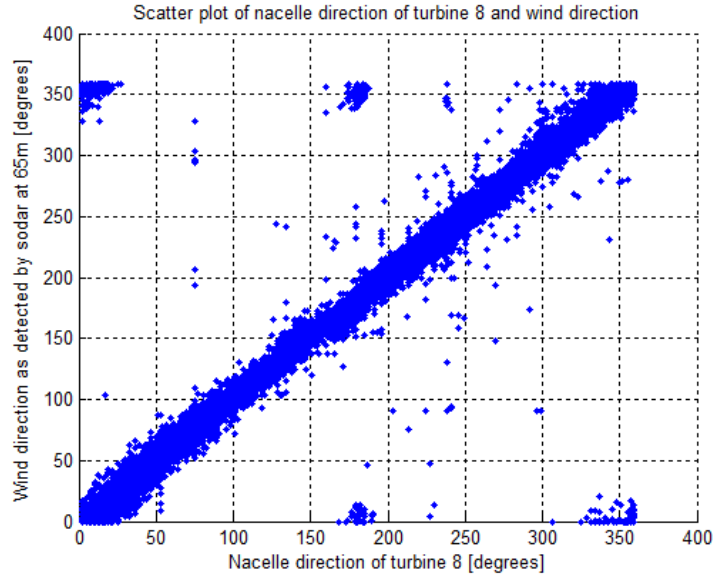

Figure 23: Nacelle direction of turbines 8 compared to wind direction as measured by the Sodar at 65m through scatter plot

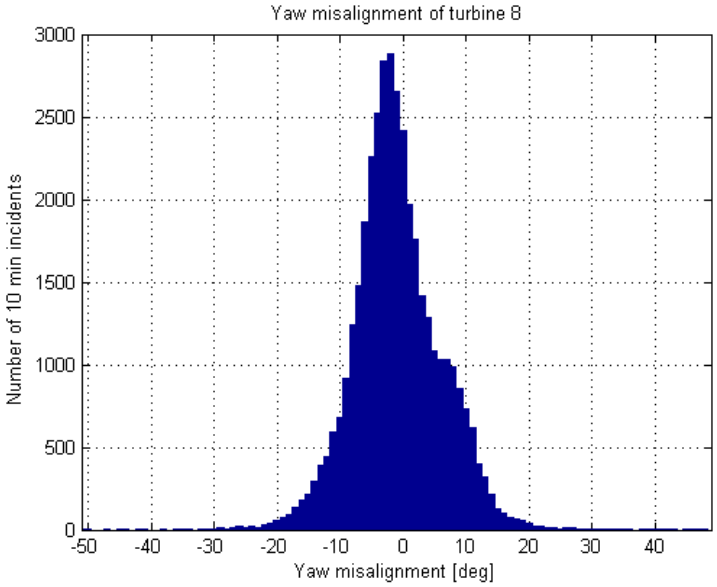

Figure 24: Nacelle direction of turbines 8 compared to wind direction as measured by the Sodar at 65m through a histogram. Mean: $-0.72°$; SD (σ): 12.5°

9 POWER CURVE

Power curve scatter plots were made for turbine 8 and 9 using both sources for wind speed (i.e. nacelle anemometer and sodar), as shown in Figure 25 – Figure 27. These plots show that the nacelle anemometer has less spread in the data points, probably because it is a very local measurement and its time logging is perfectly in sync with power production figures. If there turns out to be a time lag between the two time series which can be resolved, this will probably result in a power curve with less spread for the sodar data. However, it could also be that the nacelle anemometer is calibrated using power produced (in the nacelle transfer function), which would mean that the power curves based on the nacelle anemometer are not useful for power curve verification.

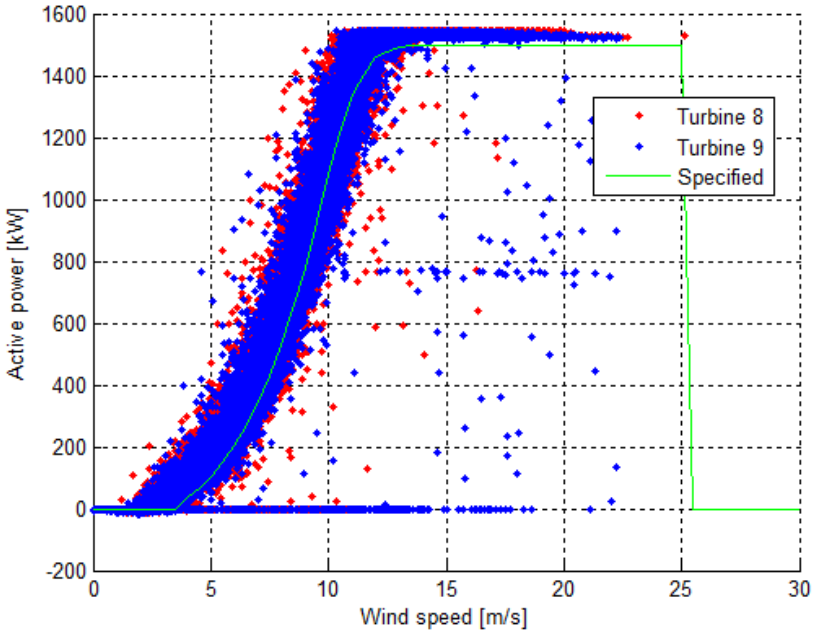

Figure 25: Power curve scatter plots for turbine 8 and 9 made using nacelle anemometers

When comparing the two wind speed measurement sources, it seems that the nacelle anemometer shows a higher production at low wind speed (2–7 m/s), but that the sodar predicts a slightly lower rated wind speed, meaning that the turbine produces full power at a lower wind speed. The specified power curve of the GE Wind 1.5s has also been plotted[36], and matches the data well.

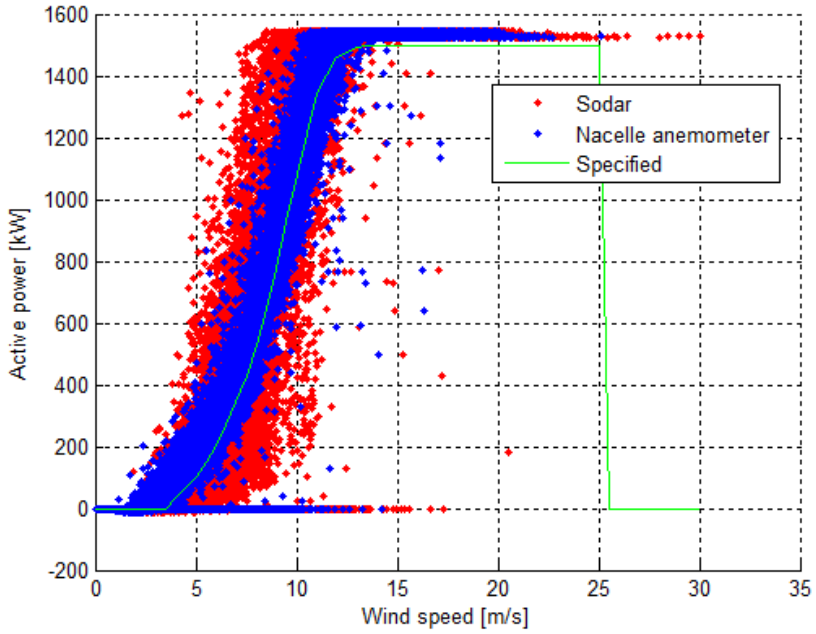

Figure 26: Power curve scatter plots for turbine 8 using nacelle anemometer and sodar

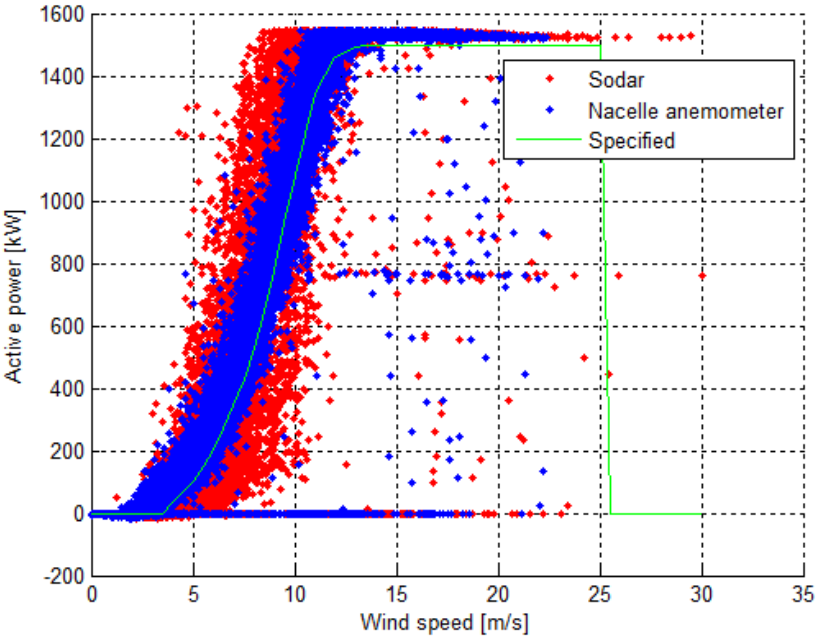

Figure 27: Power curve scatter plots for turbine 9 using nacelle anemometer and sodar

Part II

CAMPAIGN II

This part of the thesis discusses the second measurement campaign, which took place from September 2014 until January 2015. Measurements are taken with a sodar and a nacelle-based lidar (a Wind Iris by Avent) at wind park Slufterdam. Through analysis of the data, this part of the thesis aims to address the research objectives as set out in Chapter 3.

10 LIDAR WORKING PRINCIPLE

In the field of wind energy, laser signal emitted by the lidar is scattered by natural aerosols in the wind[27]. These aerosols are typically dust, water droplets, pollution, pollen or salt crystals. In case of a nacelle-based lidar, there is a stationary transmitter/observer and a moving target, causing a Doppler shift in the received signal, where the Doppler shifted frequency is directly proportional to the line-of-sight velocity[57], as shown in Equation 5. In this equation, λ is the laser wavelength, f the Doppler frequency shift and RWS the radial wind speed (i.e. line-of-sight velocity). This effect is very similar to that in sound waves, for instance from a police car moving by, where one can hear the frequency shift in the sirens. Receivers used for wind lidars are typically very sensitive, requiring just one photon for every 10^{12} transmitted to determine the wind speed[57]. The laser used is also safe for human eyes, since the radiation has a wavelength of 1.55µm[57], which is *near infrared light*[50]. Since the working principle of this type of lidar relies on the Doppler shift, it is sometimes referred to as a Doppler lidar[5].

$$RWS = \frac{\lambda f}{2} \tag{5}$$

However, just the line-of-sight velocity on its own is not very useful. Therefore in case of a two beam lidar (like the Wind Iris), the line-of-sight velocity is determined in two separate points. Assuming uniform flow, these data points can then be combined to estimate the wind velocity and direction in the space between the points[72], as shown in Figure 28.

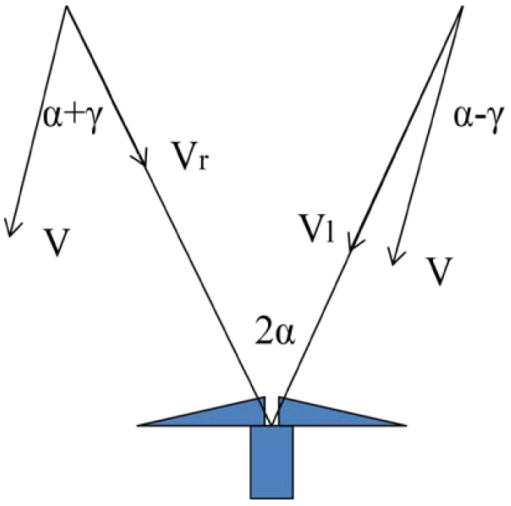

Figure 28: Calculation of wind speed and direction with a two beam lidar.[72]

In Figure 28, V is the wind vector (assuming uniform flow), V_l and V_r are the line-of-sight velocity components (left and right) as detected by the lidar, α is

the half opening-angle and γ is the wind direction relative to the lidar. The vectors as shown in Figure 28 allow the derivation of the relations as described in Equation 6[67]. The derivation itself is discussed in more detail in Appendix A.

$$\begin{aligned} V_x &= (V_l + V_r)/(2\cos\alpha) \\ V_y &= (V_l - V_r)/(2\sin\alpha) \\ V &= \sqrt{V_x^2 + V_y^2} \\ \gamma &= \arctan\frac{V_y}{V_x} \end{aligned} \tag{6}$$

To get an idea of the relations, γ and V were plotted as functions of V_r, V_l and α in Figure 29 – Figure 34. Note that if a lidar is mounted on a nacelle, the wind direction is equal to the yaw misalignment of the turbine, hence *yaw misalignment* in the titles of the figures.

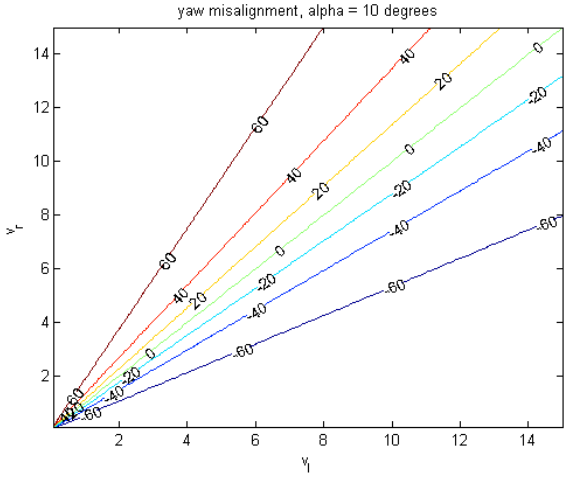

Figure 29: Wind direction as a function of line-of-sight velocities with a two beam lidar for $\alpha = 10°$

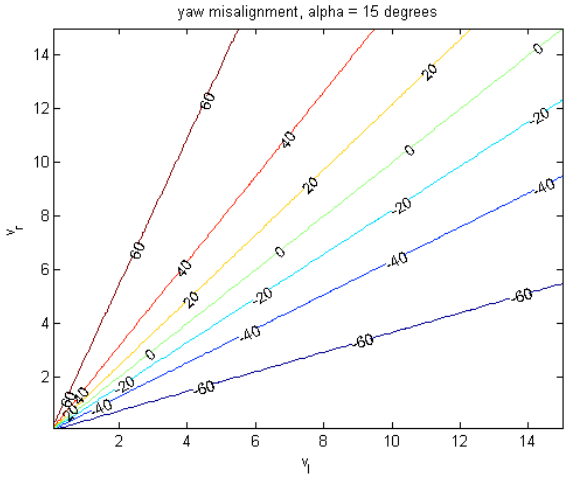

Figure 30: Wind direction as a function of line-of-sight velocities with a two beam lidar for $\alpha = 15°$

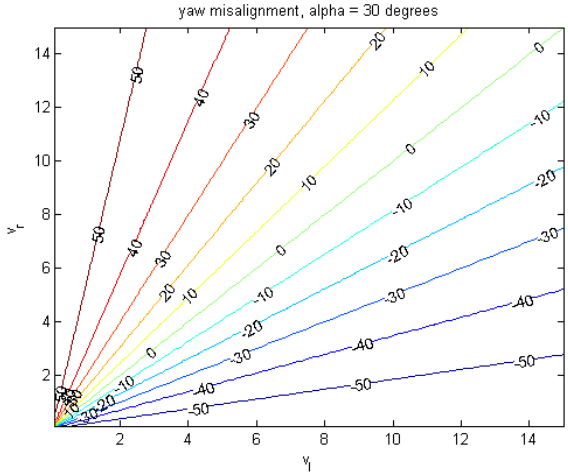

Figure 31: Wind direction as a function of line-of-sight velocities with a two beam lidar for $\alpha = 30°$

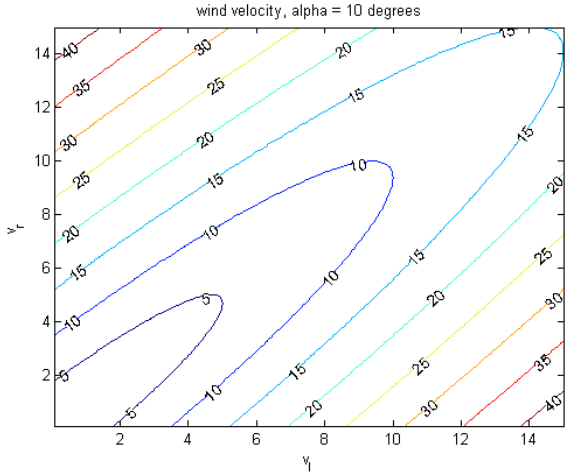

Figure 32: Wind speed as a function of line-of-sight velocities with a two beam lidar for $\alpha = 10°$

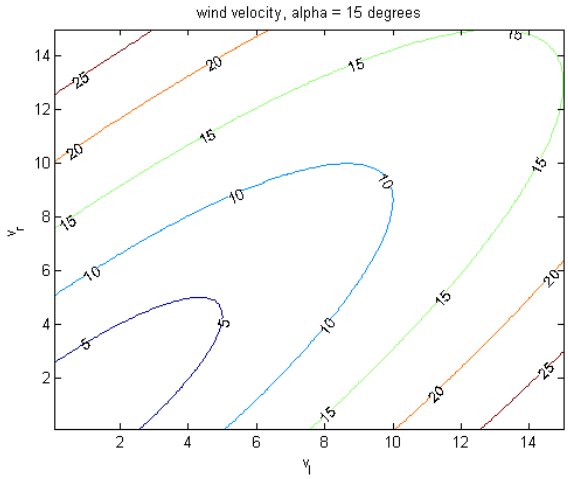

Figure 33: Wind speed as a function of line-of-sight velocities with a two beam lidar for $\alpha = 15°$

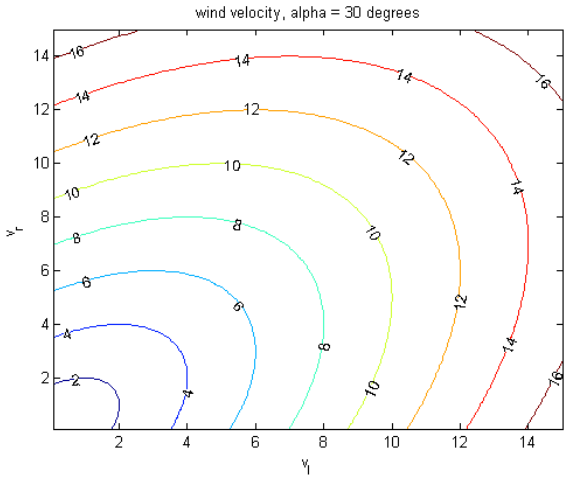

Figure 34: Wind speed as a function of line-of-sight velocities with a two beam lidar for $\alpha = 30°$

Figure 29 – Figure 34 make it clear that in the choice of opening angle α, a trade-off is to be made. If a small opening angle is chosen, the inspected wind area is smaller, giving a better indication of local wind and perhaps a better turbulence measurement. However, a small α also means that the iso-lines are closer together, in case of both direction and speed. This means that a small deviation or error in one of the line-of-sight velocities results in a larger registered yaw misalignment. In other words: yaw misalignment is measured more accurately with a large opening angle, at the cost of accuracy in the local velocity measurement. Moreover, although a larger α gives a more accurate speed measurement, it is a less local measurement. The standard setting on the Wind Iris is $\alpha = 15°$, and measurements take place 80, 120, 160, 240, 320 and 400 meters in front of the turbine.

Moreover, the case as described in this chapter is based on pulsed Doppler lidar, just like the Wind Iris used in this research. But there is a distinction to be made between two techniques within lidar wind measurements. Lidar systems can use either a continuous wave (*cw*), or a pulsating laser signal[37]. To determine the distance between the lidar and the point of interest, the CW lidar focuses its detector, whereas the pulsating lidar uses signal timing[37], i.e. measuring the elapsed time between emitting and detecting the signal. The trade-off between CW and pulsed lidar, as well as the effect of volume averaging is discussed in detail by Clive[12].

11 WIND IRIS INSTALLATION

Installation of the nacelle-based lidar took place on 18 September 2014, and was executed by Erik and Chris (Oldbaum Services), Onno (TotalWind), and Teus (Vattenfall). The tripod of the lidar is attached to the nacelle by drilling holes and fastening it with screws. The lidar was aligned to be parallel to the rotor axis using the Wind Iris' alignment diodes, and is facing down by 0.15° under no tower bend. Normally, this pre-tilt of the lidar should be such that under tower bend, the lidar measures at hub height 160m in front of the turbine, as shown in Figure 35. Unfortunately, this was not the case and the lidar measured 1.9m above hub height 160m in front of the turbine under a tower bend of 0.5°. This is discussed in more detail in Section 21.2, concluding that the results from the project are not compromised.

Furthermore, it was noted that there was a time difference of two hours between the turbine and the lidar, because the former uses local time and the latter UTC. The system was checked and found to be working correctly. Some photos of the installation are shown in Figure 36 – Figure 39.

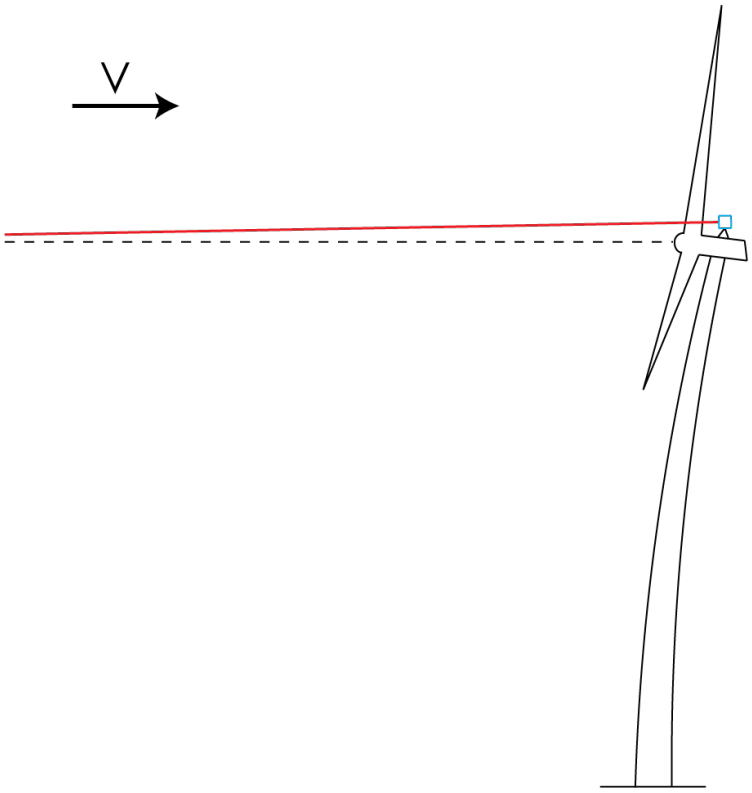

Figure 35: Exaggerated representation of tower bend and lidar tilt

Figure 36: Onno (TotalWind), Teus (Vattenfall), Erik and Chris (Oldbaum Services) preparing equipment for installation

Figure 37: Onno, Chris and Erik installing the Wind Iris on top of the turbine

Figure 38: Onno and Erik on top of the turbine

Figure 39: Wind Iris successfully installed on Wind Turbine 9 of Slufterdam West

12 WIND IRIS DATA LOGGING

Lidar data is collected in 1Hz, and is internally processed into 10 minute averages. Data logging is done according to Table 3 and Table 4. However, it must be noted that the 10 minute averages are created through vectorial averaging. In other words: they are not averaging the reconstructions (e.g. horizontal wind speed and wind direction), but creating reconstructions out of average radial wind speed.

In the high frequency data (1Hz), Table 3, the system is set up to emit beams sequentially (beam 0 and beam 1) at 1 Hz, and performs calculation reconstructing parameters such as horizontal wind speed and wind direction. These parameters are considered valid if the Carrier to Noise ratio (CNR) of both beams is higher than -21dB[70]. But also the measurement must have been taken in time (i.e. no delay; overrunstat=1) and it is a good idea to implement an upper threshold on the CNR, to exclude irrelevant reflections (e.g. turbines and birds). When looking at radial wind speeds filtering for valid radial wind speed (rwstat=1), overrun status (overrunstat=1) and CNR (CNR<0 dB) suffices, but when using reconstructions, the filter hwsstat=1 should also be included. This set of filters was compiled with help of Erik Brown of Oldbaum Services.

Parameter	Unit	Description
Timestamp	(s)	Coordinated Universal Time (UTC)
Distance	(m)	Distance along symmetry axis of lines of sight.
Line of sight	(a.u.)	2 lines of sight possible (0/1)
HWS	(m/s)	Horizontal wind speed
Direction	(°)	Direction of wind
RWS	(m/s)	Radial wind speed
RWSD	(m/s)	Radial wind speed deviation
CNR	(dB)	Carrier to noise ratio
Tilt	(°)	Tilt of system telescopes
Roll	(°)	Roll of system telescopes
RWS status	(a.u.)	0 / 1 = RWS is not valid / valid
RWS RT status (obsolete)	(a.u.)	0 = no valid RWS within "real time availability period" 1 = at least 1 valid RWS within "real time availability period"
Overrun Status	(a.u.)	0 / 1 = the measurement is late / in time
HWS status	(a.u.)	0 / 1 = HWS is not valid / valid
HWS RT status (obsolete)	(a.u.)	0 = no valid HWS within "real time availability period" (obsolete) 1 = at least 1 valid HWS within "real time availability period" (obsolete)

Table 3: Format of real time (1Hz) data

The tilt and roll of the lidar is measured by means of an inclinometer placed on top of the optical head, and this is used in Chapter 21. The signals for turbulence intensity are computed with Equation 7, i.e. with the standard deviation of the line-of-sight velocities. All four *deviations* as mentioned in Table 4 are standard deviations, but unfortunatley this is not calculated for the wind direction (*directionm*).

$$TI0 = abs\left(\frac{dRWS0}{RWS0m}\right) \quad TI1 = abs\left(\frac{dRWS1}{RWS1m}\right) \quad TI = \frac{TI0 + TI1}{2} \tag{7}$$

Parameter	Unit	Description
Timestamp	(s)	Coordinated Universal Time (UTC)
Distance	(m)	Distance along symmetry axis of lines of sight.
HWSm	(m/s)	Average horizontal wind speed (vectorial)
HWSmax	(m/s)	Maximum horizontal wind speed
HWSmin	(m/s)	Minimum horizontal wind speed
Directionm	(°)	Average direction (vectorial)
Um	(m/s)	Average wind speed component along Ox axis
Vm	(m/s)	Average wind speed component along Oy axis
RWS0m	(m/s)	Average LOS0 radial wind speed
dRWS0	(m/s)	LOS0 radial wind speed deviation
RWS1m	(m/s)	Average LOS1 radial wind speed
dRWS1	(m/s)	LOS1 radial wind speed deviation
TI	(a.u.)	Mean turbulence intensity
TI0	(a.u.)	LOS0 turbulence intensity
TI1	(a.u.)	LOS1 turbulence intensity
CNR0m	(dB)	Average LOS0 CNR
CNR0max	(dB)	Maximum LOS0 CNR
CNR0min	(dB)	Minimum LOS0 CNR
CNR1m	(dB)	Average LOS1 CNR
CNR1max	(dB)	Maximum LOS1 CNR
CNR1min	(dB)	Minimum LOS1 CNR
Tiltm	(°)	Average tilt
dTilt	(°)	Tilt deviation
Rollm	(°)	Average roll
dRoll	(°)	Roll deviation
RWS0 availability	(a.u.)	LOS0 data availability $\in [0,1]$
RWS1 availability	(a.u.)	LOS1 data availability $\in [0,1]$
HWS availability	(a.u.)	Reconstruction data availability $\in [0,1]$

Table 4: Format of 10 minute average data

As mentioned in Chapter 10, the Wind Iris takes measurements 80, 120, 160, 240, 320 and 400 meters in front of the turbine. To get an idea of scale, these distances are illustrated as concentric circles in Figure 40. If applicable, this measurement distance is referred to in labels of plots and figures. To prevent confusion, the approximate measurement height of 65m is also included in these labels. For example, (h=65m, d=160m) refers to measurements 160m in front of the turbine.

Figure 40: Measurement distances of the Wind Iris

13

USER EXPERIENCE (RESEARCH OBJECTIVE I)

The first research objective of this thesis is to *gain experience with the installation and operation of the Avent Wind Iris, as well as the collection and analysis of the data, considering that a good dataset is a prerequisite for further analysis.* This research objective will be addressed in this chapter and is listed in Chapter 3 among the other objectives.

As discussed in Chapter 11, the installation of the Wind Iris took one day and was carried out by four technicians, although this could possibly be reduced to three. No major issues arose during installation. However, as mentioned in Chapter 11, the tilt of the lidar was not set entirely accurately. As will be discussed in Section 21.2, this does not compromise the goals of this project. However, when great accuracy is required for a power curve measurement or for blockage research, it is recommended that the tilt calculations are double checked. Another option is to adjust the tilt of the nacelle-based lidar during the campaign, after having analyzed the tower bend.

Moreover, it is possible to set the measuring distances of the lidar in the software of the system, so it is recommended that next time the 2D and 2.5D points are added before the start of the campaign. It is also possible to add these points while measuring, but this creates an inconsistent data set. When blockage is investigated, it is recommended that the maximum number of measurement points are included, which in case of the Wind Iris is ten.

Access to the data was straight-forward through Oldbaum's FTP server. Processing of the data was carried out in Matlab, which is also relatively straightforward since the designations of the columns can be found in the Wind Iris manual or by contacting Oldbaum Services. There is also plenty of literature available on the topic, which is useful for comparison and verification.

Availability of the Wind Iris during the campaign was good: 90% of the 10 minute points are available (i.e. not NaN), meaning that the instrument was operating properly 90% of the time. This is also related to the finding that the cable had become unplugged early December, of which the cause is unknown. Each 10 minute data point is based on a maximum of 600 1Hz data points, which also allows for another means of measuring availability: for instance if a 10 minute data point is based on 400 1Hz points, the parameter *HWS Availability*, is 67%. During the entire campaign the average *HWS Availability* is 82%, which is also good, considering that this includes blades passing in front of the instrument. These two availabilities can be combined, leading to a total availability of 74%.

14 POST-PROCESSING

14.1 TIME CORRECTION

Before datasets can be analyzed, some post-processing has to be done. For instance, the time difference has to be confirmed in Figure 41 and corrected. As noted in Chapter 11, during installation a two hour mismatch was observed between the lidar and turbine. Examining the wind velocity time series as measured by the nacelle anemometer and lidar in Figure 41 reveals that there is indeed a two hour mismatch. Therefore the turbine time stamps are converted to UTC. This is done in the Matlab script, and also takes in the daylight saving change on 26 October 2014 into account. This namely affects the turbine's internal time but not the lidar's, changing the 2 hour mismatch to a 1 hour mismatch.

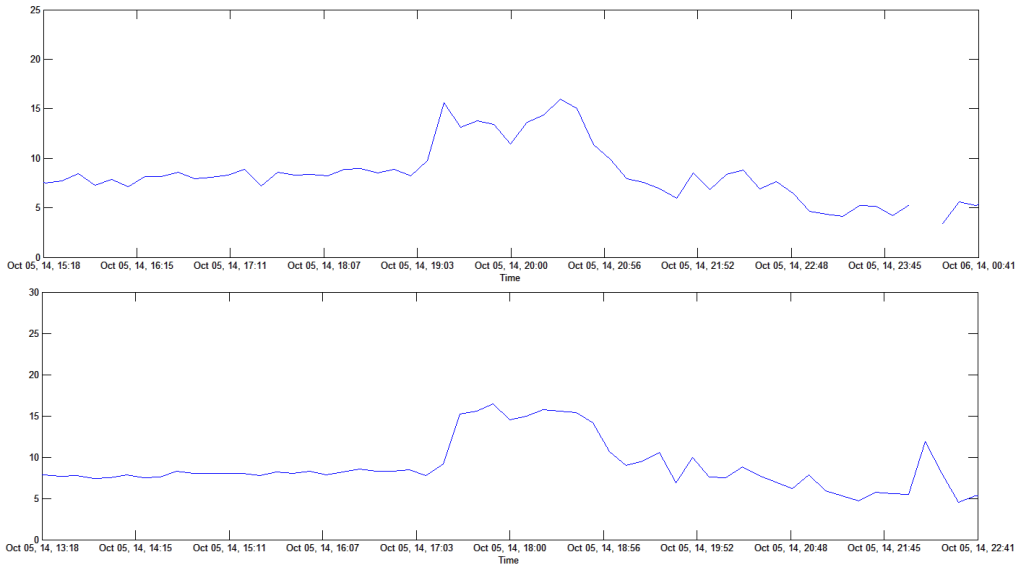

Figure 41: Confirming the time difference between the turbine and nacelle-based lidar using a time series plot of wind velocity

14.2 HWS AVAILABILITY AND CNR

A horizontal wind speed (HWS) calculation is logged by the lidar if the Carrier-Noise-Ratio (CNR) better than -21 dB. This is reflected in Figure 42, where the HWS availability is plotted against the mean CNR of beam 0. This plot shows that there is indeed internal data processing before the data is logged. More specifically, the strong increase in HWS availability around -21 dB shows that the horizontal wind speed is only logged (i.e. available) if the CNR is better than -21 dB, which is in agreement with the lidar specifications. To get an idea of the mean wind speed associated with certain CNR values, Figure 43 is plotted. This plot shows that the horizontal lidar does not necessarily have a preference for high/low wind speed.

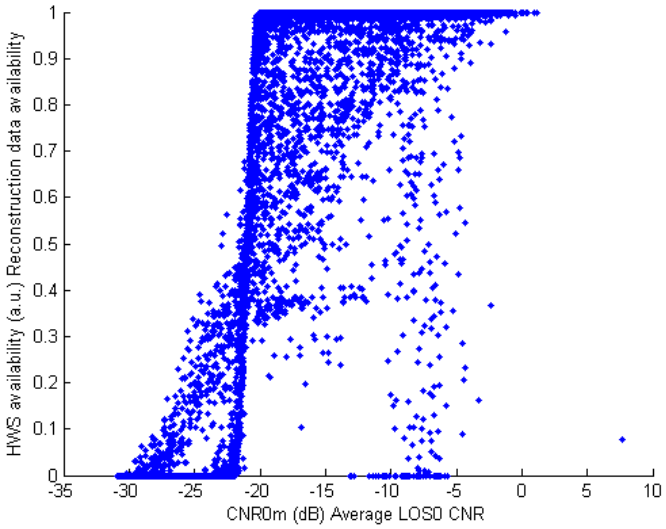

Figure 42: Relationship between HWS Availability and mean Carrier-Noise-Ratio of beam 0

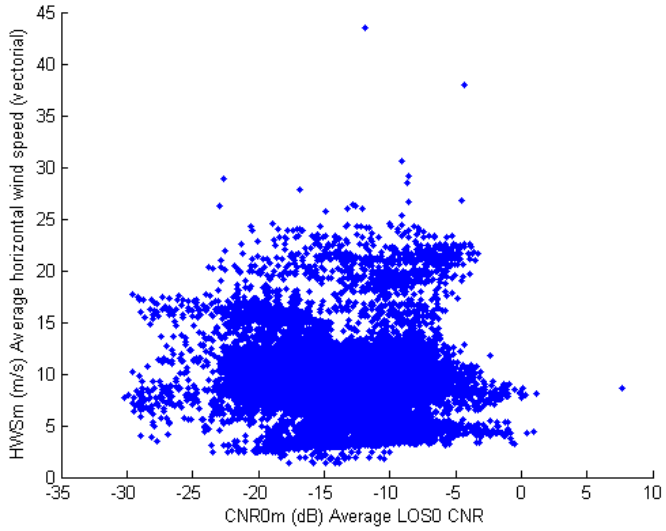

Figure 43: Mean horizontal wind speed plotted against Carrier to Noise Ratio

Figure 44 shows the average CNR as plotted against distance from the lidar. The result is similar to the findings of Cariou et al. as shown in Figure 45[10]. In both cases there is a peak in CNR, and in the case of the Wind Iris this peak is more or less in the middle of the range (80-400m).

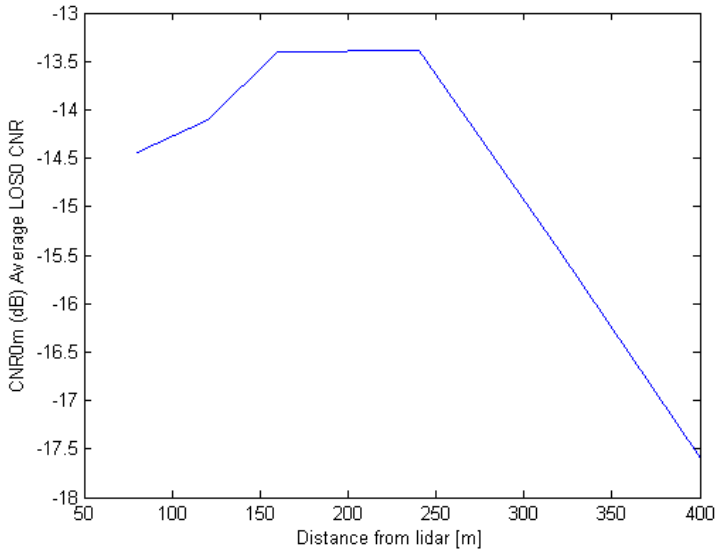

Figure 44: Meaured CNR plotted against distance from lidar

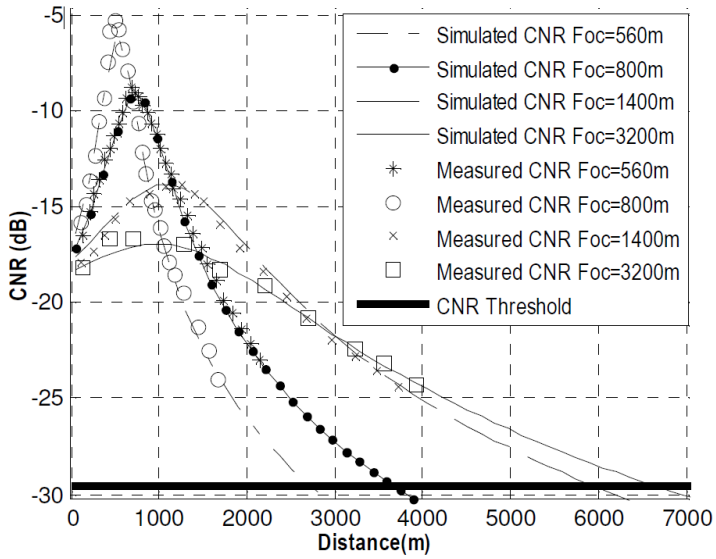

Figure 45: Measured and simulated CNR for different Focusing Distances[10]

15 VALIDATION

Before data is analyzed, checks are carried out and comparisons are made to evaluate the validity of the measurements.

15.1 INITIAL CHECK

Besides comparing the lidar to sodar and turbine data (e.g. nacelle anemometer), some initial checks can be performed. For instance, a histogram of horizontal wind speed is made (based on one hour of 1Hz data, all distances included), as shown in Figure 46. As expected, this more or less follows a bell curve.

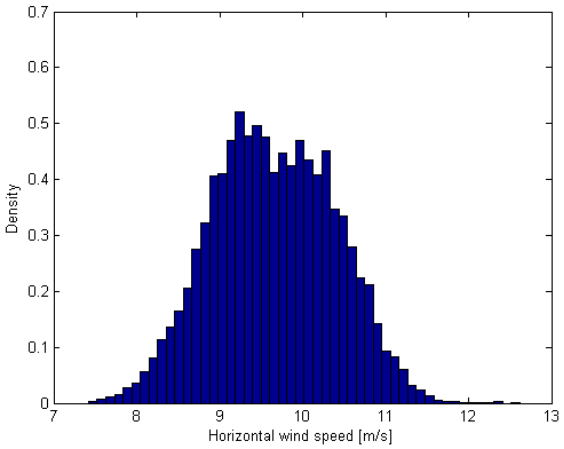

Figure 46: Histogram of horizontal wind speed (HWS), to get an idea of validity of the data

Also the timeseries of the measurements can be compared, as shown in Figure 47. This plot shows that all data sources are in sync and capture the same trend. However, there are still quite some differences. Of all signals, the cup anemometer on the nacelle shows the strongest fluctuations, and the lidar signals seem the most steady. The cup anemometer measures disturbed wind, since it is located in the wake of the rotor, which could be an explanation for the fluctuations. Moreover, the lidar measures undisturbed flow (the turbine rarely faces the wakes of other turbines), and also has some spatial averaging, which could be the explanation for the steadier nature of the signal. The wind speed at Hoek van Holland is quite different from the other signals, but this can be explained as it is approximately 10km away and measures at 14.6m height instead of 65m.

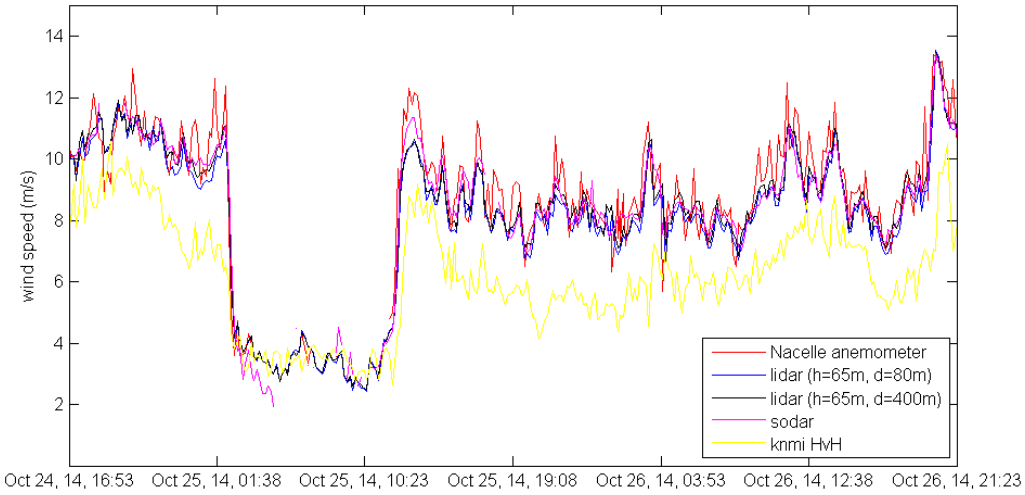

Figure 47: Timeseries of wind speed as measured by nacelle anemometer, sodar and lidar. Wind speed at KNMI station Hoek van Holland included for reference

15.2 WIND SPEED

An indication of measurement accuracy can be made using Figure 48, where mean wind speeds are compared from the sodar and nacelle-based lidar. In this plot, the worst outliers are filtered out by the minimum HWS availability of 0.98 and minimum sodar signal/noise ratio of 8. The least squares fit is very close to the ideal $y = 1x + 0$ and coefficient of determination is high, $R^2 = 0.97$. Even though one can wonder if the sodar is validating the lidar or vice versa, the result that (nacelle-based) lidar can measure wind speed accurately is in accordance with literature[4] [34] [37] [43] [51] [57] [65] [66] [67] [70]. For example, Wagenaar et al. plotted the Wind Iris horizontal wind speed against met mast measurements, finding $y = ax + b$ with $a = 1.003$, $b = 0.002$ and $R^2 = 0.99$[65]. Similarly, Wagner and Davoust found $a = 1.005$, $b = 0.004$ and $R^2 = 0.996$[70]

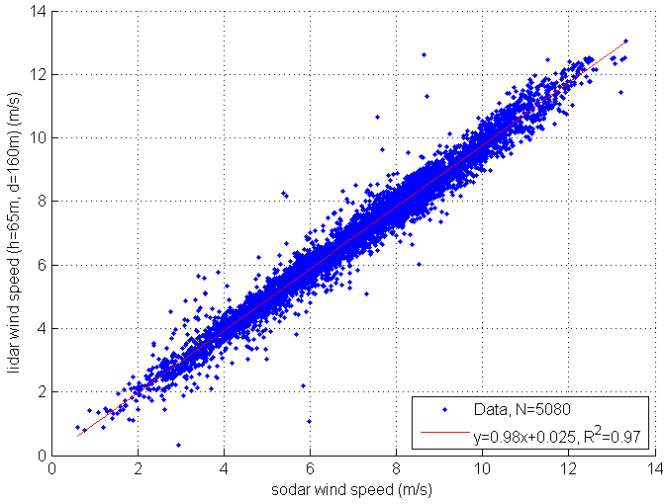

Figure 48: Validation of lidar/sodar by comparing wind speed measurements

A comparison is also made between the wind speeds as measured by the lidar at Slufterdam and the KNMI station at Hoek van Holland. The result is shown in Figure 49, which illustrates that on average the wind speed at Slufterdam is 1.1 m/s higher than at Hoek van Holland. However, the former measures at hub height (65m), while the latter measures at 14.65m. Nevertheless, there still is good correlation and the slope of the linear regression is very close to one, adding to the trust in the lidar and sodar measurements.

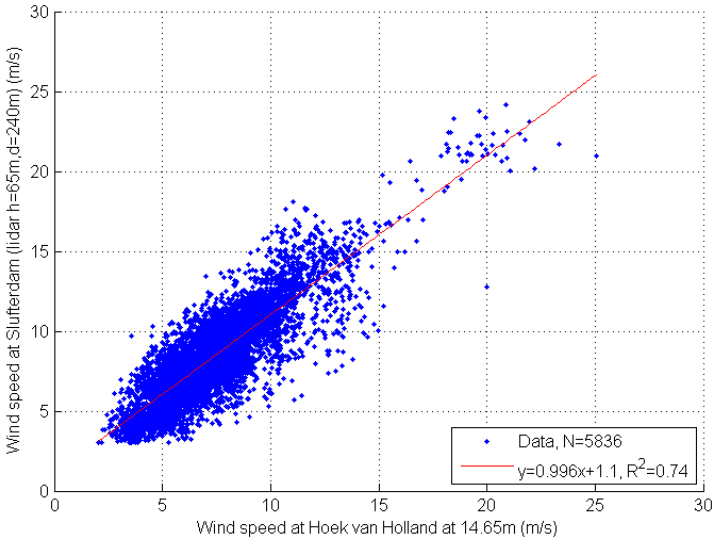

Figure 49: Validation of lidar by comparing wind speed to KNMI station Hoek van Holland

15.3 TURBULENCE INTENSITY

The lidar has a means of measuring the turbulence intensity, as discussed in Chapter 12 (Equation 7). Moreover, the sodar registers the mean wind speed ($\overline{V}$) and standard deviation in wind speed (σ), and so the turbulence intensity can also be calculated using sodar data, with Equation 8.

$$TI = \frac{\sigma}{\overline{V}} \tag{8}$$

Consequently, a scatter plot can be made to compare the sodar and lidar in terms of turbulence intensity measurement, as shown in Figure 50. This plot shows that there is a correlation between the turbulence intensity measurements, but there is quite a lot of spread, indicating significant uncertainty in at least one of the measurements. The plot also shows that the sodar perceives higher turbulence intensity than the nacelle-based lidar. The idea that lidar has difficulty measuring turbulence was also found in literature[12] [40], although there is no consensus[65] [35]. For instance, Krishnamurthy et al. conclude that *[the] accuracy of turbulence intensity from lidar profiler measurements compare well with tower measurements*[35]. Wagner and Davoust plotted Wind Iris TI versus cup anemometer TI on a met mast and found $y = 0.95x$ with $R^2 = 0.80$, noting that TI_{lidar} *and* TI_{cup} *are found to display an encouraging level of correlation*[70].

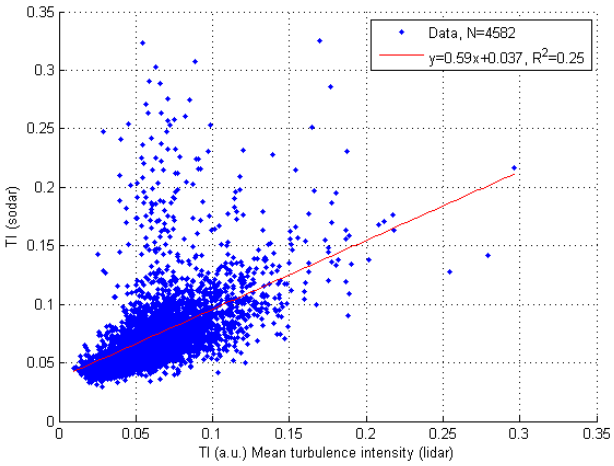

Figure 50: Validation of lidar/sodar by comparing Turbulence Intensity measurements

To gain some more understanding, a similar plot to that of Wagenaar et al. is made and both are shown in Figure 51[65]. However, since there is no met mast on site, sodar data is used, and one must also keep in mind that the sites are different. Compared to Wagenaar et al., the results from Slufterdam show a larger difference between the two TI measurements, even though the general trends are similar. Moreover, the sodar records a higher turbulence intensity for all wind speeds.

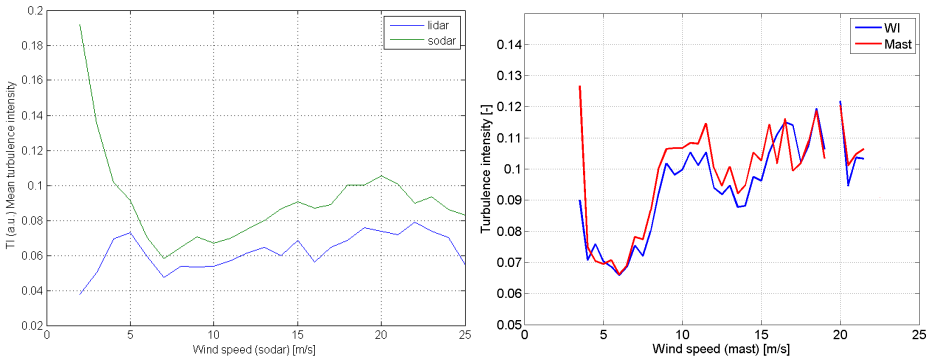

Figure 51: Turbulence Intensity (lidar and sodar) versus wind speed (left) and Turbulence Intensity (lidar and met mast) versus wind speed by Wagenaar et al.[65] (right)

Unfortunately, Wagenaar et al. only show the binned plot[65], giving little insight in the spread of the data points. In case of the Slufterdam, such a plot is shown in Figure 52, which reveals that there is significant spread. The spread is of such magnitude that one can wonder if a comparison based only on binned data is justified.

Considering that there is no consensus in literature and that own measurement also indicate uncertainty in turbulence intensity measurements, analyses involving turbulence intensity with pulsed lidar should be viewed with care.

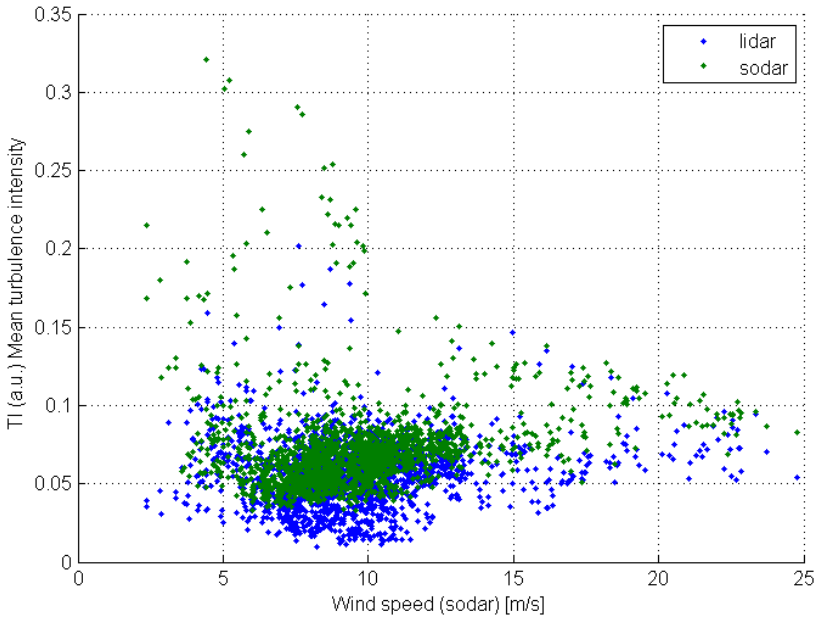

Figure 52: Turbulence Intensity (lidar and sodar) versus wind speed

15.4 DIRECTION

Another means of validating the data is using direction, considering that three data sources have some means of measuring absolute or relative direction: the turbine logs the direction of the nacelle, the sodar measures wind direction, and the lidar measures yaw misalignment. On paper, the difference between the wind direction and nacelle direction should be equal to the yaw misalignment, as discussed in Chapter 8.

First, however, the sodar is corrected for its direction. During the installation, it was assumed that the sodar is facing East (i.e. +90 degrees from North), so any corrections during post-processing will be with respect to East. As mentioned in Section 4.3.2, two direction measurements were taken of the sodar, one using GPS (120 degrees from north), and one using landmarks and Google maps (124 degrees from north). Since the GPS method is deemed more reliable, 120 degrees is assumed correct, so the direction signal is shifted by 30 degrees.

To check this correction and get a better idea of the wind direction measurements, a comparison is made with the measurements by KNMI at Hoek van Holland. This station is just 10km away from the site and also logs data in 10 minute intervals. As shown in Figure 53, the general trend in the two signals is very similar. It seems that the sodar perceives the wind direction slightly higher (i.e. further clockwise) than the KNMI station. This could be caused by the difference in measurement height (14.65m versus 65m), location or by incorrect calibration.

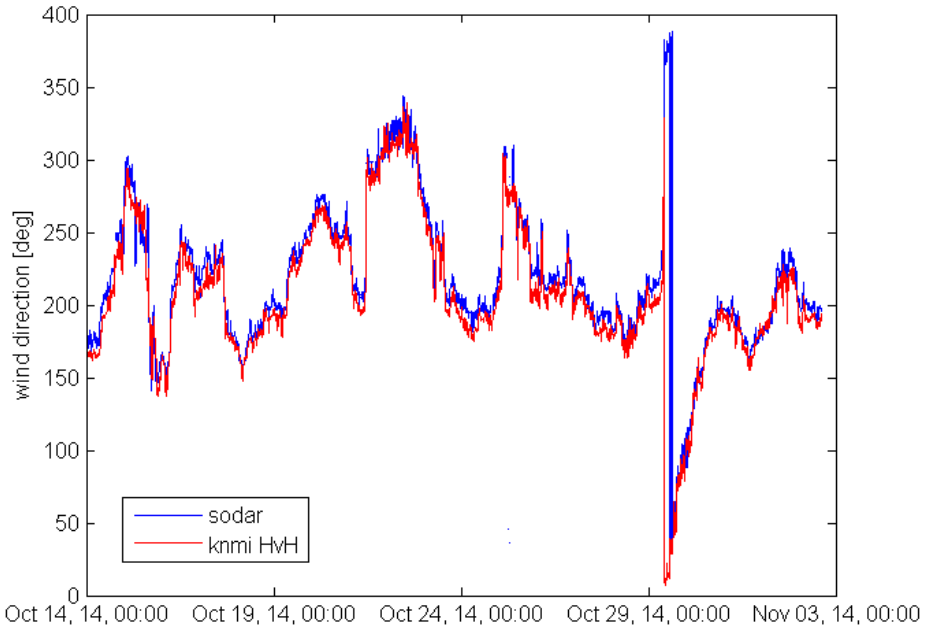

Figure 53: Time series of wind direction as measured by sodar and at KNMI station at Hoek van Holland

Another means of comparing wind directions at the KNMI station and the sodar is shown in Figure 54. This plot shows that there is indeed a very strong correlation between the wind direction measurements. Once again, there seems to be an offset, which can also be seen in the calculated trend line. This offset is on average 7 degrees, but it is left as it is, since the GPS measurement seems more reliable than assuming the same wind directions at Hoek van Holland and Slufterdam.

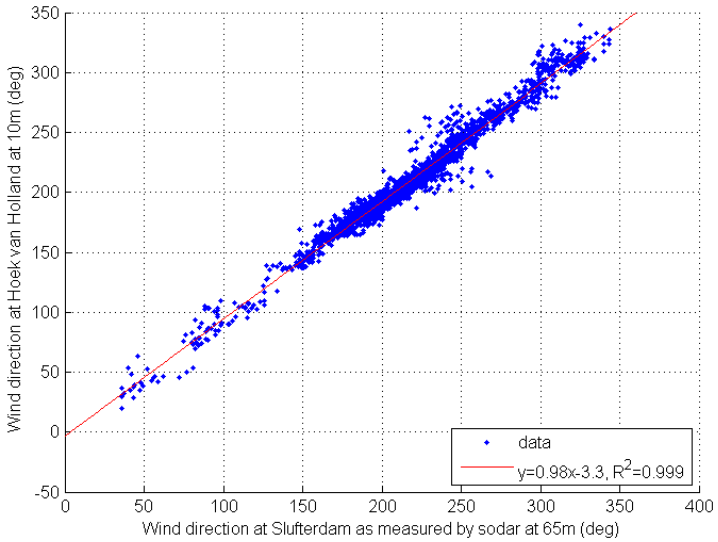

Figure 54: Scatter plot of wind direction as measured by sodar and at KNMI station at Hoek van Holland

Next, the wind direction as measured by the sodar can be compared to the direction of the nacelle of turbine 9, a similar procedure as carried out in Chapter 8. The result is shown in Figure 55 and shows a very good match: the

trend line has a gradient very close to one, and there is little scatter around the trend line (resulting in $R^2 = 0.99$). However, the trend line is shifted down, i.e. not crossing the origin. Like in Chapter 8, it is impossible to determine with certainty if this is due to the offset in sodar and/or nacelle direction, or if it is a constant yaw misalignment. However, unlike in Chapter 8, there now is a much more direct means of measuring the yaw misalignment, namely the nacelle-based lidar.

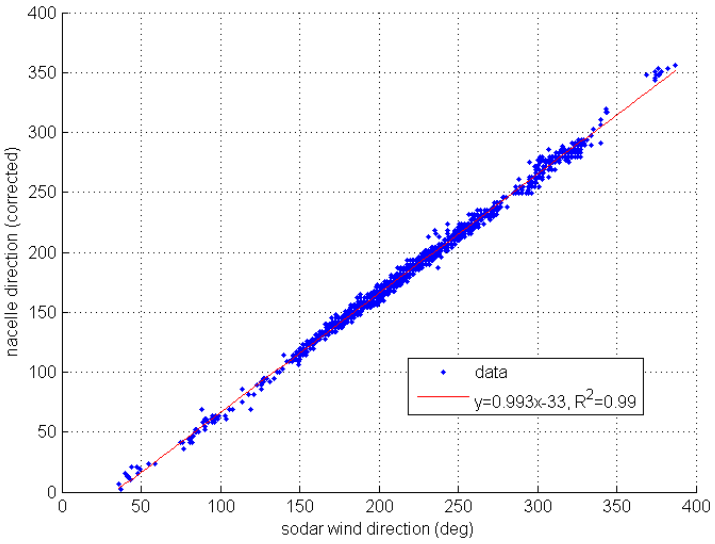

Figure 55: Scatter plot of wind direction as measured by sodar and the nacelle direction of turbine 9

After introducing an offset to the scada signal such that the mean yaw misalignment is approximately zero, the time series of the nacelle direction and wind direction as measured by the sodar is plotted in Figure 56. This plot reaffirms that the signals are in sync and capture the same trends quite accurately.

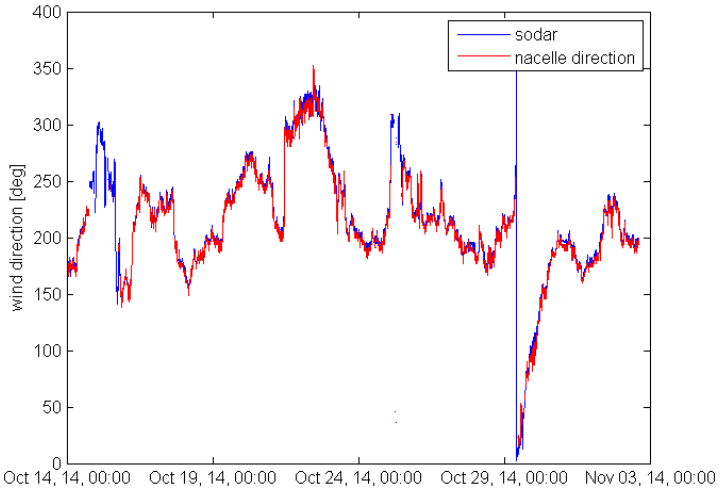

Figure 56: Time series of wind direction as measured by sodar and the nacelle direction of turbine 9

Next, the time series of yaw misalignment can be compared. This is shown in Figure 57, where the *scada/sodar* signal is the wind direction as measured by the sodar subtracted from the nacelle direction. The nacelle-based lidar measures yaw misalignment in a much more direct fashion and is shown in black. The plot makes it clear that there are significant differences between the signals.

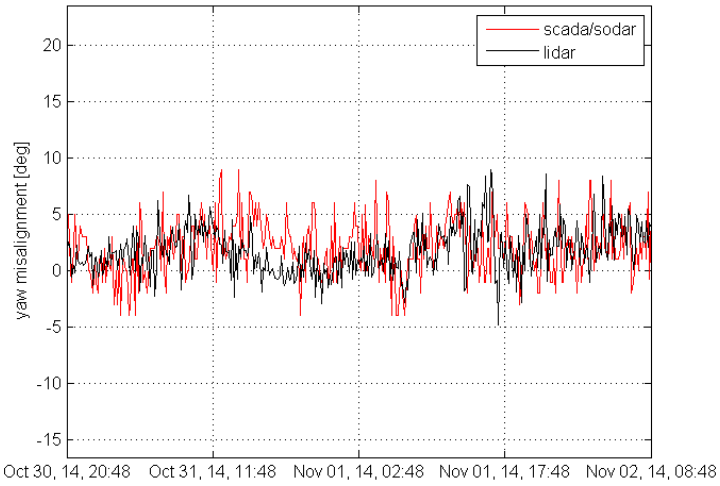

Figure 57: Time series of yaw misalignment

These differences become even clearer when examining Figure 58. Once again, one would hope to find a $y = ax + b$ trend with "a" close to 1 or -1 and any "b" value could be explained by offsets. Unfortunately, the correlation in the figure is very weak. Assuming the nacelle-based lidar can measure yaw misalignment relatively accurately, this means that the *scada/sodar* method is simply too crude. Where trends in the original signal were captured accurately (Figure 55), this is not the case when subtracting the signals to determine yaw misalignment. An explanation for this is that these data signals are meant to capture trends from $0 - 360$ degrees, hence their measurement uncertainty is probably relatively high. Moreover, assuming the measurements error to have a random character, the subtraction of the signals leads to a summation of the variances. This is shown in Equation 9, where the signals are assumed to be normally distributed random variables with mean μ and standard deviation σ. The resulting yaw misalignment signal has a large variance, seemingly too large to actually capture yaw misalignment. This effect is simulated and discussed in Appendix D, from which the conclusion is drawn that both methods have significant measurement uncertainty: lidar in the order of 4 degrees, sodar in the order of 5 degrees.

$$\begin{aligned} \text{Nacelle direction } X &\sim N(\mu_X, \sigma_X^2) \\ \text{Wind direction (sodar) } Y &\sim N(\mu_Y, \sigma_Y^2) \\ \text{Yaw misalignment } Z &= X - Y \end{aligned}$$

$$Z \sim N(\mu_X - \mu_Y, \sigma_X^2 + \sigma_Y^2) \tag{9}$$

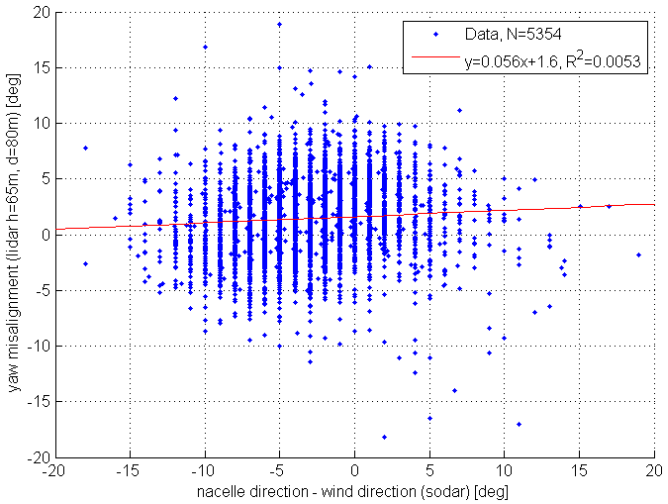

Figure 58: Scatter plot of yaw misalignment

On the other hand, to get an initial idea of the spread in yaw misalignment, like discussed in Chapter 8, it seems the *scada/sodar* method might be applicable. As shown in Figure 59, the two methods (nacelle-based lidar and scada/sodar) have similar bell curves, although it must be noted that the bell curve of the *scada/sodar* method has been shifted by +5 degrees to let the mean yaw misalignment match that of the lidar. Nonetheless, as discussed in Appendix D, the most realistic yaw misalignment histogram will have a smaller spread, due to the measurement error in both methods. In conclusion, the *scada/sodar* method is suitable for determining the maximum spread in yaw misalignment, and the Wind Iris is suitable for determining the mean yaw misalignment as well as the maximum spread in yaw misalignment.

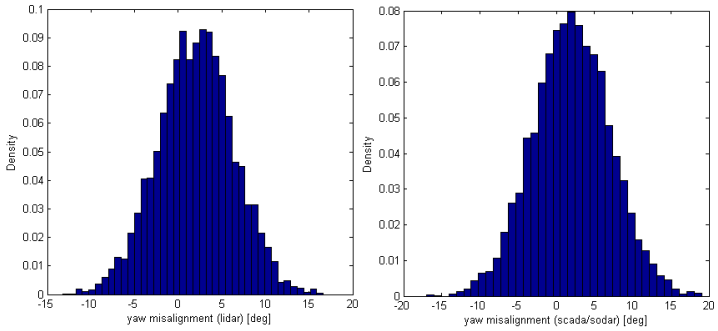

Figure 59: Yaw misalignment histograms of turbine 9 made with nacelle-based lidar (left) and the *scada/sodar* method (right)

Another means of evaluating the accuracy of the lidar's yaw misalignment measurement is by looking at literature: Wagner and Davoust carried out an experiment with the Wind Iris on wind park Avedøre in Denmark[70]. Located 2D southwest of the turbine with the Wind Iris is a met mast with a wind vane 4m below hub height in accordance with IEC 61400-12-1[26]. By comparing the nacelle direction to the vane direction on the met mast (Figure 60[70]) they concluded that the turbine is well aligned with the wind.

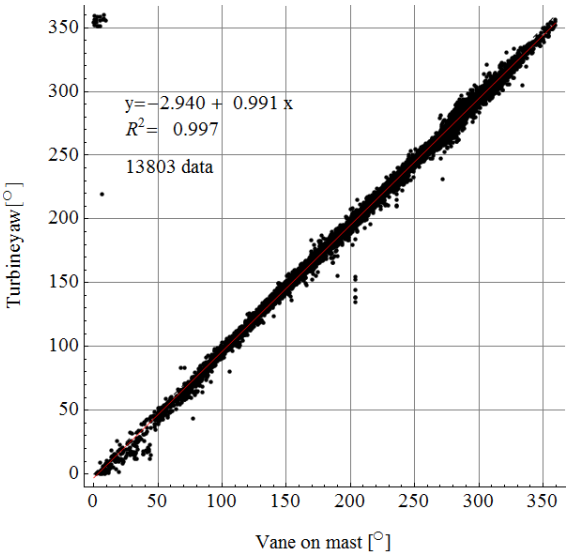

Figure 60: Comparison and linear regression between the turbine yaw and the direction indicated by the wind vane on the met mast[70]

Next, the yaw misalignment as measured by the nacelle-based lidar was subtracted from the nacelle direction, which would on paper give a perfect $y = x$ fit. The result is shown in Figure 61[70], illustrating that this is clearly not the case. Wagner and Davoust explain the difference: *a major issue when using a nacelle lidar to obtain the wind direction is that the lidar cannot make the difference between a misalignment between the wind direction and its axis (turbine yaw error for example) and a situation where the wind speed is not horizontally homogeneous. For instance, if one of the lidar beam is in the wake of a surrounding obstacle, whereas the second beam is outside the wake (large inhomogeneity in the wind speed seen by the two beams), the lidar gives a large relative wind direction angle even though the lidar is well aligned with the wind direction.*[70].

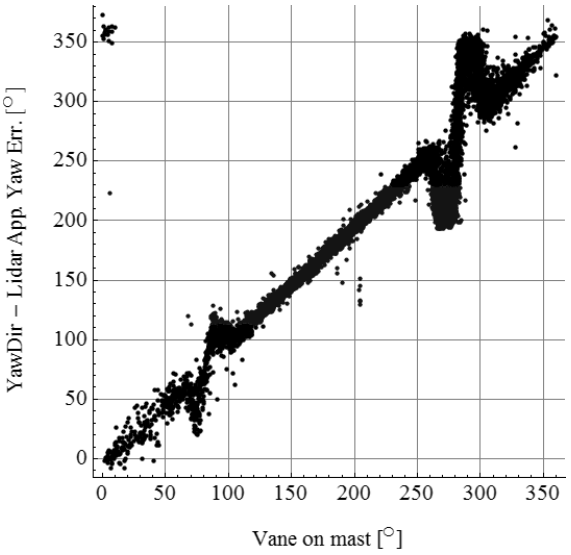

Figure 61: Comparison between the wind direction obtained by subtracting the lidar relative direction to the turbine yaw and the direction given by the vane on the met mast.[70]

Figure 61 also shows that when there are no obstacles upwind, i.e. wind direction $100 - 250$ degrees, there is a good fit. Furthermore, the problem does not arise due to random turbulence, since these fluctuations are averaged out in the 10min data.

A similar plot can be made using the data from Slufterdam, as shown in Figure 62. It seems the yaw misalignment does depend on the direction the nacelle is facing. If one of the lidar beams is measuring in a wake the lidar can perceive a non-existent yaw misalignment, as illustrated by Wagner and Davoust in Figure 61. However, in case of the Slufterdam this only occurs for nacelle directions between approximately 300 and 90 degrees (i.e. NNW-E). While this part of the plot indeed shows more spread in perceived yaw misalignment, there is also an almost sinusoidal trend between 90 and 300 degrees, even though these are free stream directions. It is difficult to distinguish whether the turbine is indeed misaligned for these directions or the lidar is incorrectly perceiving the misalignment. In either case, the trend might be related to the dike on which the turbine is located.

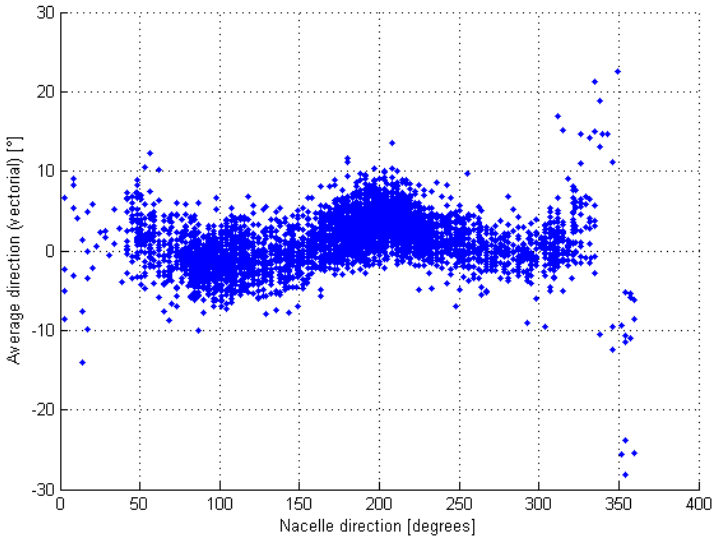

Figure 62: Yaw misalignment versus nacelle direction

Moreover, Wagenaar et al. have compared yaw misalignment measurements: *This Wind Iris yaw misalignment measurement was validated against the ground-based LiDAR near the mast (MM3). These measurements show an average yaw misalignment of about -3.5 degrees at hub height, which is very close to the offset obtained with the Wind Iris.*[65]

While these findings adds some trust to the yaw misalignment measurement by the Wind Iris, the desired accuracy in the order of 1 degree has not yet been thoroughly tested in literature. Therefore an experiment is recommended involving the Wind Iris on a static mast, pointed towards a met mast with a wind vane, as shown in Figure 63. By comparing wind direction measurements, the accuracy of the yaw misalignment measurement can be determined.

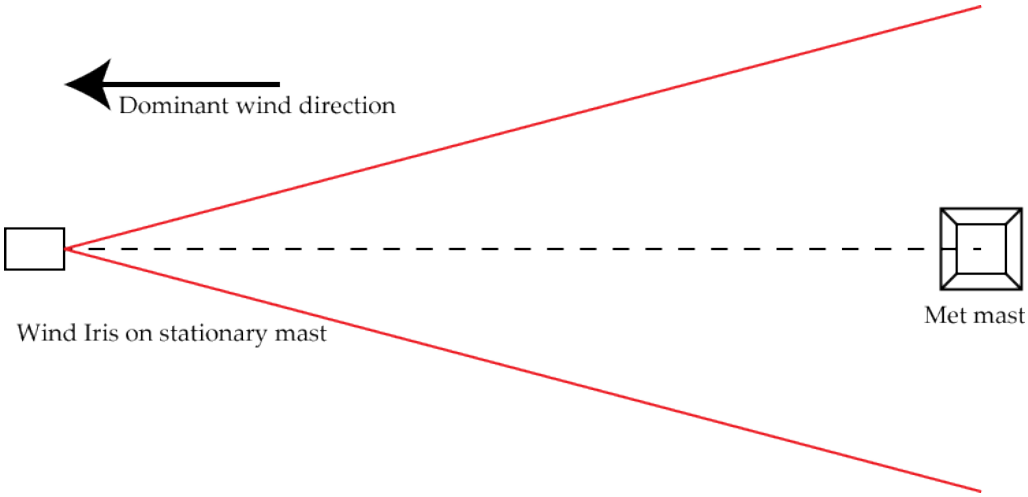

Figure 63: Proposed experiment to validate Wind Iris yaw misalignment measurement

In this experiment, ideally the masts are around 100m apart, since this is an appropriate distance to measure yaw misalignment at. The lidar namely has difficulty taking measurements closer than 80m, but further away the wind direction might not be representative for the virtual wind direction at the turbine. By placing the lidar on a mast directly downwind of the met mast, the lidar takes measurements on either side of the mast, as close as possible to the wind vane. With a half opening angle of 15 degrees, this means that the measurement points of the lidar are 54m apart. As such the mast is not interfering with the flow at the lidar measurement points.

16 WEATHER CHARACTERISTICS DURING CAMPAIGN II

This chapter discusses general wind and weather conditions during the second measurement campaign.

16.1 WEATHER

Autumn 2014 (September, October, November) was exceptionally warm, dry and sunny, according to the Royal Netherlands Meteorological Institute (KNMI). The average temperature at De Bilt was 12.4° instead of the normal 10.6° (normal being the average in 1981-2010). There was also less rain than normal, 136mm instead of 243mm, and more sunshine: 376 hours instead of 320 hours. Both the high temperature and little rain can be attributed to high pressure zones dominating the weather. The only real exception was the storm of October 21st, with wind speeds near shore of 9 Bft[56]. December 2014 was also relatively warm, although it started out cold. Precipitation was close to average: the first days were dry but were followed by dynamic and windy conditions. A storm passed by on 12 December with up to 30mm of rain. The first snow of the winter fell on 27 December. The number of sunshine hours was close to average[22].

16.2 WIND ROSE

A wind rose is plotted in Figure 64, which is based on sodar measurements during campaign II. Comparing this wind rose to Figure 8 illustrates that turbine 9 faces the wind freely most of the time, i.e. it is not often in the wake of other turbines. It would only be facing turbine wakes if the wind direction is between NNW and NE.

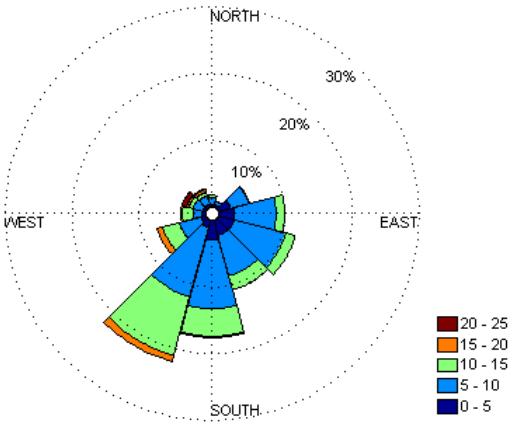

Figure 64: Wind rose during campaign II, based on sodar data (m/s)

16.3 WIND DISTRIBUTION

A wind speed distribution during campaign II is made with the sodar measurements at 65m and it is shown in Figure 65. Comparing this to the wind speed distribution during a whole year (i.e. campaign I, Figure 10) shows that during campaign II, the shape factor k is higher. This could be a seasonal effect, considering that September-December typically has more wind and less calm weather than a whole year on average.

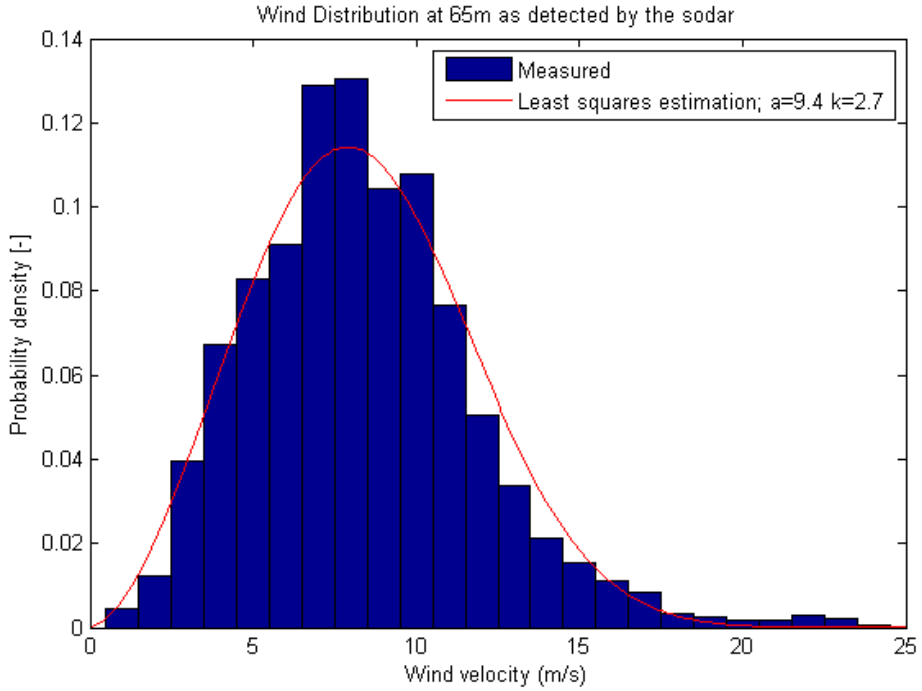

Figure 65: Wind speed distribution during campaign II

17

POWER CURVE (RESEARCH OBJECTIVE II)

The second research objective is to *determine the power curve based on lidar*. This is achieved by including the produced power as logged by the scada system (a parameter called *activepower*). Some initial power curves were already plotted using sodar and the nacelle anemometer in Chapter 9, but in this chapter the topic will be explored in more detail.

17.1 FIRST GLANCE

The first power curve plotted using the nacelle-based lidar data is shown in Figure 66. It is based on the data between 18 september and 2 november, and all measurement points of the lidar (filtered for 160m in front of the turbine) are shown in red. Also included in the graph is the contracted power curve (black), the median of the measurements (yellow) and the binned averages with confidence intervals based on the standard deviation of the measurements (blue).

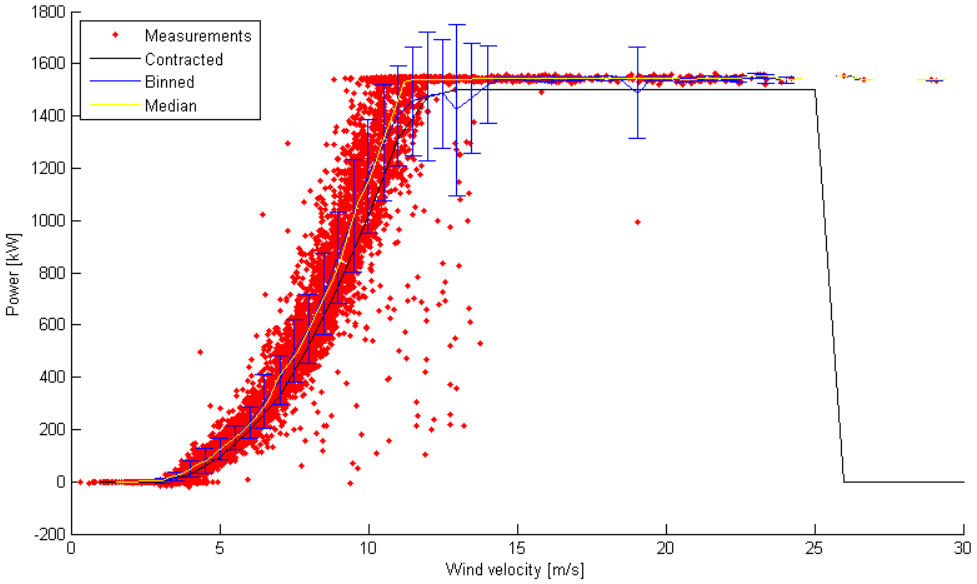

Figure 66: A first power curve plotted using lidar data (h=65m, d=160m)

This initial plot has a couple of peculiarities. First of all the rated power as measured is approximately 3% higher than contracted, around 1545 kW versus 1500 kW respectively. Secondly, there is a cloud of data points below the contracted power curve, seemingly restricted by a maximum wind speed of 14 m/s (except for the point at 19m/s and 996kW). Third and finally, the median as plotted captures the trend of the contracted (i.e. expected) power curve very well, better in fact than the binned average, as recommended by the IEC.

Digging a little deeper in this first result reveals that the cloud below the contracted power curve and below 14 m/s is strongly related to the measured yaw misalignment, as shown in Figure 67. In this plot the red scatter plot is the same as before (i.e. all lidar data at 160m), but also shows the data points as filtered for absolute yaw misalignment smaller than 2 degrees, in blue. This shows that the entire outlying cloud has disappeared, suggesting that there is indeed a relationship between yaw misalignment and power. However, it must be noted that these points might just as well be invalid measurements (in either the turbine data or lidar data) or have some other underlying relationship. This could be checked by examining the sodar data, comparing data from different distances and/or examining individual outliers.

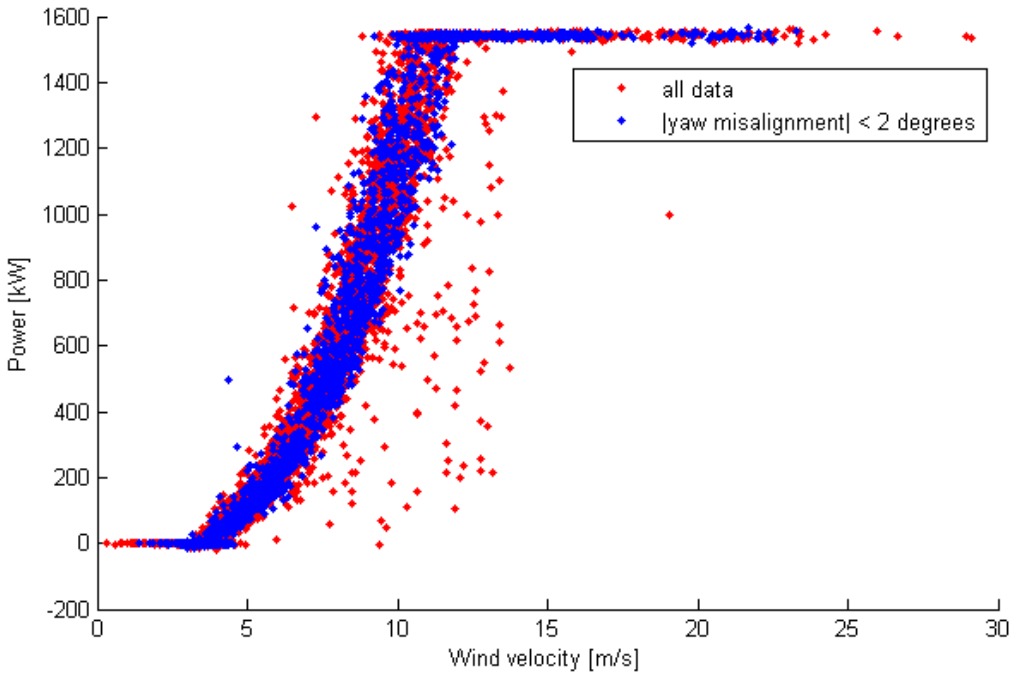

Figure 67: Power curves with and without restriction on yaw misalignment

To gain a little more understanding of the outliers, the red point located at V=19.7m/s P=996kW is examined. This data point has the time stamp 22 October 14:50, and this allowed other data from this moment to be retrieved. It turns out the nacelle anemometer, as well as the lidar (distances 80, 120, 240, 320 and 400m) all measured a wind speed around 10.5 m/s as opposed to 19.7 m/s. Moreover, this individual data point has exceptionally high turbulence intensity (4.2) and a very low HWS availability (0.46). All this makes it evident that the lidar has taken an invalid measurement. It also suggests that HWS availability might be a suitable parameter to filter data with. To get an idea of how much data would be filtered, a histogram is made of HWS availability, as shown in Figure 68. This plot shows that most data points have high availability, so relatively little data is lost when filtering.

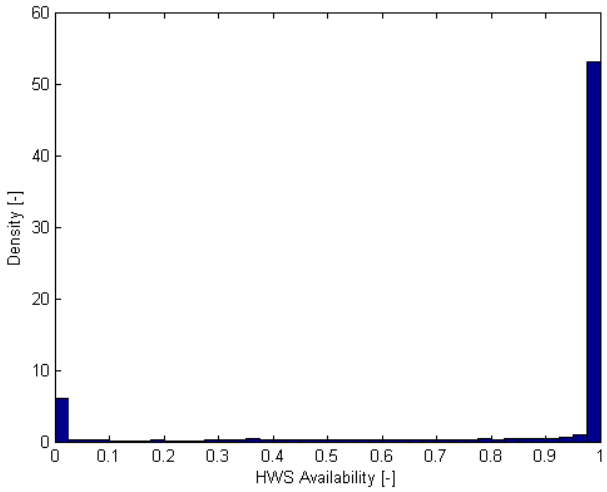

Figure 68: Histogram of Horizontal Wind Speed (HWS) availability of 10min average lidar data

Once again the power curve can be plotted, this time for all yaw misalignment, but filtered for a minimum HWS availability of 0.98, as shown in Figure 69. This filter removes around 23% of the data, including most of the cloud below the power curve. All in all it seems this cloud below the power curve is related to a perceived yaw misalignment as well as low availability.

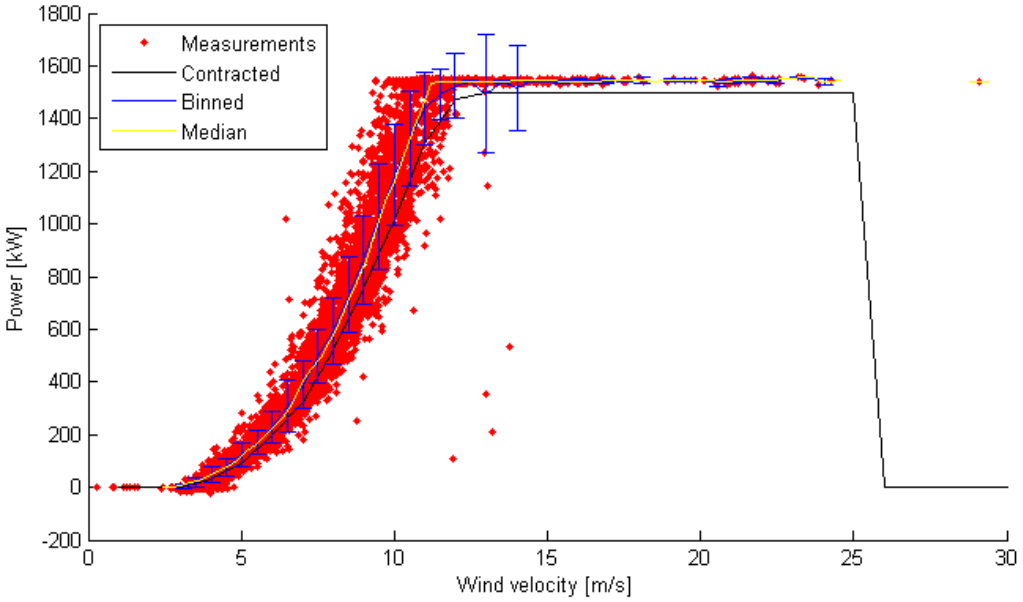

Figure 69: Power curve plotted using lidar data (160m in front of the turbine) filtered for minimum HWS availabity of 0.98

The disappearance of the cloud below the power curve for both low yaw misalignment (Figure 67) and high HWS availability (Figure 69) suggests a relationship between the two. In fact, this could suggest that the lidar has difficulties detecting yaw misalignment (i.e. if the turbine is under yaw misalignment, HWS availability drops). To investigate this relation a bit further, Figure 70 was plotted, for a distance of 80m to the lidar and wind speed above 4 m/s (cut-in). This plot illustrates that detection of yaw misalignment is not necessarily related to measurement uncertainty. In fact, towards to right of Figure 70, where availability is high, there are plenty of data points indicating yaw misalignment. Histograms of yaw misalignment are discussed in Section 18.2, which reaffirm that it is indeed possible to detect yaw misalignment with high availability.

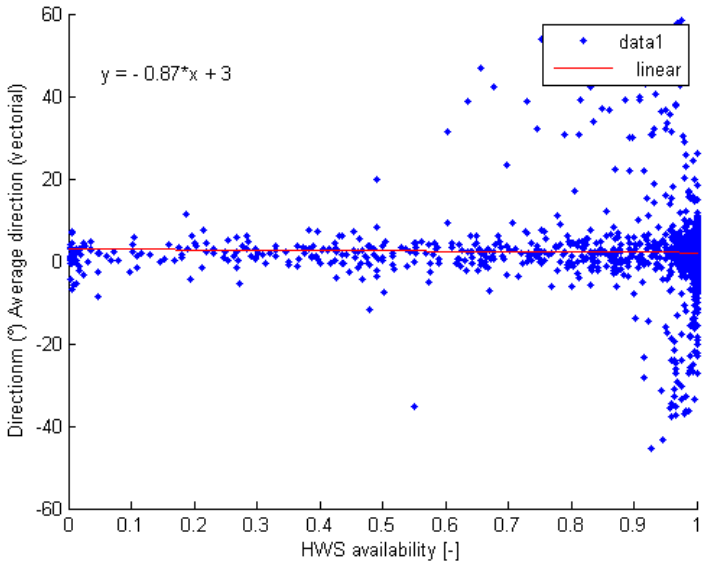

Figure 70: Yaw misalignment plotted against HWS availabity to investigate the certainty with which yaw misalignment is measured

Regarding the measured rated power of around 1545 kW instead of the expected 1500 kW, it seems there is no clarity within Vattenfall as to what causes this peculiarity. Site manager Tycho noted that this is not the first case of turbines producing more than specified. Moreover, data analysts and scada engineers don't know what could cause the higher produced power. It seems the most reliable approach to power measurement is the installation of an independent, IEC-compliant power measurement.

17.2 EFFECT OF DENSITY

With help of the nearby KNMI station or the on-site sodar (both measuring pressure and temperature) it is possible to take the air density into account in the power curve. The equation for power, Equation 10, can be rewritten using the swept area ($A = \pi r^2$) and ideal gas law ($p = \rho RT$), as shown in Equation 11.

$$P = C_p \frac{1}{2} \rho V_\infty^3 A \tag{10}$$

$$P = C_p \frac{1}{2} \frac{p}{RT} V_\infty^3 \pi r^2 \tag{11}$$

Taking this into account allows for the power to be calculated, if the density were $\rho = 1.225\ kg/m^3$, i.e. normalized power. This is shown in Equation 12.

$$P_{normalized} = P \frac{1.225}{\rho} = P \frac{1.225}{\frac{p}{RT}} \tag{12}$$

Alternatively, this method allows the power at the site to be predicted, given a power curve at standard conditions (i.e. $\rho_{std} = 1.225\ kg/m^3$), as shown in Equation 13[59].

$$P_{site} = P_{std} \frac{\rho_{site}}{\rho_{std}} \tag{13}$$

However, the correction according to Equation 13 is only applicable to stall regulated turbines[59], since it also affects the rated power. For instance, the turbines at Slufterdam have a rated power of 1500 kW, but if the density of the air is $\rho = 1.2\ kg/m^3$, the rated power will still be 1500 kW, whereas Equation 12 predicts it will be 1469 kW.

An alternative to this method is shown in Equation 14, which is a recommendation by the IEC[26] for pitch controlled turbines. This equation alters velocity instead of the density, hence keeping the predicted rated power the same.

$$V_{site} = V_{std} \left(\frac{\rho_{std}}{\rho_{site}} \right)^{\frac{1}{3}} \tag{14}$$

However, the IEC method shown in Equation 14 can overestimate the AEP by 5%[59]. The power curve namely has a $P \propto \rho V^3$ relation for low wind speeds, but this proportionality does not apply for higher wind speeds below rated, since the blades start pitching. Therefore, Svenningsen proposes a method as shown in Equation 15[59], where m is a function of wind speed, according to Figure 71. A large pool of power curves from most of the large manufacturers was used to determine m as a function of wind speed[58]. A comparison is

made between the IEC method and Svenningsen's method in Figure 72[58]. The method was found to reduce the error to 1%[59].

$$V_{site} = V_{std}\left(\frac{\rho_{std}}{\rho_{site}}\right)^{\frac{1}{m}} \tag{15}$$

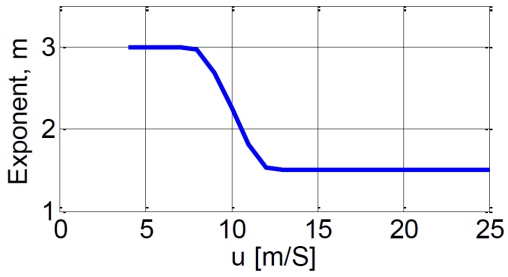

Figure 71: Proposed variation of m with V for power curve estimation according to Svenningsen[59]

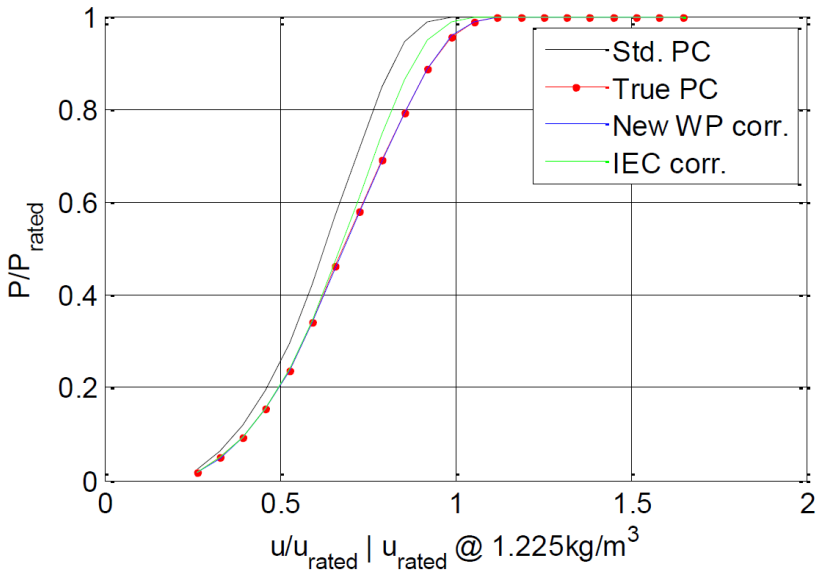

Figure 72: An illustration of the difference between Svenningsen's method and the IEC correction. The black power curve (PC) is the standard PC at 1.225 kg/m^3, to which corrections are applied. The red PC is the "true" air density specific power curve at 1.0 kg/m^3 calculated by the manufacturer using a full aeroelastic model of the turbine. The green PC is the standard PC corrected using the IEC61400-12 method and the blue curve is corrected using Svenningsen's method[58]

To get an initial impression of how density influences turbine performance, density is plotted against temperature, as shown in Figure 73. This plot was created by computing density from temperature and pressure measurements by the sodar and using the ideal gas law. It illustrates that a high air temperature is related to a low air density, as expected. The difference between high and low air density is around 9%, hence also directly impacting the produced power below rated power by 9%. However, since power curves are usually based on stan-

dard density ($\rho = 1.225 kg/m^3$), the maximum deviation from the contracted power curve will be in the order of 7%.

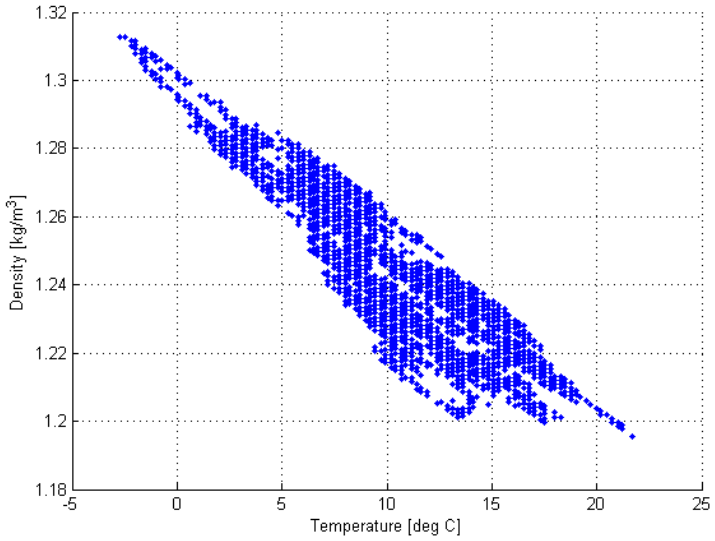

Figure 73: Density plotted versus Temperature as computed using sodar measurements

Svenningsen's method was rewritten to compute the standard velocity (v_{std}) from the site's velocity (v_{site}), and then implemented using Matlab's stepfunction *heaviside*, as shown below.

```
m = 3-3*heaviside(vsite - 8)+(-(3/8).*vsite+6).*heaviside(vsite-8).*
    heaviside(12-vsite)+1.5*heaviside(vsite-12);
vstd = vsite.*(1.225./density).^(-1./m);
```

The resulting power curve is shown in Figure 74, along with the original measurements. The plot shows that the spread in data points is reduced slightly, but there still is significant spread between the data points. In fact, the data point which was corrected the most was shifted by just 0.43 m/s.

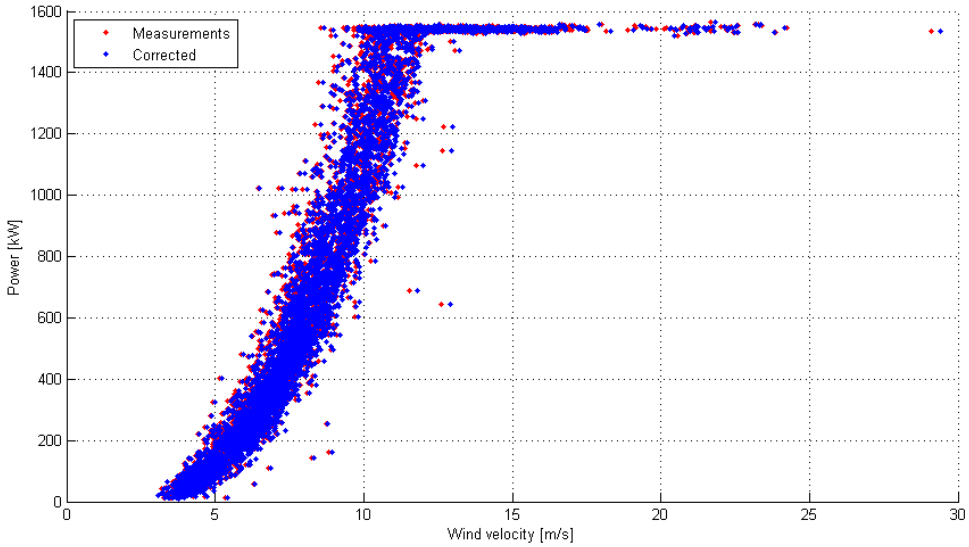

Figure 74: The measured power curve (lidar h=65m, d=160m) and power curve corrected for measured density (sodar) using Svenningsen's method[59].

17.3 THE POWER COEFFICIENT C_p

By combining data from the sodar (pressure and temperature), the lidar (wind velocity) and the turbine itself (power and rotational speed), it is possible to plot a Cp-lambda curve. This is shown in Figure 75, where the power coefficient is calculated according to Equation 16. Moreover, the power coefficient can be plotted against wind speed, as shown in Figure 76, and the tip speed ratio can be plotted against wind speed, as illustrated in Figure 77. All plots are made with lidar data at 320m, filtered for HWS availability > 0.98 and the turbine available.

$$C_p = \frac{P}{\frac{1}{2}\frac{p}{RT}V_\infty^3 \pi r^2} \tag{16}$$

The plots reveal that the turbine does not have a constant tip speed ratio below rated power. This can be explained as the turbine has a doubly-fed asynchronous generator with wound rotor and slip rings[17]. The speed can therefore be adjusted in a range of approximately $\pm 30\%$ around the synchronous speed, resulting in a rotor speed range of approximately 12-20 RPM, as shown in Figure 78. As a result, the turbine can operate at the optimal tip speed ratio between 6 and 10 m/s, as shown in Figure 77.

Moreover, the calculated power coefficient exceeds the Betz limit of 0.59 in numerous 10 minute intervals, which suggests that a measurement or calculation could be flawed.

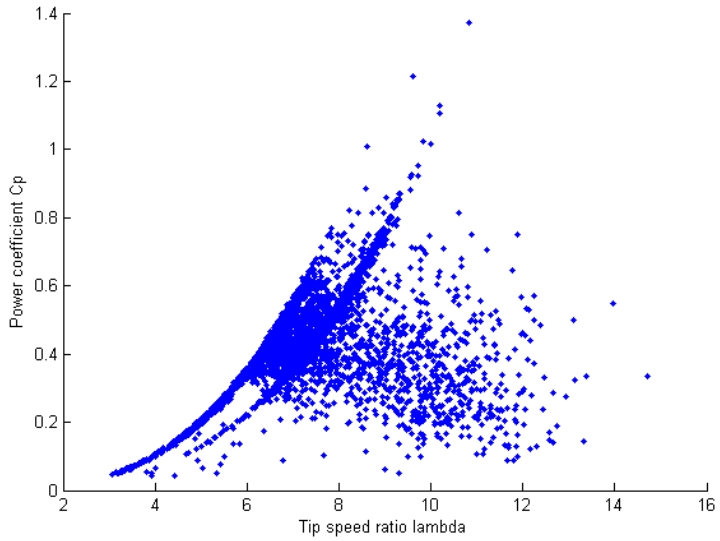

Figure 75: Cp-lambda curve

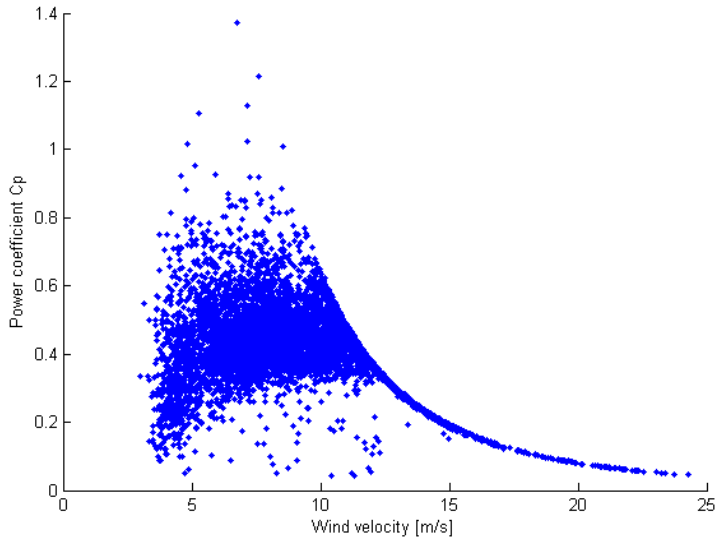

Figure 76: Cp-V curve

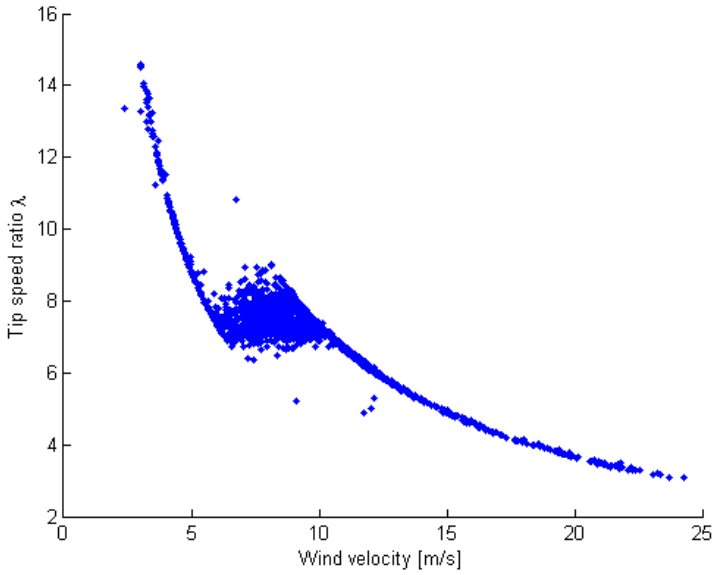

Figure 77: lambda-V curve

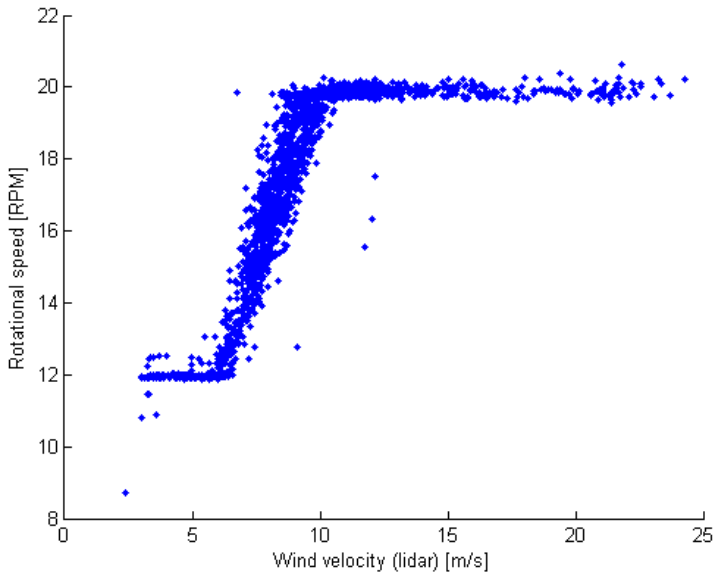

Figure 78: Rotational speed versus horizontal wind speed

The measured Cp-V plot in Figure 76 can be compared by those found by Hunter et al.[24] for an Enercon 40, as shown in Figure 79 and Figure 80[24]. The curves follow the same pattern and have similar spread characteristics: below rated power, the data points form clouds with similar shapes, and above rated power, the data points follow a smooth curve with very little spread. The figures by Hunter et al. suggest that site complexity has a drastic impact on the amount of spread between the data points. Moreover, at the moderately complex site, C_P values are found up to 0.7, similar to the case of Slufterdam (Figure 76).

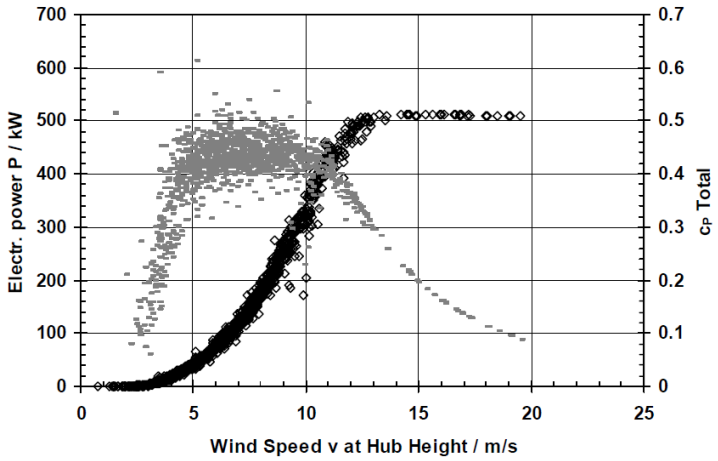

Figure 79: Raw power of the Enercon 40 versus wind speed data for the flat onshore site at Inte, near the German North Sea coast[24]

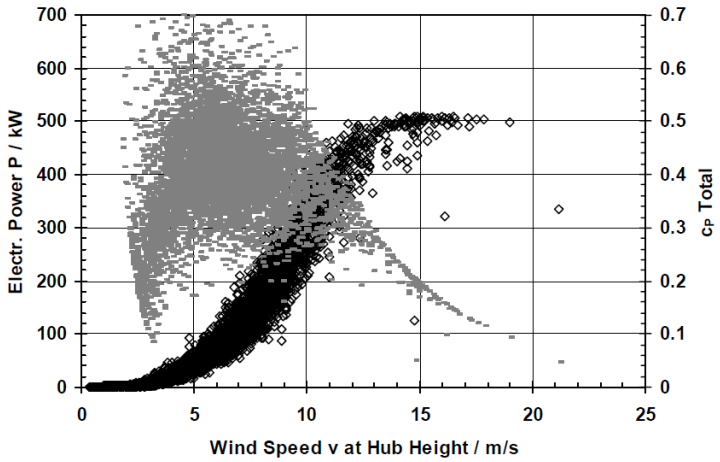

Figure 80: Power curve raw data of the Enercon 40 in moderately complex terrain near the German town Schmidt in the Eifel mountains, with met mast without site calibration[24]

Moreover, Villanueva Lopez has created a scatter plot using an IEC compliant met mast as shown in Figure 81[64], using color to indicate turbulence intensity in %. This plot also shows significant spread in the region below rated wind speed.

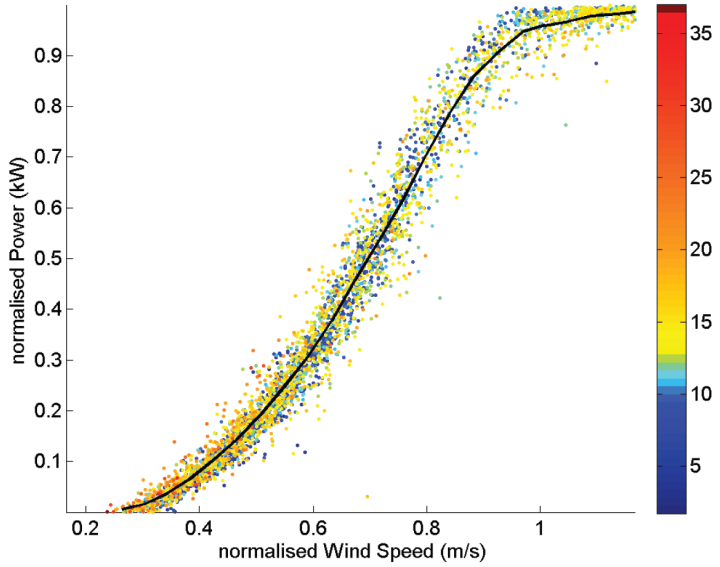

Figure 81: Power curve scatter plot as measured by Villanueva Lopez[64]

Instead of plotting the power curve, it is also possible to calculate the velocity from measured power using the contracted power curve. This is achieved by interpolating the contracted power curve and using it as a look-up table. For instance, if the produced power during one 10 min interval is 876 kW, it is possible to deduce that the wind velocity must have been around 9.5 m/s. However, this only applies below rated power, since produced power is around 1500 kW for wind speeds between rated and cut-out.

The method is applied to the entire data set, and the calculated wind velocity is compared to the wind velocity as measured by the lidar in Figure 82, and as measured by the nacelle anemometer in Figure 83. In this method, filtering the lidar data for signal quality is less trivial, and so there still is one major outlier left in the plot (lidar speed approx. 28 m/s). Nonetheless, the method is useful since the result can be analyzed with a linear regression. In the plot with the nacelle anemometer wind speed, Figure 83, it is remarkable how close the gradient of the linear regression is to one and how neatly the scatter seems trimmed for low C_P (i.e. upper side of the cloud). In both plots color is used to identify data points with $C_P > 0.59$ (i.e. above the Betz limit).

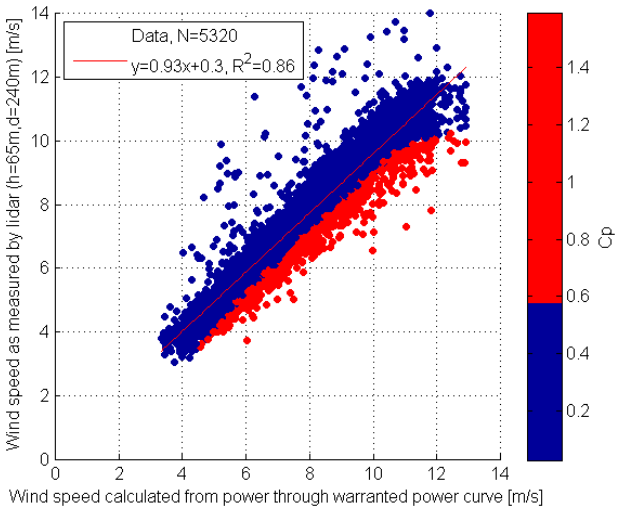

Figure 82: Measured wind velocity (lidar) versus calculated wind velocity (through measured power production and contracted power curve)

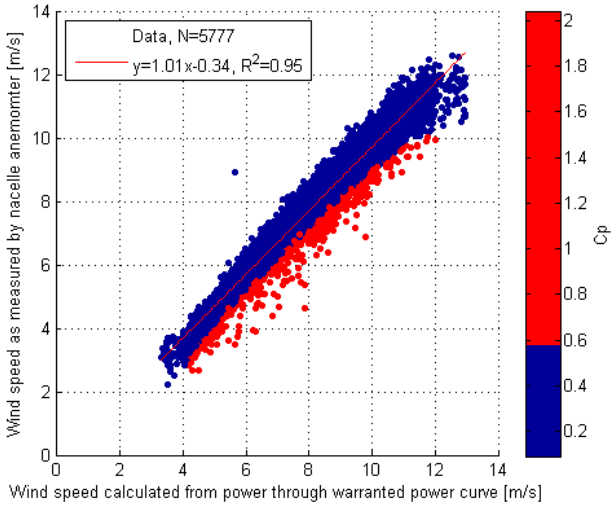

Figure 83: Measured wind velocity (nacelle anemometer) versus calculated wind velocity (through measured power production and contracted power curve)

17.4 POWER CURVE PER WIND DIRECTION

To examine what the wind direction does to the power curve, a method similar to that of Section 18.7 is written. Essentially, the power curve is plotted for a specific range of nacelle directions, for instance between 0 (i.e. North) and 20 degrees. The fit $P = \beta V^3$ is then computed using the least squares method for all data points below rated power, since only this part of the power curve will be affected. The value for β is stored and the procedure is repeated for nacelle directions between 1 and 21 degrees, then 2 to 22 degrees, and so forth, until all directions are examined. However, the value of β is only accepted if the coefficient of determination R^2 is higher than 0.7, there are at least 15 data points in the fit, and the horizontal wind speeds as measured by the lidar and sodar differ by no more than 0.5 m/s. By dividing all β by the highest value of β, the plot is normalized to one, and the result is shown in Figure 84.

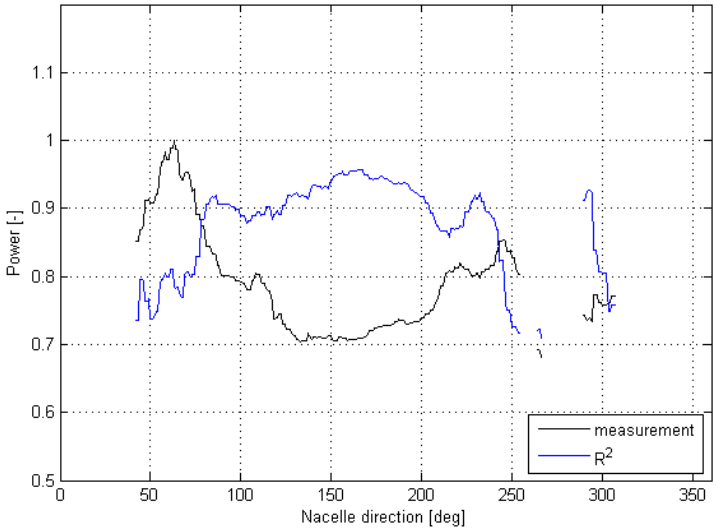

Figure 84: Normalized power below rated for varying nacelle directions, where abs(sodar-lidar)<0.5 m/s

Normally, one would expect a better power curve for free stream (90-300 degrees), but the opposite seems to be the case. The best power curve is found for nacelle directions between 50 and 70 degrees, and the worst between 110-200 degrees. From 210-250 degrees the power curve is relatively good again, possibly because the turbine faces the sea freely. These unexpected results are also found when filtering such that the maximum difference between the wind speed as measured by the lidar and by the sodar is 0.1 m/s, as shown in Figure 85. Note that this power curve analysis was not applicable to wind directions between $250° - 42°$, due to a lack of data points and/or a R^2 below 0.7.

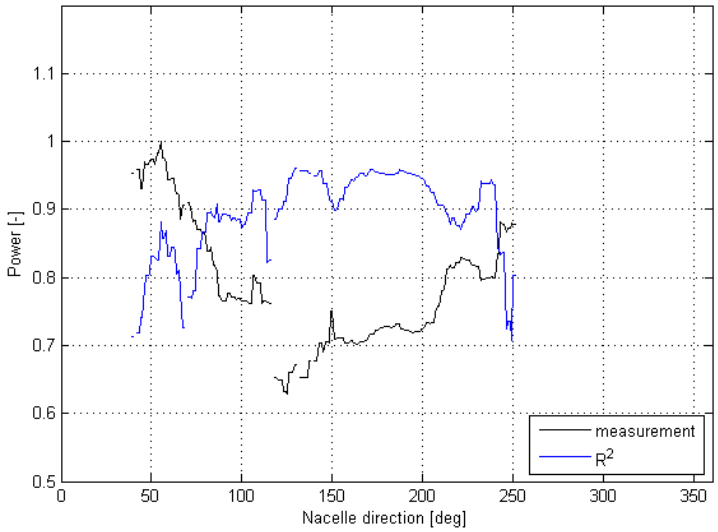

Figure 85: Normalized power below rated for varying nacelle directions, where abs(sodar-lidar)<0.1 m/s

From Figure 85, the best and worst wind directions are determined to be $42° - 62°$ and $118° - 146°$ respectively. To get an idea of what the power curves and fits look like for these best and worst wind directions, Figure 86 is included below. These plots show that there are plenty of data points, but that the spread is significantly more for the favorable wind direction, resulting in a lower R^2. The favorable and unfavorable wind sectors themselves are illustrated on a map in Figure 87.

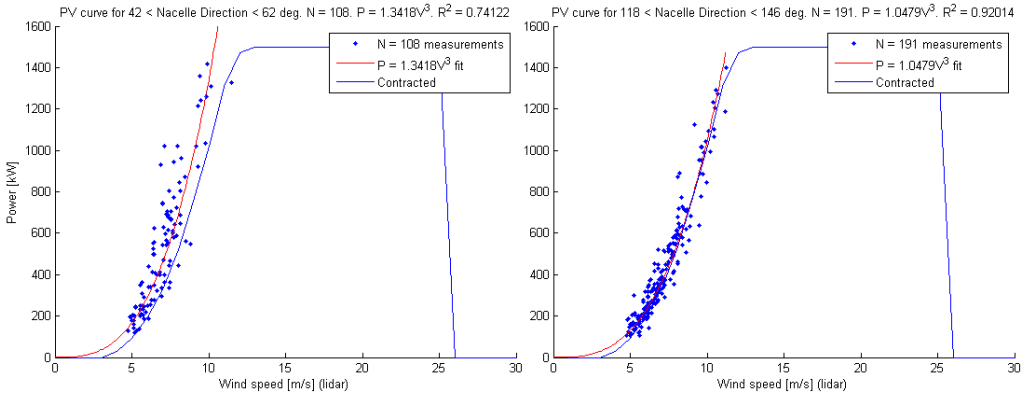

Figure 86: Power curves for the best and worst wind directions, with abs(sodar-lidar)<0.5 m/s

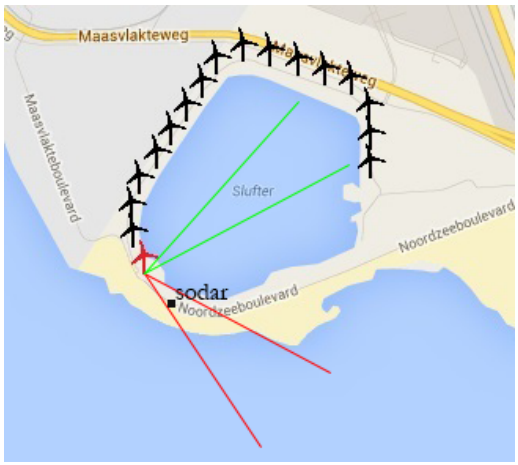

Figure 87: The favorable and unfavorable wind directions illustrated on a map. Green sector is favorable ($42° - 62°$), the red sector is unfavorable ($118° - 146°$)

For future reference, the map in Figure 87 also shows that the turbine under investigation (turbine 9) is in the wake of other turbines if the wind is coming from $340° - 67°$. The sodar is in the wake of other turbines from $315° - 60°$. Furthermore, the sodar is directly in the wake of turbine 9 if the wind has direction 315°. By averaging the wind speeds at varying height for this wind direction, the wake of turbine 9 can be visualized. The wind shear (i.e. wind profile) can be plotted similarly, but now using free stream wind directions. The two are compared side by side in Figure 88, normalized using the highest average wind speed. This figure shows that the wake effect is strongest at hub height, as expected.

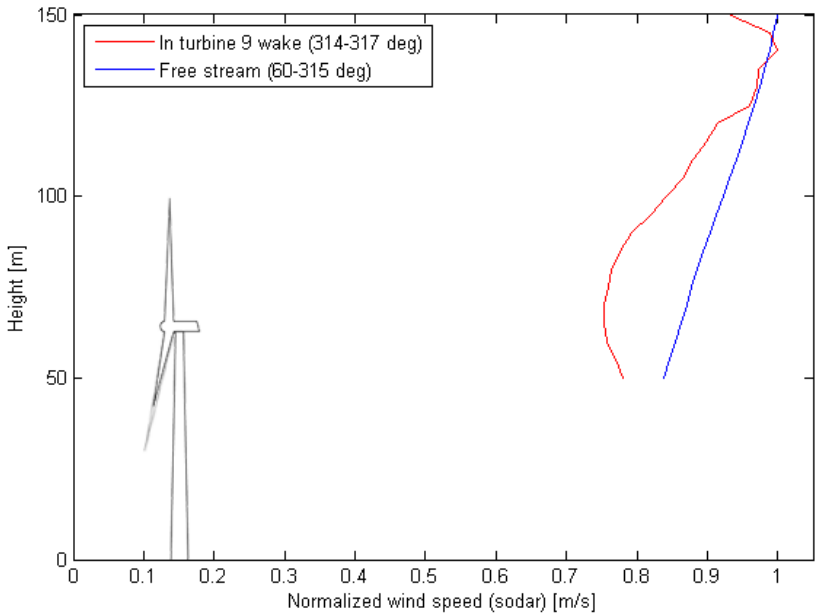

Figure 88: The wake of wind turbine 9 visualized 3.3D downwind by the sodar (red), and the free stream wind profile (blue). The wind turbine is drawn to scale

To see if wind shear is causing the contradictory results from Figure 85, the *Rotor Equivalent Wind Speed* (abbreviated as REWS) is used. This is calculated from the wind speeds measured by the sodar, since this instrument measures at altitudes between 20m and 150m in steps of 5m. Unfortunately all data from 30m-45m altitude was logged as invalid (value 9999 m/s), so the wind shear was extrapolated linearly. This data is required, since the rotor sweeps between 29.45m and 99.95m. After extrapolating the data, the rotor equivalent wind speed at every 10min point is calculated according to Equation 17[68]. Essentially, the swept area is cut in segments horizontally with area A_i, such that the segment's boundaries are in-between the velocity measurement heights. The total swept area is A, R is the rotor radius, H is hub height and z is height.

$$v_{rews} = \left(\sum_{i=1}^{n_h} v_i^3 \frac{A_i}{A} \right)^{1/3} \tag{17}$$

where

$$A_i = \int_{z_i}^{z_{i+1}} c(z)\,dz$$

and where

$$c(z) = 2\sqrt{R^2 - (z-H)^2}$$

The resulting rotor equivalent wind speed is the hub height velocity that represents the wind velocity on the entire rotor, in accordance with how much power is actually present in the swept area of the turbine. By dividing this more representative value by the hub height wind speed, an idea is created of the difference between the two. However, to get an idea of how much power is present, versus how much power is present according to hub height wind velocity, this ratio is cubed: $(v_{rews}/v_{hub})^3$. An average of this ratio is computed for every wind direction, and the result is shown in Figure 89. This figure illustrates that if the sodar is downstream of the closest turbines, i.e. wind directions $300° - 340°$, the ratio is between 1.05 and 1.10, meaning that there is 5% to 10% more power available than the hub height wind speed would suggest. This effect can be traced back to Figure 88, which showed that the wake effect is strongest at hub height. Therefore the hub height velocity underestimates the power available and the $(v_{rews}/v_{hub})^3$ ratio is high. Figure 89 also shows that for directions $50° - 280°$ (i.e. free stream), the ratio is between 0.97 and 1.05, so V_{hub} can be considered acceptable.

Another effect which might be taking place at Slufterdam is the wake re-energizing effect as suggested by Clive[13]. This effect is illustrated in Figure 90, where the turbulent flow behind each turbine causes mixing with the high-velocity flow above the wake. This re-introduces energy to the wake, allowing downwind turbines to extract more energy than expected, hence contributing to the phenomenon of V_{hub} being unrepresentative for the power available in the wind. However, if the rotor equivalent wind speed is used, and the flow

conditions above the sodar are representative of the flow at the turbine (e.g. both in wakes), wind shear and wake re-energizing should not have an effect on the power curve.

Finally it must be noted that turbine 9 and the sodar are in the wake of other turbines for different wind directions, as shown in Figure 87, so Figure 85 and Figure 89 should not be compared directly.

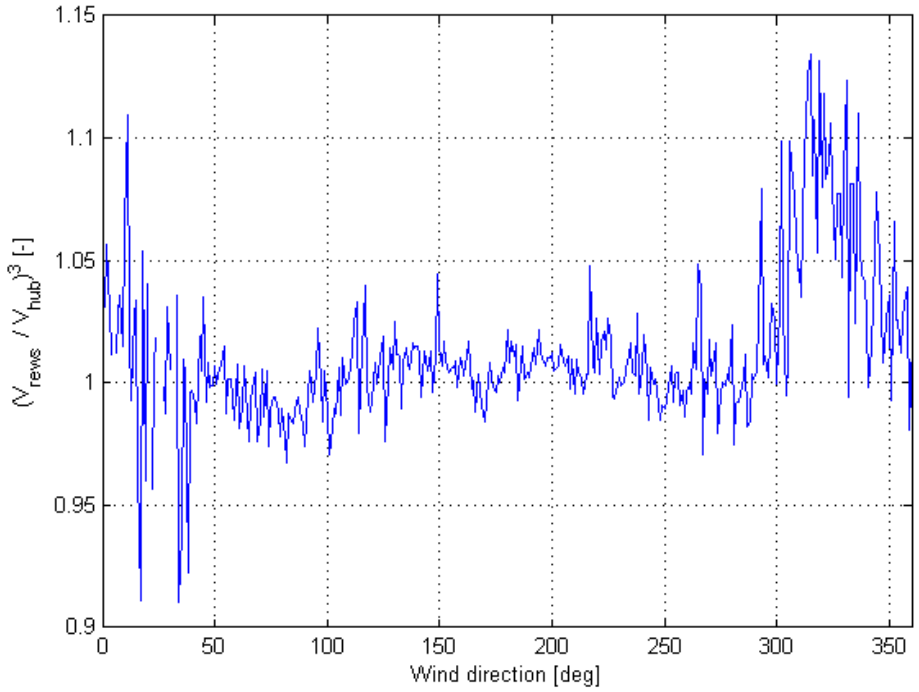

Figure 89: Ratio of power available according to rotor equivalent wind speed (REWS) to power available according to hub height wind speed

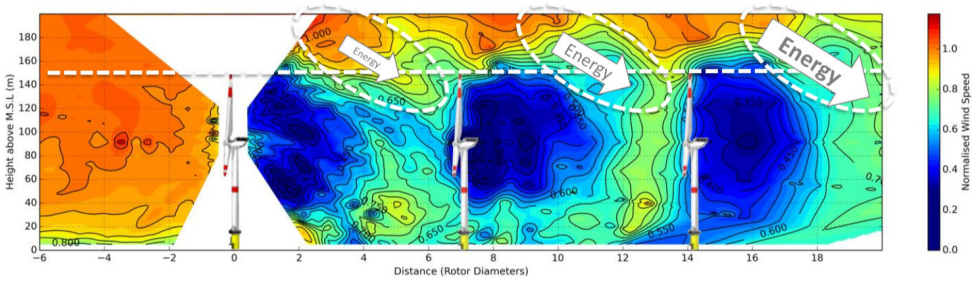

Figure 90: Wake re-energizing as hypothesized by Clive[13]

The method of Figure 84 is now repeated, but instead of using the lidar and sodar wind speeds, the rotor equivalent wind speed is used, as shown in Figure 91. As such, the effects of wind shear and wake re-energizing should be reduced. However, since the sodar is located about 235m southeast of turbine 9, the rotor equivalent wind speed is not appropriate for all wind directions.

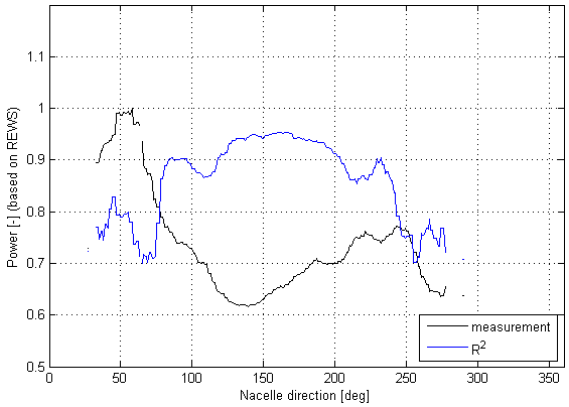

Figure 91: Normalized power below rated for varying nacelle directions, where the power curves are based on rotor equivalent wind speeds

This becomes clear from Figure 92. This figure shows the average Cp for all data points below rated power, for varying nacelle directions. This power coefficient is calculated using $C_p = \frac{2P}{\rho V_{rews}^3 A}$, where again the rotor equivalent wind speed is used, and the density is computed using the sodar's temperature and pressure measurements. The figure clearly shows that if the sodar is directly downstream of the turbine (direction 315°), the power coefficient peaks, with an average of up to 0.85, far above the Betz limit of 0.59. Nonetheless, the general pattern is similar to that of the previous analyses, where the turbine seemingly performs better when it is downstream of other turbines. For instance, there is a peak around 50°, where both the turbine and sodar are in wakes. Therefore it seems there are more factors affecting the power curve through wind direction than wind shear and wake re-energizing alone.

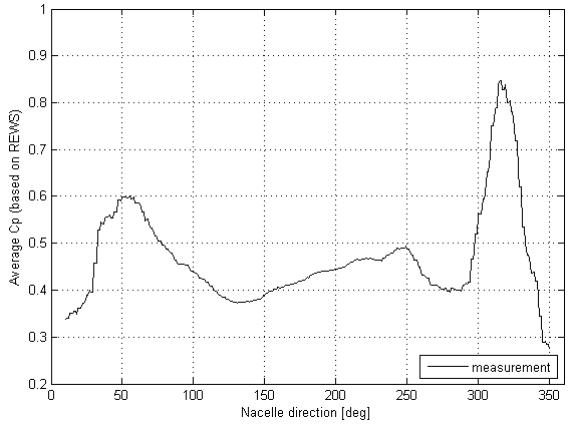

Figure 92: Average Cp per wind direction, based on rotor equivalent wind speed as determined with the sodar

To see if turbulence might be related to the previously discussed results, the turbulence intensity (TI) is calculated using the sodar's data, and shown in Figure 93. This figure illustrates that if the sodar is downstream of other turbines, the turbulence levels are increased. As expected, turbulence is lowest for free stream conditions, i.e. with wind directions $60° - 315°$. Increased turbulence is said to improve the tail of the power curve (low wind speeds) and deteriorate the power curve at the knee of the power curve (higher wind speeds, but below rated)[23]. However, it is questionable whether this effect is strong enough to account for the observed improvements around 50°.

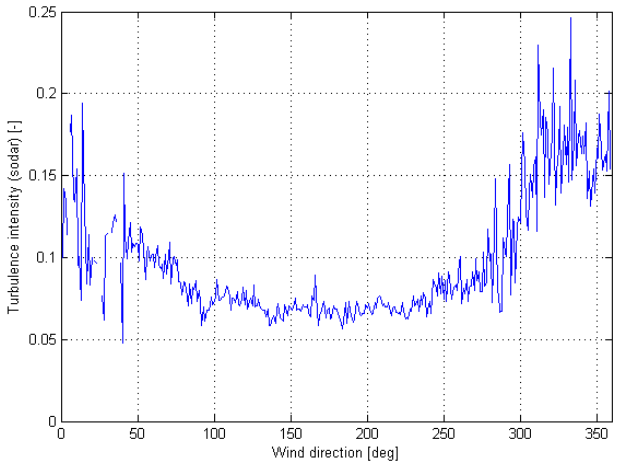

Figure 93: Turbulence Intensity (TI) per wind direction, based on sodar data

Another factor that might be of influence to the power curve is wind veer. This parameter is computed by subtracting the wind direction at 100m from that at 50m. The average wind veer is then calculated for varying wind direction and illustrated in Figure 94. In this figure, the effect of the dike can be seen as an increasing trend from $130° - 315°$. Moreover, the wind veer is strongest around 150° and relatively weak around 50°. Perhaps the combination of turbulence and wind veer can account for the variations of the power curve.

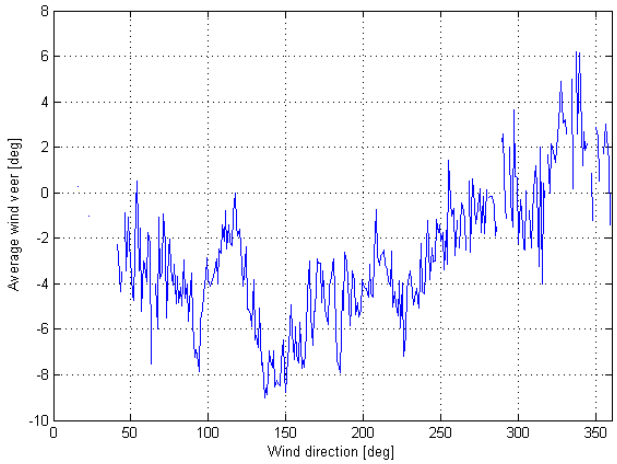

Figure 94: Average wind veer per wind direction between 50m and 100m, based on sodar data

17.5 CONCLUSIONS

As discussed in Chapter 15, the Wind Iris is able to measure average wind speed accurately, which is in agreement with literature. This means that since the Wind Iris is mounted atop the nacelle, it is able to constantly measure the wind speed 2.5D in front of the rotor, hence providing a reliable means of measuring the power curve. However, since there is some uncertainty around the SCADA signal of the turbine's power output, it is recommended that the nature of this signal is further investigated, or a second, independent power measurement is added. The latter option will also provide insight in the measurement uncertainty of the power signals.

A density correction of the data points was found to reduce the spread in the scatter plot slightly, but less than anticipated. Svenningsen's method for density correction[59] seems appropriate, but it seems the uncertainty in the measured power curve might be significantly larger than the correction itself. As a result, the method is useful, but probably more so for resource assessment in the development stage of wind parks.

When examining the power curve as a function of wind direction, it seems an improvement of the power curve occurs when the turbine is in the wake of upstream turbines with northeastern wind. While the upstream turbines might cause a reduction in wind velocity, it appears that the power produced at this reduced velocity is higher. Possibly, the hub height wind velocity is not representative of the wind in the swept area of the turbine, for instance because of wind shear and/or the wake re-energizing effect[13]. Analysis of the sodar data revealed that the rotor equivalent wind speed was significantly higher than the hub height wind speed when downstream of turbines. This indicates that when a turbine is in the wake of another turbine, more energy is available to it than the hub height wind speed suggests. However, repeating the analysis using the rotor equivalent wind speed revealed a similar trend. Another explanation could be the increased turbulence, which allegedly improves the power curve at low wind speeds[23]. Moreover, the wind veer is also found to be weaker in the wind sector where the power curve is better. In conclusion, the variations in power curve found for varying wind sectors might be attributable to wind shear, wind veer and turbulence, but separating the individual contributions of these factors is tentative.

18 TURBINE AND PARK GAINS (RESEARCH OBJECTIVE III)

The third research objective is to *determine how much Slufterdam west 09 and the park can gain from the installation of a nacelle-based lidar.* There are several ways in which a nacelle-based lidar can be advantageous to a wind park, but this chapter of the thesis focuses on detection of yaw misalignment and its effect on the power curve.

However, before discussing the analysis regarding yaw misalignment, it must be noted that the terms *yaw misalignment* and *yaw error* are discussed frequently in literature, even though reducing it is not evident. Therefore these terms do not imply that something is wrong with the turbine or that the performance can easily be improved. This is also addressed by Fleming et al., identifying two sources of yaw error: the first is that the wind direction changes more often than can be corrected for by the yaw controller. The second source of error is in the wind direction measurement, which is now typically done with a wind vane on the nacelle (i.e. in the wake of the blades). The second source is most easily addressed, since it requires little extra yaw motion. It could be done by either calibrating the existing system, or replacing it with a more accurate one[15].

18.1 YAW MISALIGNMENT AT A GLANCE

As discussed in Chapter 10, the Wind Iris is able to calculate the wind direction with respect to the nacelle and therefore assess if the turbine is aligned well with the wind. To get an initial idea of this measurement, the high-frequency data is illustrated in Matlab using animated plots. Considering that the data is logged at 1Hz, the refresh rate of the plot is also set to 1Hz, giving a true impression of the wind.

The first animated plot, of which a snapshot is shown in Figure 95, shows the wind speed and wind direction using bar plots as determined at 80, 120, 160, 240, 320 and 400 meters in front of the turbine. This animated plot turns out to be quite useful in getting an impression of the wind, especially the variations in wind speed.

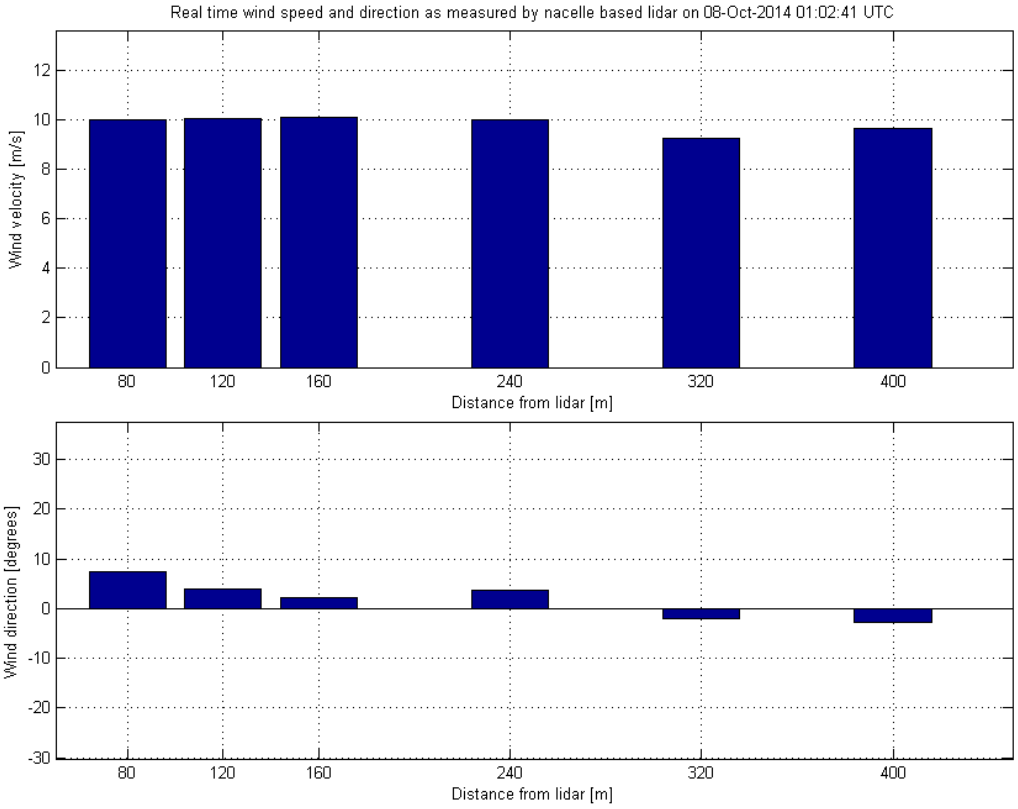

Figure 95: Snapshot of the animated bar plot, based on 1Hz lidar data

To get a better impression of the wind direction, another animated plot is made, as shown in Figure 96. In this view from above (with the lidar in the origin), blue vectors are shown representing the wind speed and direction. However, it must be noted that this plot assumes uniform flow in the y-direction, just like the lidar itself. For instance, the lidar measures line-of-sight velocity at two points at 400m in front of the turbine, 214m apart. Assuming uniform flow, the wind speed and wind direction can be calculated (as discussed in Chapter 10 and Appendix A), and plotted at x=400m. To get a better impression of the wind gusts, color is added, where green is low speed and yellow high speed. Streamlines are included to get an impression of the flow.

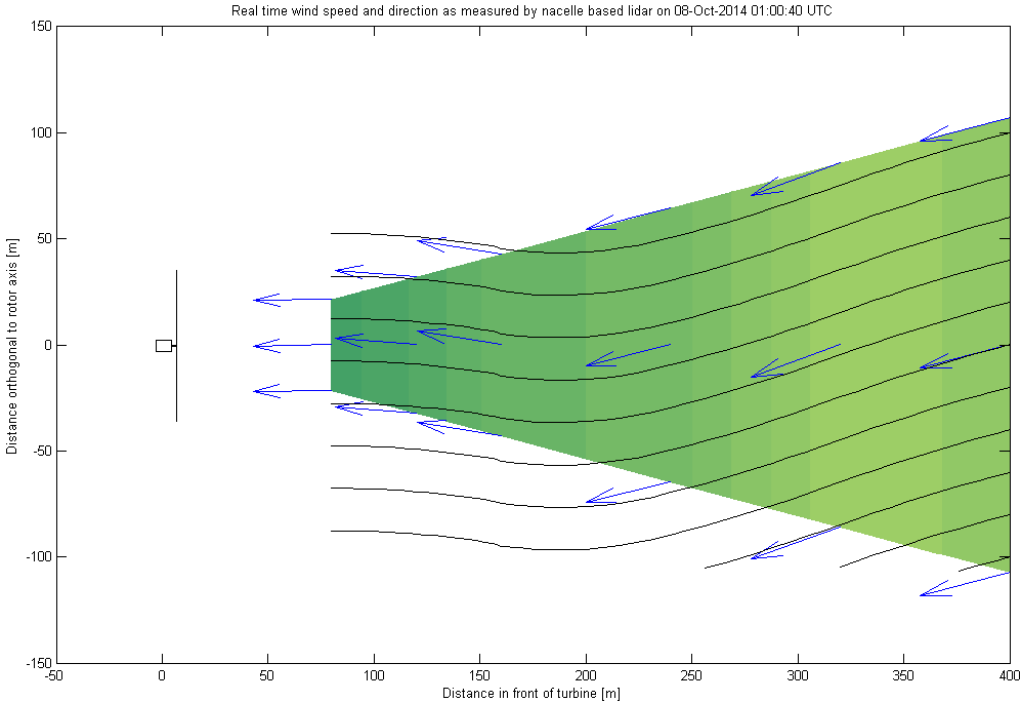

Figure 96: Snapshot of the animated streamline plot, based on 1Hz lidar data

18.2 YAW MISALIGNMENT BASED ON 10MIN AVERAGE DATA

Ten minute average lidar data can be used to create a histogram of the yaw misalignment, as shown in Figure 97. In this figure, yaw misalignment for wind speeds below 4 m/s is ignored and the measurements are taken 80m in front of the turbine. This plot illustrates that on average the turbine is aligned quite well. The mean yaw misalignment is in fact +1.5 degrees and the histogram shows relatively little spread.

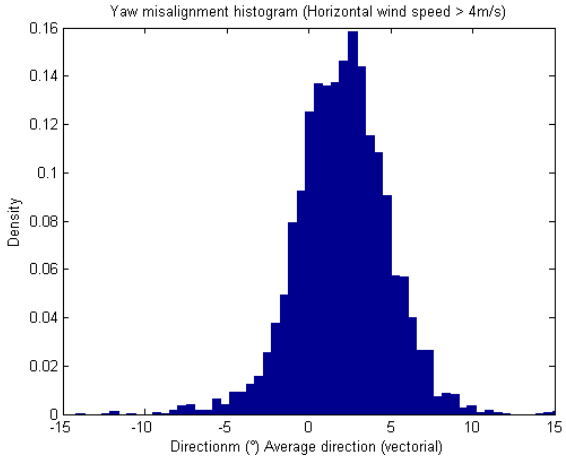

Figure 97: Histogram of yaw misalignment, based on 10 minute average lidar data

A similar plot can be made, but now also filtering for HWS availability (>0.98), as discussed in Chapter 17. The result is Figure 98, which shows that the trend is very similar to Figure 97, indicating that the Wind Iris is capable of detecting yaw misalignment with high availability. The mean yaw misalignment, filtered for HWS availability is still +1.5 degrees, the standard deviation is 3.4 degrees.

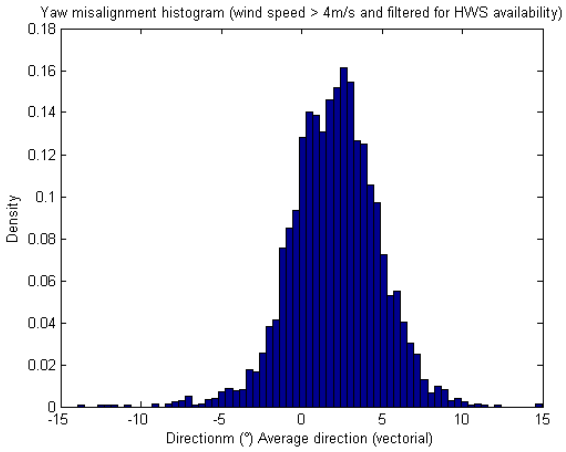

Figure 98: Histogram of yaw misalignment, based on 10 minute average lidar data. Filtered for minimum wind speed and HWS availability

For all histograms it must be noted that the "true" yaw misalignment spread will be smaller, due to the Wind Iris' random measurement error. The simulation in Appendix D illustrates that this error is probably larger than expected

(in the order of 4° as opposed to 0.5°). If this is indeed the case, Figure 135 gives a better impression of the spread.

18.3 YAW MISALIGNMENT BASED ON 1HZ DATA

Section 18.2 discusses the yaw misalignment as measured from the 10min average lidar data. However, it could well be that the averaging process (i.e. going from 1Hz measurements to 10min data) skews the results. To investigate this, a histogram of yaw misalignment based on 1Hz data is made, as shown in Figure 99, based on one hour of data from the afternoon of October 8th 2014. During this afternoon the wind was around 10 m/s from the south, meaning the turbine is facing the wind freely. The histogram reveals that indeed the mean of the instantaneous yaw misalignment is similar to mean yaw misalignment, considering that the bell curves of Figure 98 and Figure 99 have a mean of +1.5 degrees. However, the spread in the bell curve is much greater in the histogram of 1Hz data (i.e. Figure 99). This shows that the 10min data is useful for determining a mean yaw misalignment, but the spread strongly depends on the measuring frequency (1s or 10min) and the instrument's accuracy (Appendix D). Finally, the nacelle-based lidar's ability to measure mean yaw misalignment depends on how well the lidar is aligned with the rotor axis.

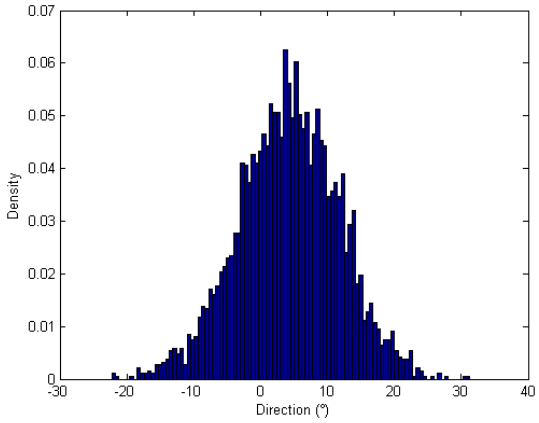

Figure 99: Histogram of yaw misalignment, based on 1Hz lidar data. Filtered for wind speed > 4 m/s and CNR > -15dB

18.4 COMPARISON TO SODAR ANALYSIS

Chapter 8 discussed a means of analyzing yaw misalignment with sodar and turbine measurements: by subtracting the direction of the nacelle from the direction of the wind as measured by the sodar, the yaw misalignment is obtained. It must be noted that both measurements must somehow have their directions calibrated, and so this method is much more suited to getting an idea of the maximum spread, rather than the mean yaw misalignment.

A histogram of yaw misalignment of turbine 8 based on sodar and turbine data was shown in Figure 24. Turbine 8 was chosen because turbine 9 had a nacelle

offset in the data of around 53 degrees, hence introducing more uncertainty in the histogram. Comparing Figure 24 to the histograms made with solely the lidar data reveals that the former indicates more spread than the 10min average lidar data (Figure 98), and a similar amount of spread as the 1Hz lidar data (Figure 99). This could be caused by the distance between the turbine and the sodar.

Moreover, it must be noted that the lidar measures the yaw misalignment much more directly: first of all, it is a local measurement: it measures the wind direction directly in front of the turbine, whereas the sodar cannot achieve this. Secondly, the nacelle based lidar is aligned directly with the rotor axis, greatly reducing the amount of uncertainty in the mean yaw misalignment.

In conclusion, the Wind Iris is suitable for determining the mean yaw misalignment through 10 minute or 1Hz data. When it comes to spread in the Wind Iris yaw misalignment histograms, one must take into account that the spread will depend on measurement frequency and the instrument's measurement accuracy. The spread will be more for high frequency data, but one can wonder if it is realistic to constantly be yawing the wind turbine, hence straining the yaw mechanism. Sodar and turbine data (the *scada/sodar* method) is less suited to measuring yaw misalignment, because it involves two alignment calibrations instead of one, and measures the wind direction further away from the turbine.

18.5 YAW MISALIGNMENT, ROTOR SPEED AND WIND SPEED

Fleming et al. and Kragh and Fleming observe a dependence of yaw misalignment on rotor speed[15][33], so an analysis is included for Slufterdam. A first impression can be based on Figure 100, where there is no clear relation. A trend line is included, indicating that there is indeed no clear dependence of yaw misalignment on rotor speed for this wind turbine. Moreover, the latest article from Scholbrock et al. revisit the previous observations: *"Another thing to note is that with the nacelle vane yaw controller, the yaw misalignment is not dependent on the rotor speed. This is in disagreement with what was found in [33], and is probably due to a new issue that was not present in 2011 when the data was collected for [33]."*[54]

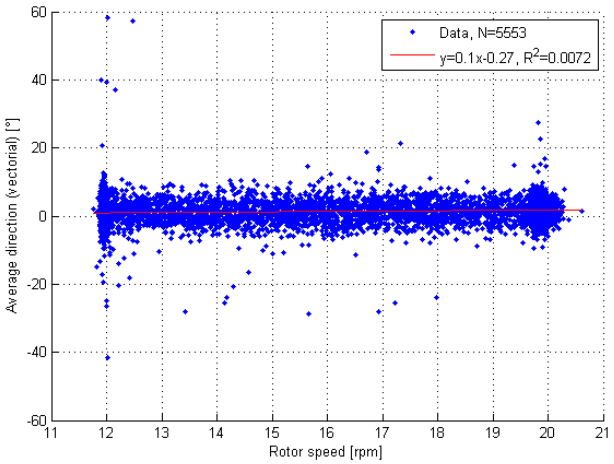

Figure 100: Scatter plot of yaw misalignment versus rotor speed

Unlike the apparent lack of dependence of yaw misalignment on rotor speed, plotting yaw misalignment against wind speed reveals there might be a connection. This is shown in Figure 101, where yaw misalignment and wind speed have been determined using the nacelle lidar at 80m in front of the turbine. Perhaps this dependence manifests itself like this because the turbine only varies its rotor speed for wind speeds between 6 and 10 m/s, as shown in Figure 78 and discussed in Section 17.3.

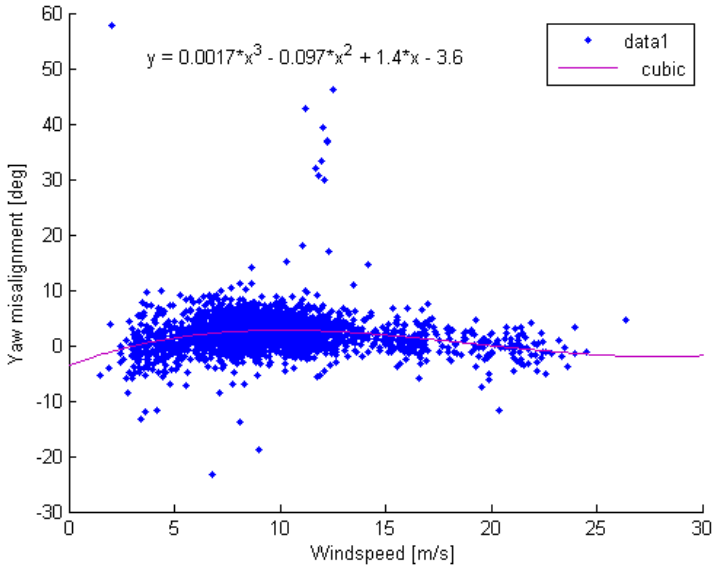

Figure 101: Scatter plot of yaw misalignment versus wind speed

It may seem tempting to take rotor speed or wind speed into account in the calibration of the yaw controller. However, examining Figure 101 more closely reveals that the dependence of yaw misalignment on wind speed is not that strong in the wind regime where it matters for the power curve (i.e. 4-12 m/s). In this regime the trend in yaw misalignment lies between $1 - 2.5°$.

18.6 YAW MISALIGNMENT AND OTHER VARIABLES

It seems that the perceived yaw misalignment is a random variable: it is normally distributed and has little or no relation to other variables (rotor speed, wind speed). However, when looking at the effect of yaw misalignment on produced power (Section 18.7), care must be taken to exclude the possibility of omitted variable bias (confounding). To that end the occurence of yaw misalignment is further examined. For instance, Figure 102 shows the dependence of yaw misalignment on the time of the day (filtered for HWS availability, turbine operating and wind speed above cut-in). More specifically, the day/night cycle has an effect on the stability of the atmosphere, due to heating/cooling of the land, air and water. Consequently, the turbine's ability to align itself with the wind could be affected. However, Figure 102 shows that neither the spread, nor the mean yaw misalignment is dependent on the time of the day.

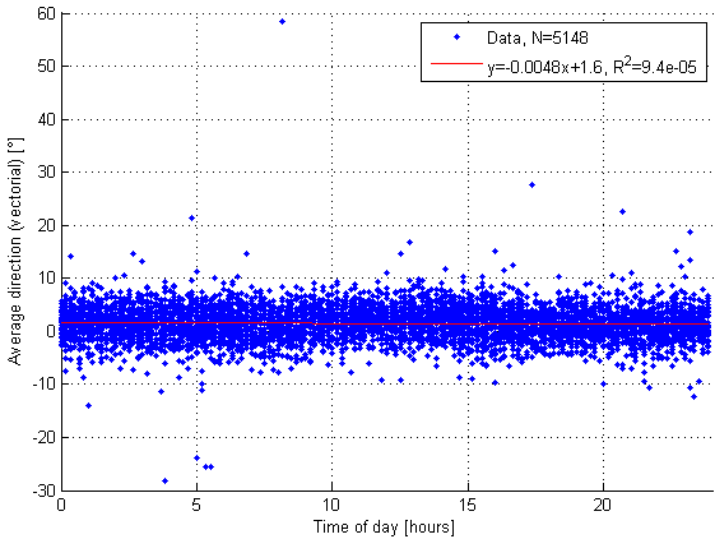

Figure 102: Scatter plot of yaw misalignment versus time of the day (hours)

Moreover, Figure 103 shows that there is a relationship between the perceived yaw misalignment and turbulence intensity, where both variables were measured by the lidar. Particularly, the spread in yaw misalignment increases with turbulence intensity. This comes as no surprise, as stable wind is easier to work with than unpredictable turbulent/gusty wind. However, another hypothesis is that the lidar has difficulty measuring turbulence and distinguishing yaw misalignment from inhomogeneous flow. This idea is supported by the findings in Section 15.3, where it was found that lidar might have difficulties measuring turbulence accurately. It is also in line with literature[70], as discussed in Section 15.4.

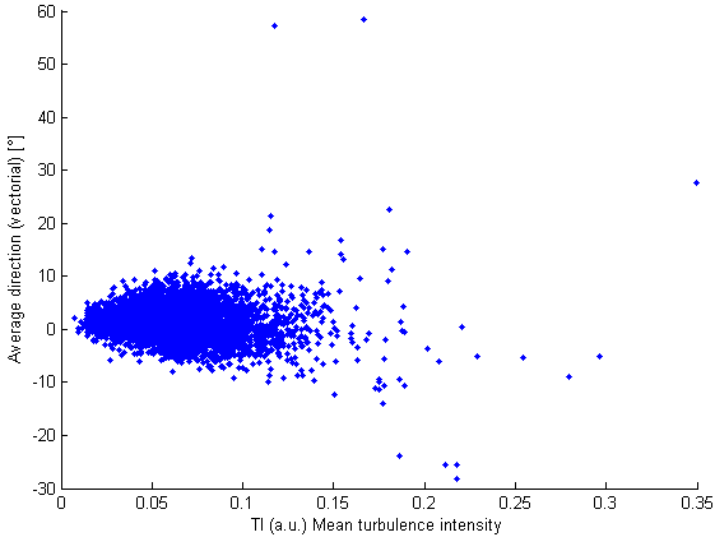

Figure 103: Scatter plot of yaw misalignment versus turbulence intensity as measured by lidar

18.7 EFFECT OF YAW MISALIGNMENT ON PRODUCED POWER

Several research institutes and companies suggest that the produced power of wind turbines can be increased by reducing the yaw misalignment. To facilitate these performance improvements, wind consultants and instrument manufacturers are offering their services and products.

To see if yaw misalignment leads to a decrease in power in practice, power curves are plotted for a sequence of yaw misalignment bins as measured by the Wind Iris. First, the velocities are corrected for density, as discussed in Section 17.2. Next, a cubic least squares fit is calculated for all data points below rated power, as illustrated in two examples in Figure 104. In these plots the green points represent power below rated power, the black line is the least squares fit ($P = \beta V^3$), and the blue points are the residuals. For each fit the coefficient of determination (R^2) is also calculated and shown in the plot's title.

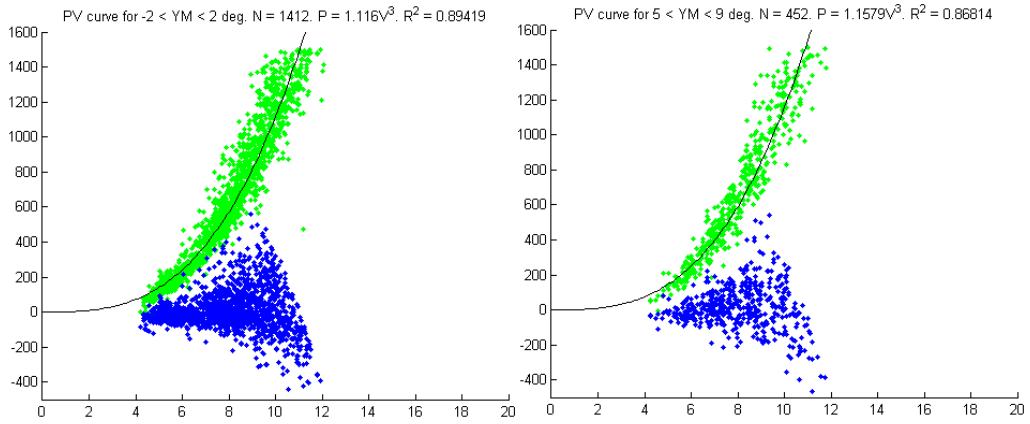

Figure 104: Example of two cubic power curve fits for yaw misalignment bins [-2 2] and [5 9] (left and right respectively)

The next step is to plot the cubic fit parameter (β) against its corresponding yaw misalignment bin (normalized for zero yaw misalignment), as shown in Figure 105. In this plot the coefficient of determination (R^2) is also plotted, as well as the $cosine$, $cosine^2$ and $cosine^3$ as mentioned in literature[15][47][49]. The data points in the analysis are filtered for numerous factors: the turbine must be operational, the data point must have a 1Hz availability of more than 98%, the wind speed must be between 5 and 11 m/s, the turbine produces less than rated power, and the wind direction (as measured by the sodar) is between 100° and 250°, to make sure there is nothing upstream of the turbine. The wind speed and yaw misalignment measurements are taken by the Wind Iris 240m in front of the turbine. Finally, β is only plotted if R^2 for a certain yaw misalignment bin is more than 0.7 and there are at least 50 data points in the plot.

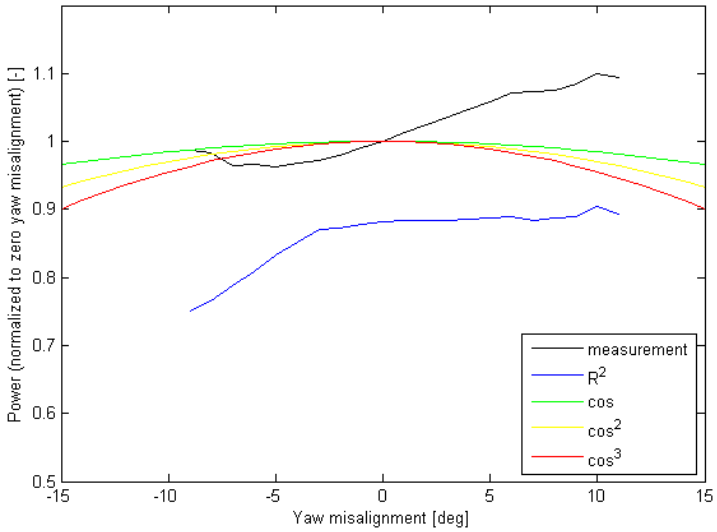

Figure 105: Scatter plot of yaw misalignment versus rotor speed

Interestingly, Figure 105 seems to suggest that the produced power increases slightly for a small positive yaw misalignment. At this moment it is worthwhile to mention that a positive yaw misalignment means that the wind is coming from the right, as shown in Figure 106. The turbine rotates clockwise (when facing the turbine with the wind in your back), so a positive yaw misalignment means that the local inflow angle is favorable (higher angle of attack) at the top of the swept area and unfavorable (lower angle of attack) at the lower side of the swept area. Combined with wind shear this might be an explanation for a higher yield at small positive yaw misalignment, since the favorable effect takes place in higher wind speed than the unfavorable effect, hence resulting in a net favorable effect.

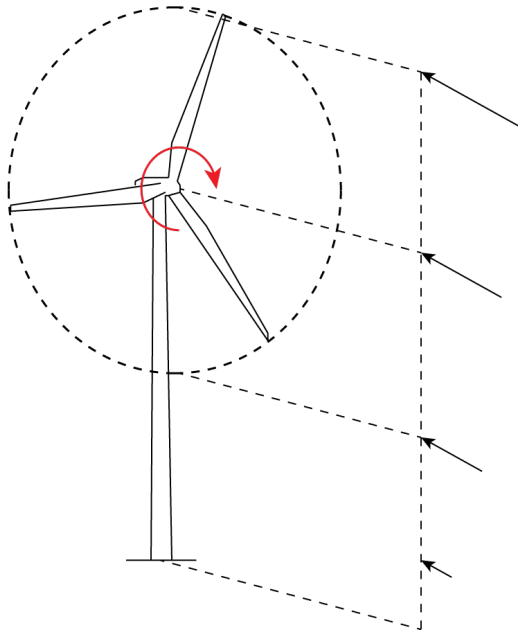

Figure 106: A clockwise rotating turbine under a small positive yaw misalignment

A comparison of this result can be made to literature, like shown in Figure 107[49]. In this plot, much greater yaw misalignments are included than in Figure 105. Nonetheless, the slight increase in power at small positive yaw misalignment is also visible in this graph.

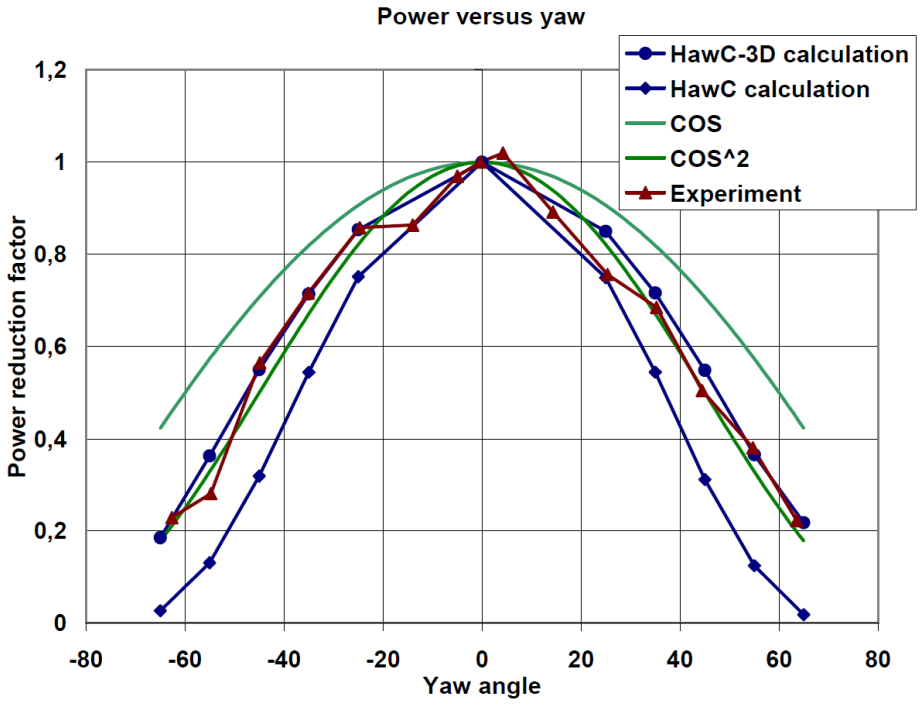

Figure 107: Relative power reduction as measured and simulated for a 75kW wind turbine at 8-9 m/s[49]

Moreover, Wagenaar et al. have also used the Wind Iris and a similar method resulting in Figure 108[65]. They noted an offset of 2.5 and 3.3 degrees, i.e. the "best" yaw misalignment is not necessarily 0 degrees. However, from the paper it does not become clear if the used sign convention for yaw misalignment is the same as in Figure 105.

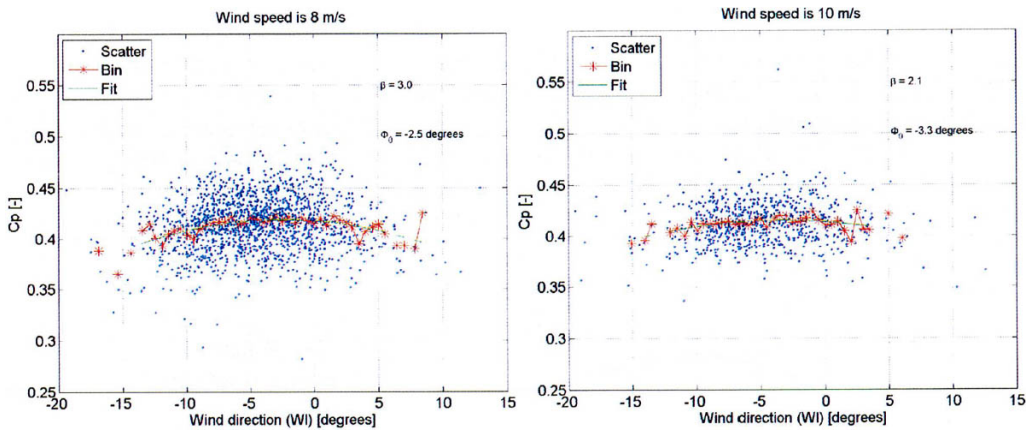

Figure 108: Cp values against Wind Iris wind direction for 10 minute averages (blue), binned averages (red) and fit on the data (green). Wind speed values between 7 m/s and 9 m/s (left) and 9 m/s and 11 m/s (right)[65]

To make a more direct comparison to the results of Wagenaar et al. and investigate the effect further, a method similar to that of Wagenaar et al. is applied[65]. The power coefficient is calculated for every data point using $C_p = \frac{2P}{\rho V^3 A}$, where the density is computed using the sodar's temperature and pressure measurements. The same filters are used as before and the results are shown in Figure 109. The graph on the right of Figure 109 is the same as the red plot in the left graph, except with different axes. From these figures the same trend can be seen as before: a slight increase in power for small positive yaw misalignment, and a slight decrease in power for small negative yaw misalignment.

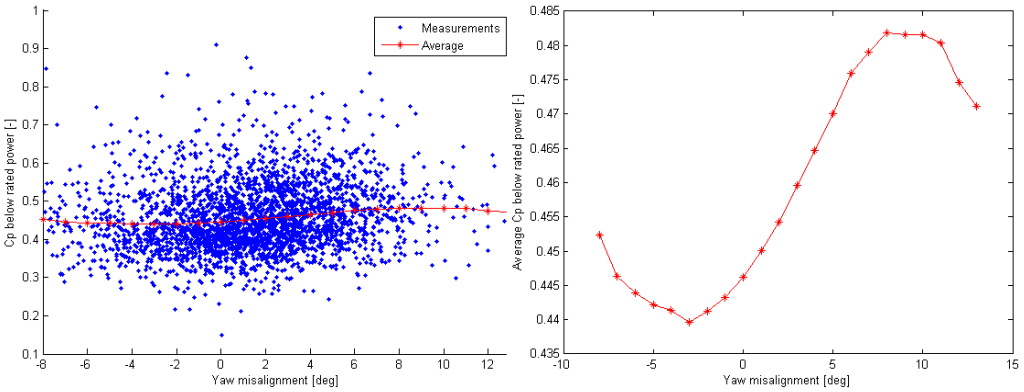

Figure 109: Left: Cp values against yaw misalignment for 10 minute averages (blue) and average (red). Right: Average Cp against yaw misalignment

However, there are a number of notes to be made about these analyses and their results in Figure 105 and Figure 109. First of all, the results are quite sensitive to the filters that are applied. Moreover, as discussed in Appendix D, there are reasons to believe that the Wind Iris cannot measure yaw misalignment as accurately as anticipated. This also means that it is possible that the true yaw misalignment is rarely outside the range $-2°$ to $6°$, as shown in the histogram from the simulation, Figure 135. These observations combined mean that the analyses are tentative outside the range $-2°$ to $6°$ and there is significant uncertainty in the yaw misalignment measurement, deeming the analyses less reliable. Finally, one can wonder if the 10 minute average data points are the most suitable for investigating the effect of yaw misalignment on the power curve. The wind and nacelle probably rotate in a smaller time domain such as 1-2 minutes, making this a more suitable time step.

In conclusion, it is quite difficult to accurately and definitively determine the impact of yaw misalignment on the power curve. Therefore, more research regarding this topic is recommended. More specifically, an experiment could be carried out where the (full scale) turbine is put under an intentional yaw misalignment using an offset in the yaw controller. By regularly changing the yaw misalignment (e.g. every hour) to a new value, the impact from other variables is minimized. However, if a small positive yaw misalignment turns out to be beneficial to the power curve, the impact on loads must be assessed before intentional yaw misalignment can be recommended.

18.8 PARK GAINS

There are several ways in which implementation of the Wind Iris can be beneficial to an entire wind park. For instance, the Wind Iris could be applied sequentially to all turbines, hence allowing the performance of all turbines to be analyzed. This scenario is further discussed in Chapter 20, including an analysis from a financial point of view. However, another option is to use the Wind Iris as the input for a feed-forward controller of the yaw and pitch systems, essentially anticipating the incoming wind. Perhaps such an implementation could be extended to the entire wind park, where data from the most upstream turbine is used to predict wind conditions for the downstream turbines.

18.9 CONCLUSIONS

Wind turbine 9 of Slufterdam West was found to have an average yaw misalignment of $+1.5$ degrees. While the Wind Iris seems like a suitable instrument for measuring yaw misalignment, the accuracy in its direction measurement has not been proven. In fact, a simulation in Appendix D suggests that the standard deviation of the Wind Iris' measurement might be in the order of four degrees, hence causing an overestimation of the spread in the yaw misalignment histogram. It is unknown how accurately the Wind Iris can measure the mean yaw misalignment, but this is also expected to be in the order of 4 degrees. To investigate the accuracy of the instrument further, an experiment is proposed in Section 15.4.

Yaw misalignment was found to be correlated to turbulence intensity, i.e. a higher turbulence intensity is related to greater spread in yaw misalignment. While this finding is in line with expectations, it must be noted that the Wind Iris is not the best instrument for measuring turbulence. It would therefore be interesting to compare the measured yaw misalignment to a reliable and independent turbulence intensity measurement, such as a cup anemometer on a met mast.

Furthermore, it seems yaw misalignment is affected by wind speed, but not significantly in the regime where it really matters, i.e. between cut-in and rated wind speed. Moreover, in 2011 Fleming et al. found yaw misalignment to be dependent on rotor speed[15], but this relationship was not found on the Slufterdam. The latest AIAA paper by this research group revisits the topic and no longer finds this relationship, which they speculate to be due to an issue not present during the original measurement campaign from 2011[54].

Produced power is said to be dependent on yaw misalignment through a $cosine$, $cosine^2$ or $cosine^3$ of the yaw misalignment[15][47][49]. To investigate this relationship, two methods are used to examine the impact of naturally occurring yaw misalignment on the power curve below rated power. Results indicate a slight improvement of the power curve for small positive yaw misalignment and a deterioration of the power curve for small negative yaw misalignment.

However, the methods are quite sensitive to input parameters, and the Wind Iris might not be able to measure yaw misalignment as accurately as anticipated. Therefore at this stage no indisputable conclusions can be drawn, and further research regarding the topic is recommended.

19

BLOCKAGE (RESEARCH OBJECTIVE IV)

The fourth research objective is to *estimate the blockage effect/compression zone in front of the turbine and compare to models/theory*. Not only is this topic interesting from a theoretical point of view, it will also give insight in the optimal measuring distance for power curve verification.

19.1 THEORY

Below rated power the ideal induction is $a = 0.33$ according to the actuator disk model as shown in Figure 110. The nature of the lidar measurements make it an ideal tool to investigate what the blockage, i.e. reduction of wind speed in front of the turbine, looks like in practice.

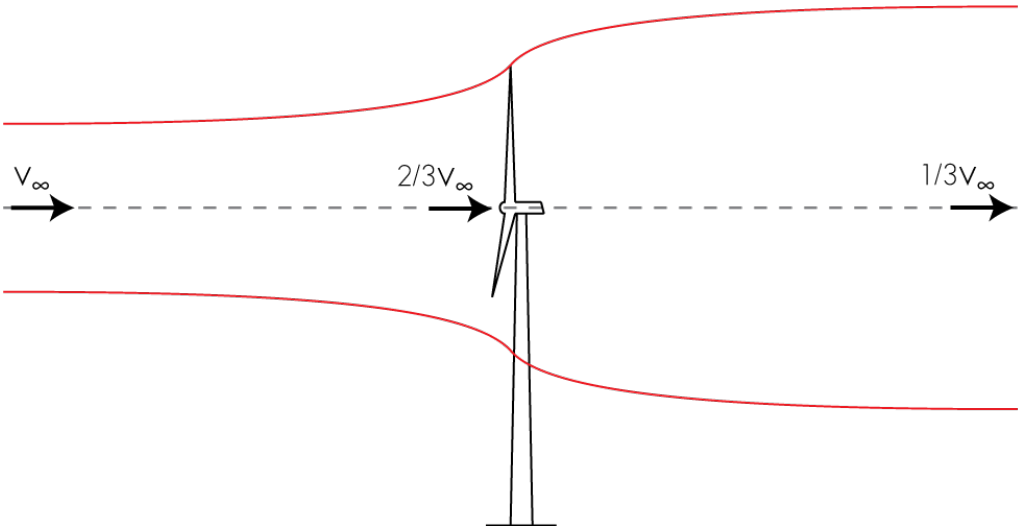

Figure 110: Side view of the actuator disk model

The theoretical wind speed in front of the turbine can be found by calculating the induced velocity with the Biot-Savart law, resulting from helical tip vortices stretched to infinity downstream[41]. This leads to Equation 18 where $\xi = -x/R$ and the induction factor $a = 0.33$[41].

$$\frac{u}{u_\infty} = 1 - a\left(1 + \xi(1+\xi^2)^{-\frac{1}{2}}\right) \tag{18}$$

19.2 RESULTS

A plot of the mean measured wind speed is shown in Figure 111, which also includes the theoretical wind speed according to Equation 18. In this plot wind speeds are only included if they are below rated wind speed (12 m/s). The figure reveals that the measurements follow the same pattern as the theory, except that the maximum mean wind speed is reached around 9R, instead of approaching it asymptotically.

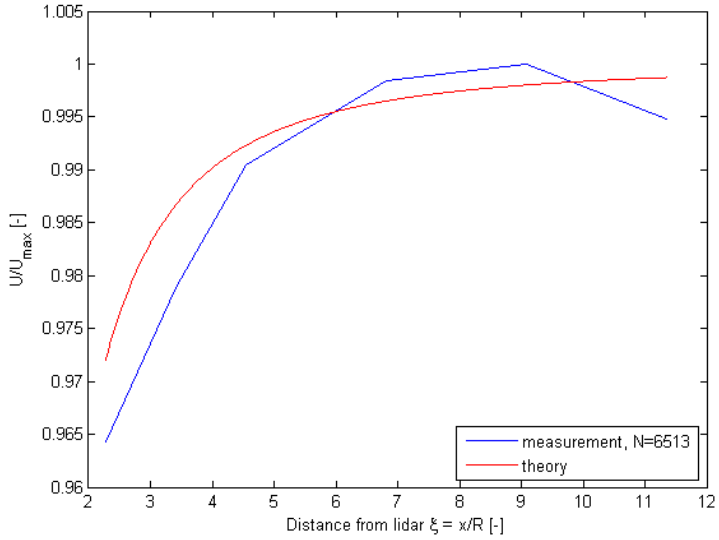

Figure 111: Blockage as measured by lidar and a theoretical plot[41]

The relatively good fit of Figure 111 is put into perspective when adding the standard deviation as error bars, as shown in Figure 112. These large error bars can be explained from the large variations in horizontal wind speeds. As shown in Figure 65, there is a large spread in horizontal wind speed.

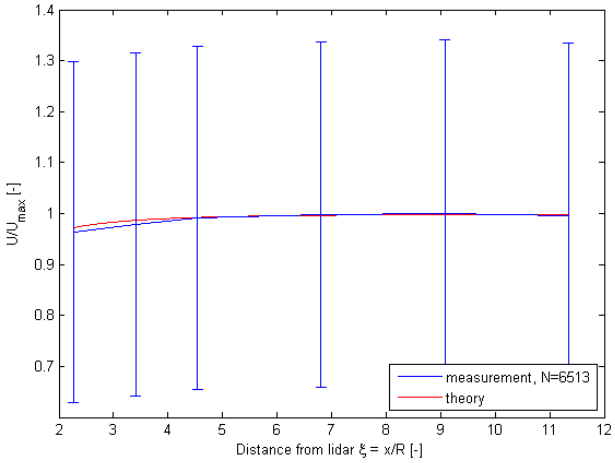

Figure 112: Blockage as measured by lidar including standard deviation as error bars

To illustrate this, Figure 113 is plotted. This graph shows normalized wind speed histograms at various distances from the lidar, but with the wind speed below rated, i.e. 12 m/s. These histograms were normalized by dividing the

wind speeds by 12 m/s since this is the upper limit of the range. The plot shows that there is indeed a large spread in wind velocity, but the trend of Figure 111 can also be seen: the histograms are stretched to the right further from the lidar. In other words, lower velocities occur more closer to the turbine and higher velocities occur more further from the turbine.

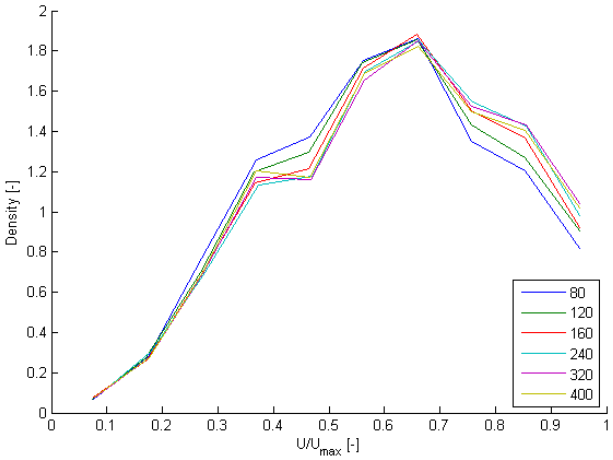

Figure 113: Histograms wind speed at various distances from the lidar, normalized to 12 m/s.

Aside from discussing the validity of this test, it can also be made more similar to that of Medici et al.. They namely conducted the experiment in a wind tunnel, i.e. where the wind speed is controlled. To achieve a similar experiment, only data is included for which the wind speed at 400m was between certain values. For instance, Figure 114 shows what the blockage effect looks like for speeds between 9 and 10 m/s 400m in front of the turbine. The standard deviations have shrunk significantly but the plot also deviates more from the theory. By filtering for wind speed at 400m, the errorbars at this measurement point can essentially be made as small as desired. For instance, Figure 115 shows the blockage plot for wind speeds at 400 between 6.3 and 6.4 m/s. This plot shows that the uncertainty/spread becomes larger as the wind approaches the turbine. It must be noted that this plot has been normalized at 400m.

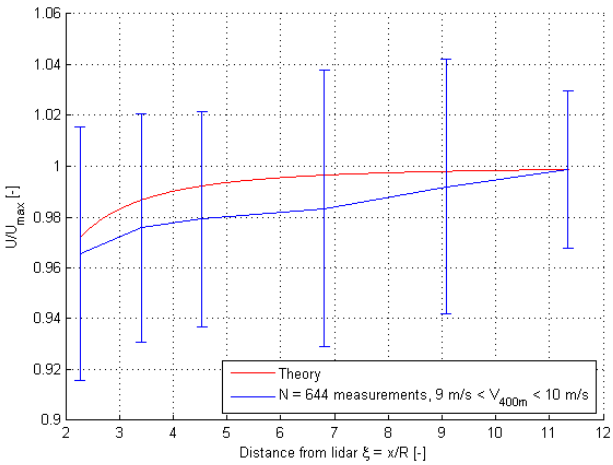

Figure 114: Blockage as measured by lidar for HWS_{400} between 9 and 10 m/s

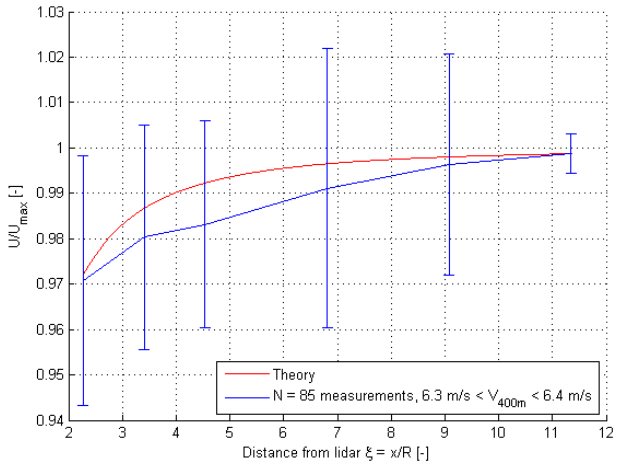

Figure 115: Blockage as measured by lidar for HWS_{400} between 6.3 and 6.4 m/s

The results can be compared to the findings of Wagenaar et al., as shown in Figure 116[65]. In this plot the red line represents northern wind and blue southwestern wind. It shows that the blockage effect can be seen, but there there is some upspeeding for southwestern wind, which are hypothesized to be caused by the turbine's surroundings[65].

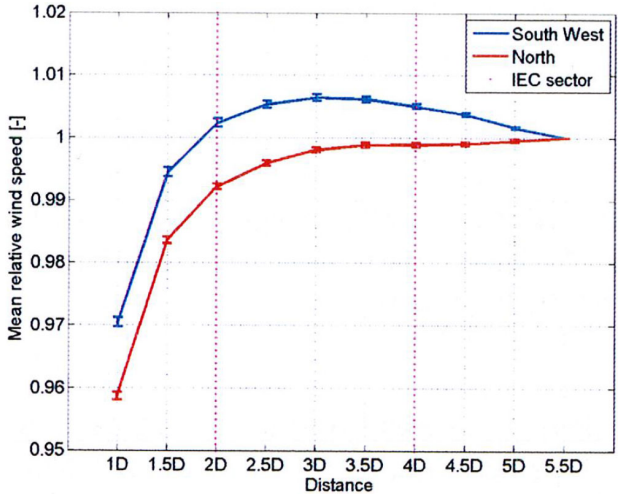

Figure 116: Blockage as measured by Wagenaar et al. using nacelle-based lidar[65]

Another possibility is to compare 10 consecutive 10 minute cases, as shown in Figure 117. These took place on 18 October 2014, with approximately 9 m/s wind from the south. This plot shows that individual 10 minute cases may not perfectly follow the theoretical curve, but seeing the 10 curves together shows that the theoretical trend is certainty present.

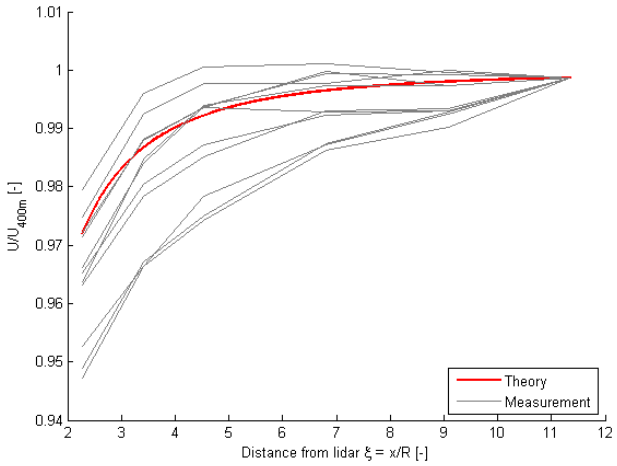

Figure 117: Blockage as measured by lidar in 10 consecutive 10 minute cases

It is also possible to examine the blockage effect at wind speeds above rated. In this case one would not expect the measurements to follow the theoretical curve. Results vary, but a typical plot is shown in Figure 118, illustrating that the reduction in wind speed in front of the turbine is indeed no longer significant.

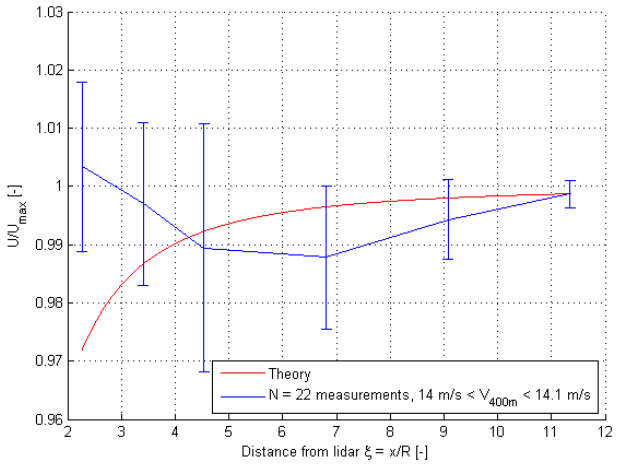

Figure 118: Blockage as measured by lidar for HWS_{400} between 14.0 and 14.1 m/s

However, in all analyses related to blockage, the measurement geometry as shown in Figure 119 should be kept in mind. Considering the conservation of mass as shown in Equation 19 with constant density leads to the conclusion that the streamtube will be narrow for high wind speeds (i.e. upwind) and wide for low wind speeds (i.e. downwind), as illustrated in Figure 110.

$$\rho_1 V_1 A_1 = \rho_2 V_2 A_2 = \rho_3 V_3 A_3 \tag{19}$$

Although it is unknown what the flow upstream of a turbine looks like in detail, the measurements at 240m, 320m and 400m possibly take place outside the streamtube, hence might not be representative for blockage research. For the purpose of investigating blockage, a beam in the middle would be ideal, where the outer beams are used to determine the flow direction, and the middle beam for the flow velocity. On the other hand, the theory suggests that at 400m

(almost 6D), the flow velocity is very close to free stream velocity, meaning that the velocity inside and outside the streamtube is almost the same.

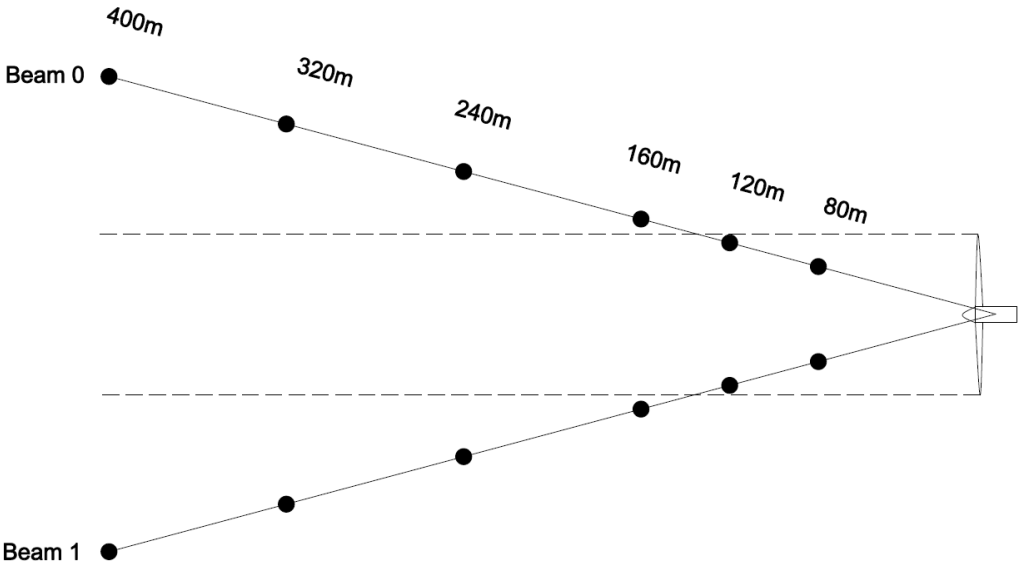

Figure 119: Beam geometry of the Wind Iris at Slufterdam[2]

Combining the findings on the blockage effect with the measurement geometry in Figure 119 should allow for a recommendation on the ideal measurement distance for power curve verification. Figure 119 suggests that at 160m (i.e. 2.3D) the measurement points are further apart than the rotor diameter, hence also outside the streamtube. Therefore this distance could already be representative of free stream. However, Figure 111 shows that the average wind speed at this distance is 99% of the wind speed at 320m. Figure 111 also illustrates that the mean wind speeds at 240m, 320m and 400m points differ by less than 0.5%, hence are representative of free stream wind. However, assuming frozen turbulence, a gust at 400m will take 80 seconds to reach the rotor at a wind speed of 5 m/s, illustrating that the measurement should be neither too close nor too far away from the rotor plane. The ideal measurement distance will therefore probably lie between 160m (2.3D) and 240m (3.4D) in front of the turbine, which is in accordance with the IEC standard, which recommends a meteorological mast at 2.5D[26].

19.3 CONCLUSIONS

As discussed in Chapter 15, the Wind Iris is able to measure average wind speed in front of the turbine accurately, making it an ideal instrument for investigating the blockage effect. The results are very close to the expectations from theory. The trends are different above rated wind speed, which is also in line with expectations. The upspeeding effect as found by Wagenaar et al.[65] were not found, hence supporting their hypothesis that it is caused by local effects.

When using the Wind Iris for power curve verification, the ideal measurement distance will most probably be between 2.3D and 3.4D in front of the turbine. At this location, the measured wind speed is representative of free stream, a finding which is in accordance with the IEC standard[26].

20 FINANCIAL CASE STUDY (RESEARCH OBJECTIVE V)

The fifth and final research objective is to *determine under what conditions a nacelle-based lidar is financially feasible.* By examining the costs and benefits of implementation, a recommendation can be made whether the application of nacelle-based lidar is financially interesting to Vattenfall as operator.

20.1 METHOD

A very specific scenario is assumed and used for all calculations. As such, the number of assumptions is minimized and the calculations can be carried out with more certainty. At the end of this chapter, the sensitivity of this choice is discussed. This will be followed by how this case study can be made more generic so it can be applied to other wind parks or several wind parks.

The scenario used in the case study is that all nine turbines of Slufterdam West are analyzed and adjusted for yaw misalignment. By applying the Wind Iris for two months on each turbine, the average yaw misalignment is determined, which can be adjusted in the yaw controller. As such, just one Wind Iris is required which is applied to all turbines sequentially. The reduction of yaw misalignment is assumed to improve the power curve of the turbines, resulting in greater income during the remainder of the wind park's operational period. Since the wind park was built in 2003, this means that the turbines can operate with the improved power curves until the park's decommissioning in 2023. This also assumes that all turbines have a small yaw misalignment which only needs to be corrected once (i.e. the yaw misalignment does not return). An alternative case study involves permanently replacing the wind vane with a Wind Iris as input for the yaw controller. Another alternative is to use the Wind Iris for feed-forward control of the turbine. However, these scenarios are not examined in this case study.

In the coming sections of this chapter, the costs and benefits of implementation are discussed. The chapter is concluded with a recommendation based on the results.

20.2 COSTS

The first costs to Vattenfall are the *Purchase costs* of the Wind Iris. It is assumed that the instrument is bought for €150 000, as opposed to rented, and that Vattenfall has the capital available for procurement. These costs are written off over the course of five years. The missed income from interest on this capital is not taken directly into account. Instead, when evaluating the outcome of the analysis the return on investment is compared to a potential interest rate.

Most of the other costs involved in the case study are due to manhours. These are estimated and an internal hourly fee of 50 €/hour is assumed.

For instance, installation, as discussed in Chapter 11, takes approximately 20 manhours (four technicians for five hours). During installation and decommissioning the turbine is not operational, and so these costs are also taken into account. This is calculated from the average power production during an entire year (621kW) and the five hours of downtime of the turbine. Decommissioning of the Wind Iris also takes approximately 20 manhours with a downtime of the turbine of five hours.

The campaign length per turbine is assumed to be two months. Wagenaar et al. have developed a method which allows the average yaw misalignment to be determined in less than seven days[65], but for this case study a more conservative estimate is used. The campaign length of two months mean that in the first year of the case study, six turbines are affected, and in the second year, the last three are addressed.

A separate cost item is included for *Operation and Maintenance (O&M)*. For instance, a site visit might be necessary because the power cable becomes unplugged (as occurred during campaign II). These costs are estimated at eight manhours per month during the period in which the Wind Iris is operational. Costs for the support system (data transfer via GSM and FTP) are included in the resulting cost item.

Data analysis is assumed to be taken care of by someone in Vattenfall's Wind Resource team, taking an equivalent of one month FTE, i.e. 160 manhours. Implementation of the wind vane calibration (constant offset in yaw controller) can be done remotely and is included in the cost item *Data analysis*. Note that all manual work (data analysis, O&M, installation and decommissioning) involves a learning curve, where it will take longer for inexperienced employees. In the costs estimates of this case study it is assumed that the employees have some experience with the work.

Taxes are included in each cost item and so there is no separate cost item for taxes. Moreover, there are a couple of risks involved. For instance, the installation of the Wind Iris requires holes to be drilled in the nacelle, which might start leaking during or after the campaign. There is also the risk of lightning strike on the Wind Iris. However, these risks are not given individual cost items, but instead the other cost items are taken more conservative. For instance, the installation and decommissioning of the Wind Iris can be executed during low wind and/or combined with other O&M work on the turbine, illustrating that this cost item is an overestimation. A pie chart of all costs included in this case study is shown in Figure 120.

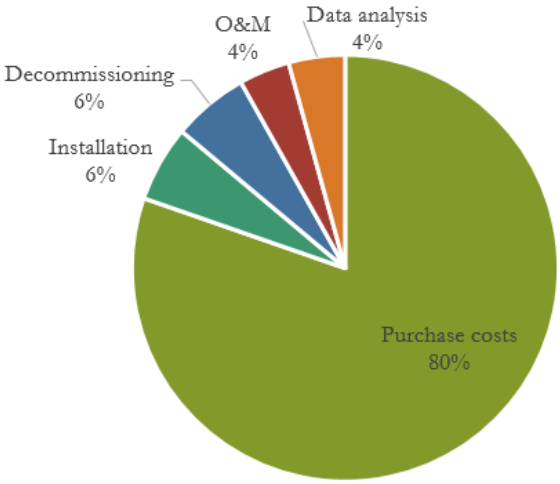

Figure 120: Pie chart of costs

20.3 BENEFITS

There are a couple of financial benefits to this case study, but just one is quantified. For instance, less yaw misalignment will probably lead to less wear and tear, but this is rather difficult to quantify. Similarly, the wind park will be more valuable after the campaign, since it has a higher annual energy production and more is known about the park (wind climate and yaw misalignment). This benefit is also neglected in this case study. The only gain that is quantified is how much more power the nine turbines can produce over the remaining nine years of the wind park's operating life.

To determine how the altered yaw controllers result in greater income, two power curves are used, as well as the wind distribution as determined in Chapter 6. A *PV improvement factor* is introduced which multiplies the power curve below rated power with a constant factor. By combining the wind distribution (through Weibull parameters $A = 9.5\text{m/s}$ and $k = 2.05$) with the old and improved power curve, it is possible to determine how much one turbine will produce more after changing the yaw controller. The turbine's availability is also taken into account, based on the figure in 2014 of 93%. To validate the calculation, the projected AEP (5437 MWh) is compared to the actual AEP of turbine 9 in 2013 and 2014: 4848 MWh and 5163 MWh respectively, revealing the number is plausible. However, it becomes clear that the *PV improvement factor* is a very strong driver in this case study. And Section 18.7 has already shown that it is very difficult to quantify how yaw misalignment affects the power curve.

The next step is to calculate how much extra income is generated from every extra kWh of electricity. Information within the organization has shown this to be approximately €0.06 per kWh.

20.4 RESULTS

To evaluate the outcome of the case study, the Return on Investment (ROI) is used. But to properly compare the case study to leaving the capital in a bank account (or other investment), the exponential nature of interest is taken into account. Under interest factor R (e.g. if interest is 2.4%, R = 1.024), the investment capital C will have grown to B after nine years, as shown in Equation 20.

$$B = C * R^9 \tag{20}$$

This can be rewritten to compute R

$$R = \left(\frac{B}{C}\right)^{\frac{1}{9}} \tag{21}$$

A similar process takes place in the case study. A total costs C is invested, which after nine years has grown to capital B (the total benefits). This means that Equation 21 can be used to compute the equivalent annual interest factor, i.e. the interest factor that would have yielded the same profit. By subtracting one and expressing it as a percentage, the Return on Investment (ROI) is found. Note that this represents the average annual return on investment.

All costs and benefits are shown in a spread sheet of the case study in Figure 121. In this figure, the input parameters as discussed in Section 20.2 and Section 20.3 are entered at the top left. These are used to compute the costs and benefits in each year of the case study. Finally, the numbers are added up and the Return on Investment is calculated according to Equation 21. Note that in this sheet, a *PV improvement factor* of 2% is assumed, yielding a ROI of 5.9%. If the *PV improvement factor* of 2% would have little uncertainty, the implementation of the scenario is recommended, since no banks currently offer 5.9% interest. However, as discussed in Section 18.7, determining the effect of yaw misalignment on the power curve is not straight forward.

Moreover, if a *PV improvement factor* of 1% is used in the case study, the Return on Investment is -1.9%, i.e. money is lost. The break even point is found for a *PV improvement factor* of 1.2%. In other words, if the power curves (below rated power) of all turbines can be improved by 1.2%, the investment costs are returned to Vattenfall through increased power production. If it would be possible to have a *PV improvement factor* of 5%, the ROI is 17.3%. It must be noted that the ROI represents an annual return, but as shown in Figure 121, the capital is invested in the first five years, followed by four years of profit. Only if the *PV improvement factor* is more than 8.6% the case is profitable from the first year on.

In conclusion, the sequential implementation of the Wind Iris is not recommended for Slufterdam West. The analysis from Section 18.7 did not indicate that the power curve of turbine 9 can be improved significantly. Also in literature there is no evidence that indicates that currently operational wind turbines

can benefit from recalibration of the yaw controller. Instead, power curve analysis is recommended if there are signs that an operational turbine might be underperforming. Such a sign could be that a turbine produces significantly less than the best turbine in the park, or that the turbine produces less than anticipated in the park's business case. Such a power curve analysis could be carried out with a Wind Iris or a met mast. The advantage of using a Wind Iris for a power curve analysis is that it also allows for the yaw misalignment to be examined.

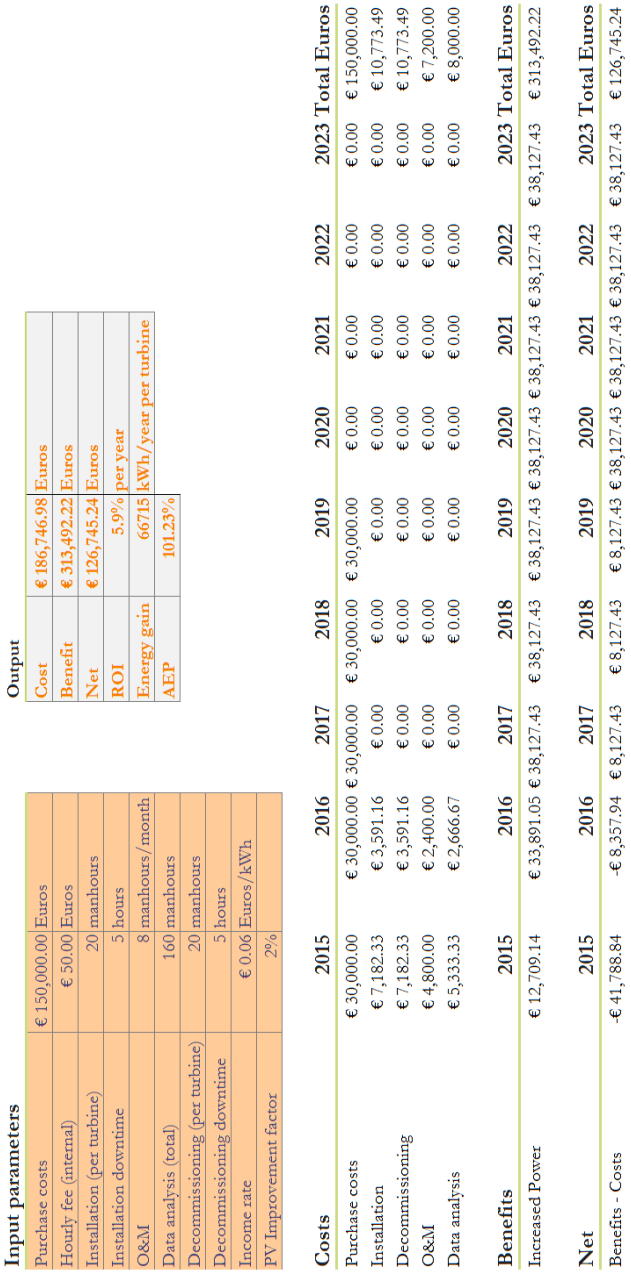

Input parameters

Purchase costs	€ 150,000.00	Euros
Hourly fee (internal)	€ 50.00	Euros
Installation (per turbine)	20	manhours
Installation downtime	5	hours
O&M	8	manhours / month
Data analysis (total)	160	manhours
Decommissioning (per turbine)	20	manhours
Decommissioning downtime	5	hours
Income rate	€ 0.06	Euros / kWh
PV Improvement factor	2%	

Output

Cost	€ 186,746.98	Euros
Benefit	€ 313,492.22	Euros
Net	€ 126,745.24	Euros
ROI	5.9%	per year
Energy gain	66715	kWh/year per turbine
AEP	101.23%	

Costs	**2015**	**2016**	**2017**	**2018**	**2019**	**2020**	**2021**	**2022**	**2023**	**Total Euros**
Purchase costs	€ 30,000.00	€ 30,000.00	€ 30,000.00	€ 30,000.00	€ 30,000.00	€ 0.00	€ 0.00	€ 0.00	€ 0.00	€ 150,000.00
Installation	€ 7,182.33	€ 3,591.16	€ 0.00	€ 0.00	€ 0.00	€ 0.00	€ 0.00	€ 0.00	€ 0.00	€ 10,773.49
Decommissioning	€ 7,182.33	€ 3,591.16	€ 0.00	€ 0.00	€ 0.00	€ 0.00	€ 0.00	€ 0.00	€ 0.00	€ 10,773.49
O&M	€ 4,800.00	€ 2,400.00	€ 0.00	€ 0.00	€ 0.00	€ 0.00	€ 0.00	€ 0.00	€ 0.00	€ 7,200.00
Data analysis	€ 5,333.33	€ 2,666.67	€ 0.00	€ 0.00	€ 0.00	€ 0.00	€ 0.00	€ 0.00	€ 0.00	€ 8,000.00
Benefits	**2015**	**2016**	**2017**	**2018**	**2019**	**2020**	**2021**	**2022**	**2023**	**Total Euros**
Increased Power	€ 12,709.14	€ 33,891.05	€ 38,127.43	€ 38,127.43	€ 38,127.43	€ 38,127.43	€ 38,127.43	€ 38,127.43	€ 38,127.43	€ 313,492.22
Net	**2015**	**2016**	**2017**	**2018**	**2019**	**2020**	**2021**	**2022**	**2023**	**Total Euros**
Benefits - Costs	-€ 41,788.84	-€ 8,357.94	€ 8,127.43	€ 8,127.43	€ 8,127.43	€ 38,127.43	€ 38,127.43	€ 38,127.43	€ 38,127.43	€ 126,745.24

Figure 121: Spreadsheet of the case study

Although implementation of the Wind Iris for reduction of yaw misalignment is currently not recommended, it might become interesting in the future, for instance, if more is known about the impact of yaw misalignment on the

power curve. In that case it will be worthwhile to know the strongest drivers in the financial analysis. These turned out to be the *PV improvement factor*, the purchase costs, income rate (i.e. price per kWh) and wind park properties. To illustrate the last variable, if Slufterdam West would consist of 3MW turbines instead of 1.5MW turbines, the benefit side nearly doubles, making the scenario much more interesting from a financial viewpoint. Moreover, the profitability also depends on the subsidy scheme of the wind park since this strongly impacts the income rate. Also, if the site has relatively low wind, the turbines are mostly operational below rated wind speed. This means that gains in this region of the power curve have a stronger effect on the AEP. Moreover, if the wind park is relatively new, there are more years available before decommissioning of the park, hence there is more time for the improved power curve to make an impact. However, this does assume that the yaw misalignment needs to be corrected just once, an assumption that certainly requires more research. Another option is to examine the scenario of applying the Wind Iris to several wind parks, reducing the impact of purchase costs significantly. Renting the Wind Iris is also an option, but more so in the case of a single wind turbine or small wind park. For a large company like Vattenfall, purchasing the Wind Iris is probably more profitable since it will be likely to be implemented for many wind turbines.

21 INCLINOMETER

The Wind Iris is equipped with an inclinometer, which measures the lidar's tilt and roll angles. The definitions and conventions regarding tilt, yaw and roll angles are shown in Figure 122, where the arrows indicate a positive angle.

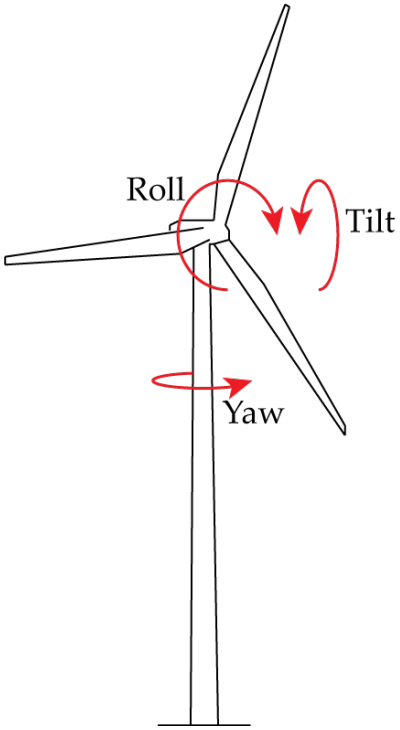

Figure 122: Definition and convention of angle measurements with the Wind Iris

These measurements can be processed in several ways, providing insight in the behavior of the wind turbine and functioning of the lidar. This is interesting information for Vattenfall as operator, since they are interested in all applications of nacelle-based lidar. The inclinometer's original purpose is to measure the tower bend at varying wind speeds. This allows for the lidar's tilt to be adjusted accurately, to make sure it measures at the correct height, as explained in Chapter 11.

However, the tilt and roll measurements can also be applied for different purposes. For instance, it can give insight in the measurement uncertainty of the lidar, since a bending tower means that the lidar is measuring at varying heights (hence varying wind speeds). Moreover, the lidar measures line-of-sight velocity, which would be equal to the wind velocity assuming purely horizontal wind and horizontal lidar measurement. The validity of these assumptions could be tested with the inclinometer measurements.

21.1 DETERMINING THE EIGENFREQUENCY OF THE TOWER

The first alternative application to be examined is an FFT (Fast Fourier Transform) of the signals[76], to give insight in the motion of the lidar, hence of the tower. To achieve this, one hour of 1Hz data is analyzed (on 8 Oct 2014), where Figure 123 is an estimation of the spectral density of the tilt signal and Figure 124 of the roll signal. A clear difference between the two signals is evident, probably caused by the fore-aft damping effect of the rotor. The first eigenfrequency of the tower becomes clear from Figure 124 and is 0.406 Hz. In both plots, there is quite a lot of noise, in the order of 0.2-1.0.

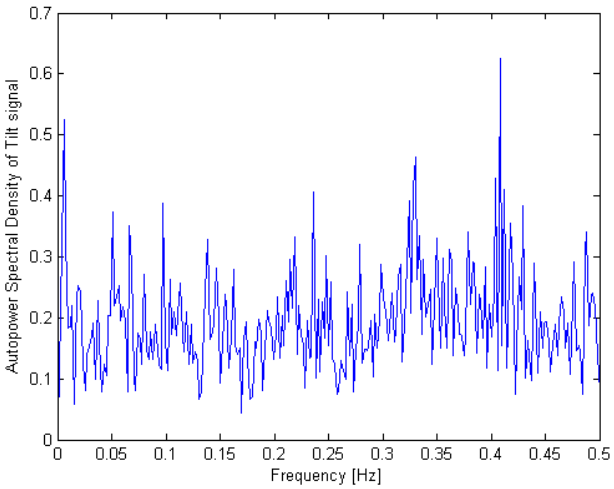

Figure 123: Spectral Density estimation of 1Hz tilt signal (Welch's method, $m = 512$)

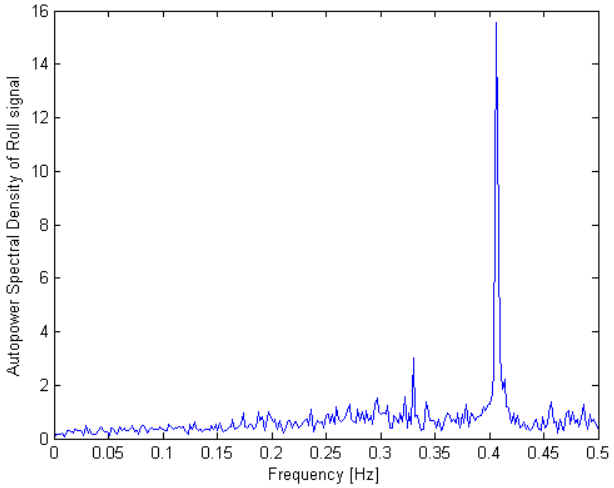

Figure 124: Spectral Density estimation of 1Hz roll signal (Welch's method, $m = 512$)

Figure 78 already illustrated that the rotor speed varies between approximately 12 and 20 RPM, and one could expect 1P, 2P and 3P to show up in plots. During the specific one hour time window of this analysis (i.e. on the afternoon of 8 Oct 2014), the rotor speed was around 20RPM, and so the 1P, 2P and 3P are respectively 0.33, 0.66 and 1 Hz. The 2P and 3P exceed the Nyquist frequency, but the 1P (0.33Hz) is visible as a peak in both Figure 123 and Figure 124.

This procedure can be repeated, but now applying it to one hour of data where the turbine is in error. This way, the fore-aft damping effect should not be visible in the plots. A suitable time window was found between 18 September and 23 September: during these days the Wind Iris was already installed, but the turbine was in error. The evening of the 21st was selected because it was relatively windy. Once again one hour of 1Hz data is processed and the results are shown in Figure 125 and Figure 126. The two plots are now very similar and indicate a first tower eigenfrequency of 0.402Hz and 0.408Hz respectively. As expected, the plots also contain a lot less noise, since the turbine is not operating.

To gain more trust in the FFT analysis, a test signal is created, sampled at one Hz and analyzed. This procedure is discussed in Appendix C.

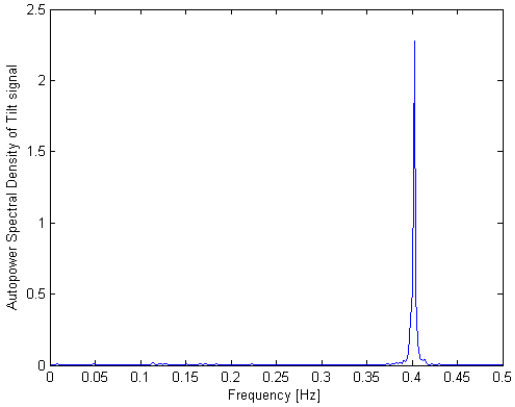

Figure 125: Spectral Density estimation of 1Hz tilt signal while the turbine is not operating (Welch's method, $m = 512$)

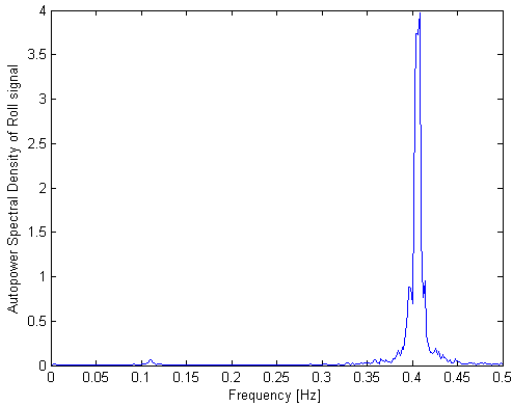

Figure 126: Spectral Density estimation of 1Hz roll signal while the turbine is not operating (Welch's method, $m = 512$)

21.2 TILT AND MEASURING HEIGHT

The roll and tilt measurements also allow for some assumptions to be checked. As mentioned in Chapter 11, the tower bend was not correctly taken into account in the lidar installation. This is shown in Figure 127, which illustrates that the lidar is pointing up, rather than down. The resulting mean tilt is 0.4° degrees, whereas the desired tilt is calculated in Equation 22 to be −0.3°. This calculation is based on a lidar height of 0.93m above hub height (since it is mounted on top of the nacelle), and the lidar is recommended to measure at hub height 2.5D in front of the turbine[72].

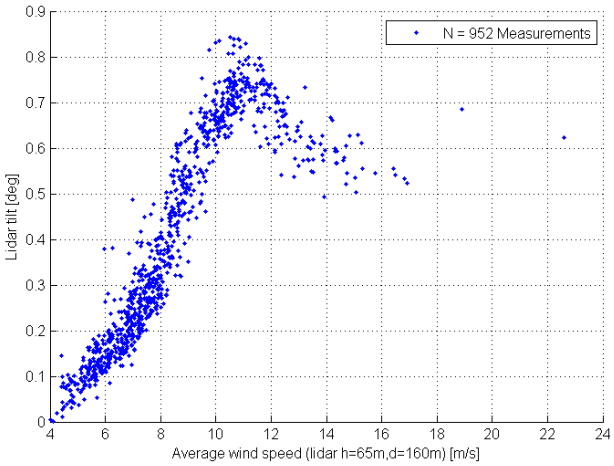

Figure 127: Lidar tilt as a function of horizontal wind speed

$$\theta = \tan^{-1}\left(\frac{-0.93}{2.5 * 70.5}\right) = -0.3° \tag{22}$$

The average measuring height at 2.5D is calculated in Equation 23 to be 2.2m above hub height. Going back to Chapter 6 and more specifically Figure 11, the effect of this tilt can be estimated. Figure 11 namely shows that Weibull parameter "A" is more or less linear with altitude between 55m and 90m, and the average wind is related to the Weibull parameters through Equation 4.

$$h = 0.93 + 2.5 * 70.5 * \tan(0.4°) = 2.2m \tag{23}$$

The slope of Figure 11 is approximately $(90-60)/(9.9-9.4) = 60s$. Hence the 2.2m that the lidar is measuring too high at translates to a change in parameter "A" of $2.2/60 = 0.04$ m/s, i.e. from $A = 9.50$ to 9.54 m/s. When measuring power curves with nacelle-based lidar, such as in Chapter 17, it means that the recorded wind speed is higher, causing a power curve which is slightly worse than the power curve as measured at hub height. The yaw misalignment is not expected to be significantly different when measuring 2.2m higher than hub height. The blockage effect is likely to be recorded slightly stronger than present in reality. However, ideally one would measure with 0° tilt in case of investigating blockage, instead of −0.3°.

Part III

CONCLUSIONS AND RECOMMENDATIONS

22 CONCLUSIONS

22.1 VALIDATION

The research has shown that the Wind Iris is able to measure 10 minute average wind speed accurately. This conclusion is based on a comparison between the lidar and a sodar on site through a time series and scatter plot. This finding is in accordance with literature[4][34][37][43][51][57][65][66][67].

However, there is no consensus in literature when it comes to measuring turbulence intensity with lidar[12][35][40][65]. A comparison between the sodar and lidar is made in this thesis, but did not provide conclusive results.

Regarding yaw misalignment, two methods of measuring it are used in this thesis, as discussed in Section 15.4 and Appendix D. However, the two methods showed little correlation, and so a simulation was executed to gain more insight in these measurements. The lack of correlation is plausible if the measurement uncertainty is higher than the spread in yaw misalignment, meaning that the Wind Iris possibly has a higher uncertainty than anticipated (in the order of 4° instead of 0.5°).

22.2 MEASUREMENT CAMPAIGNS

Data from two measurement campaigns is used, as discussed in Part i (Campaign I) and Part ii (Campaign II). Part i had a focus on resource analysis, where Part ii focused more on the research objectives as set out in Chapter 3. The former involved one year of turbine (scada) and sodar data, whereas the latter spanned approximately 3 months with turbine (scada), sodar and nacelle-based lidar data. In both campaigns KNMI data from the nearby station Hoek van Holland was used for validation. In practice, Part i also served the purpose of getting a feel of the data and wind park, forming a foundation and context for Part ii. Site data such as the wind speed distribution and wind shear which were determined in the first campaign were also used during analysis of the data from the second campaign.

22.3 ADDRESSING THE RESEARCH OBJECTIVES

The research objectives of this thesis as listed in Chapter 3 are addressed in detail in Part ii, but their main conclusions are summarized below:

Chapter 13 addressed the first research objective, concluding that no major issues arose during installation of the Wind Iris, although two minor points are formulated as recommendations in Chapter 23. Access to the data and data processing are relatively straightforward by means of Oldbaum's FTP server and Matlab. There is plenty of literature available for comparison and verification. 90% of the 10 minute data points was applicable, so availability of the lidar was good.

The Wind Iris is a suitable instrument for measuring the power curve, as discussed in Chapter 17, considering it is able to accurately measure mean wind speed in front of the turbine. The power curve of the turbine under research was found to be in accordance with the power curve in the (expired) contract.

Chapter 18 addressed the third research objective, showing that an average yaw misalignment of 1.5° was found for the turbine under investigation. The Wind Iris is a suitable instrument for determining yaw misalignment, although the direction measurements are probably less accurate than anticipated. Moreover, in the wind regime where it is relevant to the power curve, yaw misalignment was found to have no clear relationship with rotor speed and wind speed. Regarding the impact of yaw misalignment on the power curve, a $cosine$, $cosine^2$ or $cosine^3$ relation was expected, but a slight improvement of the power curve was found for small positive yaw misalignment. However, due to uncertainty in the measurements and analyses, no definitive conclusions could be drawn.

The Wind Iris has shown to be a good tool for investigating the blockage effect, as discussed in Chapter 19, and the results are in accordance with theory. When using the Wind Iris for power curve verification, the ideal measurement distance is between 2.3D and 3.4D, a finding which is equivalent to the IEC recommendation of 2.5D.

Chapter 20 addressed the implementation of the Wind Iris from a financial point of view. For the purpose of improving the power curves through reduction of yaw misalignment, the sequential implementation of the Wind Iris is not recommended. The strongest drivers in the case study are the power curve improvement and purchase costs of the Wind Iris, but analysis showed that the power curve improvements are not evident. If a trustworthy research group uses an on-off approach to investigate the effect of intentional yaw misalignment on the power curve, the case study gets more certainty and becomes more attractive. Until then, there is too much uncertainty to recommend implementation for the purpose of improving the power curve.

23

RECOMMENDATIONS

Numerous recommendations can be formulated following this thesis. For instance, a 2.5D measurement point can be added in the beginning of the campaign if the Wind Iris is used for power curve verification. Moreover, although the tilt of the lidar can be adjusted during the campaign, it is recommended that the tower bend is taken into account according to Section 21.2.

A more general recommendation is to add pressure and temperature measurements to the campaign, for the purpose of correcting for density. Although they would be useful, the Wind Iris does not have such sensors. Moreover, the power of the turbine could be measured independently and according to the IEC standard.

Since there is no clarity on the Wind Iris' ability to measure turbulence, it is recommended that turbulence intensity measurements from lidars are used with care. Moreover, the Wind Iris itself does not measure the orientation of the nacelle, even though this is an important parameter in numerous analyses. Although in case of Slufterdam the nacelle direction was logged by the wind turbine, it was not calibrated. Therefore it is recommended that this is kept in mind when considering research with nacelle-based lidar. More specifically, the nacelle direction could be measured independently at the start of the campaign and implemented as an offset during data processing.

To gain more insight in the impact of yaw misalignment on the power curve, the methods discussed in Section 18.7 can be applied to different turbines or existing data sets. The experiment can be extended by examining 1 minute data instead of 10 minute data, since this might be a more appropriate time scale. Moreover, an experiment is recommended where an operational turbine is put under an intentional yaw misalignment, which is regularly varied. For instance, changing the misalignment every hour to a new value between -25 and 25 degrees.

An experiment to measure the wind direction accuracy of the Wind Iris is also recommended, as discussed at the end of Section 15.4. This could be done by mounting it on a static mast instead of a wind turbine, and comparing the perceived wind direction to wind vane measurements on a nearby mast. The opening angle can be varied to evaluate the hypothesis that a larger opening angle allows for a more accurate wind direction measurement at the cost of this measurement being less local. Another option is to test two or more systems side-by-side to evaluate the accuracy of wind direction measurements.

Finally, Vattenfall is recommended to stay critical towards new developments and claims regarding power curve improvement. Internal evaluation of new

technology allows for such claims to be tested independently. Moreover, the sodar in Part ii proved to be a valuable addition to the measurement campaign. It allowed for validation and added measurement of temperature, pressure, wind direction, sheer and veer, which were more useful than anticipated. Therefore it is recommended that in future campaigns additional instruments are considered, since they can add significant value to the campaign. Finally, expansion of the R&D work could be considered, since this can help stay competitive in the long term.

BIBLIOGRAPHY

[1] Ali M. Abdelsalam, K. Boopathi, S. Gomathinayagam, S.S. Hari Krishnan Kumar, and Velraj Ramalingam. Experimental and numerical studies on the wake behavior of a horizontal axis wind turbine. *Journal of Wind Engineering and Industrial Aerodynamics*, 128(0):54 – 65, 2014. ISSN 0167-6105. doi: http://dx.doi.org/10.1016/j.jweia.2014.03.002. URL http://www.sciencedirect.com/science/article/pii/S0167610514000464.

[2] Erik Baker. Performance Assessment for Slufterdam - Monthly Report - December 2014. Technical report, Oldbaum Services, 2015.

[3] W.A.A.M. Bierbooms. Matlab function: (least square) estimation of Weibull parameters k and a from histogram f(V), 1999.

[4] F. Bingöl, J. Mann, and D. Foussekis. LiDAR error estimation with WAsP engineering. *IOP Conference Series: Earth and Environmental Science*, 1(1): 012058, 2008. URL http://stacks.iop.org/1755-1315/1/i=1/a=012058.

[5] Ferhat Bingol, Jakob Mann, and Gunner C. Larsen. Light detection and ranging measurements of wake dynamics part I: one-dimensional scanning. *Wind Energy*, 13(1):51–61, 2010. ISSN 1099-1824. doi: 10.1002/we.352. URL http://dx.doi.org/10.1002/we.352.

[6] Bosch & Van Rijn. Windstats Kaart, 2014. URL http://windstats.boschenvanrijn.nl/.

[7] E. Bossanyi. Un-freezing the turbulence: application to LiDAR-assisted wind turbine control. *Renewable Power Generation, IET*, 7(4):321–329, July 2013. ISSN 1752-1416. doi: 10.1049/iet-rpg.2012.0260.

[8] E. Bossanyi, B. Savini, M. Iribas, M. Hau, B. Fischer, D. Schlipf, T. van Engelen, M. Rossetti, and C. E. Carcangiu. Advanced controller research for multi-MW wind turbines in the UPWIND project. *Wind Energy*, 15(1): 119–145, 2012. ISSN 1099-1824. doi: 10.1002/we.523. URL http://dx.doi.org/10.1002/we.523.

[9] C.L. Bottasso, P. Pizzinelli, C.E.D. Riboldi, and L. Tasca. LiDAR-enabled model predictive control of wind turbines with real-time capabilities. *Renewable Energy*, 71(0):442 – 452, 2014. ISSN 0960-1481. doi: http://dx.doi.org/10.1016/j.renene.2014.05.041. URL http://www.sciencedirect.com/science/article/pii/S0960148114003024.

[10] Jean-Pierre Cariou, Laurent Sauvage, Ludovic Thobois, Guillaume Gorju, Mehdi Machta, Guillaume Lea, and Marie Duboué. Long range scanning pulsed coherent lidar for real time wind monitoring in the planetary boundary layer. *16th CLRC*, 2011.

[11] Ward W Carson, Hans-Erik Andersen, Stephen E Reutebuch, and Robert J McGaughey. LiDAR applications in forestry: An overview. In *Annual Aspres Conference Proceedings*, 2004.

[12] P. J. M. Clive. Compensation of vector and volume averaging bias in lidar wind speed measurements. *IOP Conference Series: Earth and Environmental Science*, 1(1):012036, 2008. URL http://stacks.iop.org/1755-1315/1/i=1/a=012036.

[13] P. J. M. Clive. The wind farm whisperers. In *All Energy Aberdeen*, May 2014. URL http://www.sgurrenergy.com/wp-content/uploads/2012/08/the-wind-farm-whisperers-Peter-Clive.pdf.

[14] S. Feeney, A. Derrick, A. Oram, I. Campbell, G. Hutton, G. Powles, C. Slinger, M. Harris, J. Medley, and E. Burin des Roziers. Project Cyclops: The Way Forward in Power Curve Measurements? In *EWEA*, March 2014. URL http://proceedings.ewea.org/annual2014/conference/posters/PO_083_EWEApresentation2014.pdf.

[15] P. A. Fleming, A. K. Scholbrock, A. Jehu, S. Davoust, E. Osler, A. D. Wright, and A. Clifton. Field-test results using a nacelle-mounted lidar for improving wind turbine power capture by reducing yaw misalignment. *Journal of Physics: Conference Series*, 524(1):012002, 2014. URL http://stacks.iop.org/1742-6596/524/i=1/a=012002.

[16] Rod Frehlich. 19 - Coherent Doppler lidar measurements of winds. In Anna Consortini, editor, *Trends in Optics*, Lasers and Optical Engineering, pages 351 – 370. Academic Press, San Diego, 1996. ISBN 978-0-12-186030-1. doi: http://dx.doi.org/10.1016/B978-012186030-1/50021-7. URL http://www.sciencedirect.com/science/article/pii/B9780121860301500217.

[17] *Technical Description and Specifications - Wind Turbine Generator System GE Wind Energy 1.5s*. GE Wind Energy GmbH, 2002.

[18] G.G. Goyer and R. Watson. The Laser and its Application to Meteorology. *Bulletin of the American Meteorological Society*, 44(9):564–575, 1963.

[19] R. Groenland and H. Geurts. Neerslagradar KNMI: Uitgebreide toelichting, October 2009. URL http://www.knmi.nl/cms/content/69720/uitgebreide_toelichting_bij_knmi_neerslagradar.

[20] M. Harris, M. Hand, and A. Wright. Lidar for Turbine Control. Technical report, National Renewable Energy Laboratory (NREL), 2006. URL http://www.nrel.gov/docs/fy06osti/39154.pdf.

[21] Emil Hedevang. Wind turbine power curves incorporating turbulence intensity. *Wind Energy*, 17(2):173–195, 2014. ISSN 1099-1824. doi: 10.1002/we.1566. URL http://dx.doi.org/10.1002/we.1566.

[22] Carine Homan. December 2014: Vrij zacht, gemiddelde hoeveelheid neerslag en uren zonneschijn, 2015. URL http://www.knmi.nl/klimatologie/maand_en_seizoensoverzichten/maand/dec14.html. Koninklijk Nederlands Meteorologisch Instituut.

[23] S. Honhoff. Power curves - the effect of environmental conditions. In *Scientific proceedings (GE Wind AWEA Wind Speed and Energy Workshop, Portland, Oregon USA)*, 2007.

[24] Raymond Hunter, Troels Friis Pedersen, Penny Dunbabin, Ioannis Antoniou, Sten Tronæs Frandsen, Helmut Klug, Axel Albers, and Wai Kong Lee. *European wind turbine testing procedure developments. Task 1: Measurement method to verify wind turbine performance characteristics*. Print: Danka Services International A/S, 2001.

[25] Suzan Ilcan and Lynne Phillips. Developmentalities and Calculative Practices: The Millennium Development Goals. *Antipode*, 42(4):844–874, 2010. ISSN 1467-8330. doi: 10.1111/j.1467-8330.2010.00778.x. URL http://dx.doi.org/10.1111/j.1467-8330.2010.00778.x.

[26] International Electrotechnical Commission. IEC 61400-12-1. Wind turbines - Part 12-1: Power performance measurements of electricity producing wind turbines, 2005.

[27] C. J. Karlsson, F. A. Olsson, D. Letalick, and M. Harris. All-Fiber Multifunction Continuous-Wave Coherent Laser Radar at 1.55 num for Range, Speed, Vibration, and Wind Measurements. *Applied optics*, 2000. doi: 10.1364/AO.39.003716.

[28] D.K. Killinger. 10 - Lidar (light detection and ranging). In Matthieu Baudelet, editor, *Laser Spectroscopy for Sensing*, pages 292 – 312. Woodhead Publishing, 2014. ISBN 978-0-85709-273-1. doi: http://dx.doi.org/10.1533/9780857098733.2.292. URL http://www.sciencedirect.com/science/article/pii/B9780857092731500106.

[29] Knud A. Kragh and Morten H. Hansen. Potential of power gain with improved yaw alignment. *Wind Energy*, 2014. ISSN 1099-1824. doi: 10.1002/we.1739. URL http://dx.doi.org/10.1002/we.1739.

[30] Knud A. Kragh, Paul A. Fleming, and Andrew K. Scholbrock. Increased Power Capture by Rotor Speed-Dependent Yaw Control of Wind Turbines. *Journal of Solar Energy Engineering*, 2013. URL http://dx.doi.org/10.1115/1.4023971.

[31] Knud A. Kragh, Morten H. Hansen, and Lars C. Henriksen. Sensor comparison study for load alleviating wind turbine pitch control. *Wind Energy*, 2013. ISSN 1099-1824. doi: 10.1002/we.1675. URL http://dx.doi.org/10.1002/we.1675.

[32] Knud A. Kragh, Morten H. Hansen, and Torben Mikkelsen. Precision and shortcomings of yaw error estimation using spinner-based light detection and ranging. *Wind Energy*, 16(3):353–366, 2013. ISSN 1099-1824. doi: 10.1002/we.1492. URL http://dx.doi.org/10.1002/we.1492.

[33] Knud Abildgaard Kragh and Paul A. Fleming. *Rotor Speed Dependent Yaw Control of Wind Turbines Based on Empirical Data*. American Institute of Aeronautics & Astronautics, 2012.

[34] R. Krishnamurthy, A. Choukulkar, R. Calhoun, J. Fine, A. Oliver, and K.S. Barr. Coherent Doppler lidar for wind farm characterization. *Wind Energy*, 16(2):189–206, 2013. ISSN 1099-1824. doi: 10.1002/we.539. URL http://dx.doi.org/10.1002/we.539.

[35] R. Krishnamurthy, M. Boquet, and M. Machta. Turbulence Intensity measurements for a variety of Doppler Lidar instruments. In *EWEA*, March 2014. URL http://proceedings.ewea.org/annual2014/conference/posters/PO_080_EWEApresentation2014.pdf.

[36] Idaho National Laboratory. Manufacturer's power curve table, 2014. URL www.inl.gov/wind/software/powercurves/pc_ge_wind_m_s.xls.

[37] Steven Lang and Eamon McKeogh. LIDAR and SODAR Measurements of Wind Speed and Direction in Upland Terrain for Wind Energy Purposes. *Remote Sensing*, 3(9):1871–1901, 2011. ISSN 2072-4292. doi: 10.3390/rs3091871. URL http://www.mdpi.com/2072-4292/3/9/1871.

[38] Henrik Lund. Renewable energy strategies for sustainable development. *Energy*, 32(6):912 – 919, 2007. ISSN 0360-5442. doi: http://dx.doi.org/10.1016/j.energy.2006.10.017. URL http://www.sciencedirect.com/science/article/pii/S036054420600301X. Third Dubrovnik Conference on Sustainable Development of Energy, Water and Environment Systems.

[39] T. H. Maiman. Stimulated Optical Radiation in ruby. *Nature*, 187(4736):493–494, 1960.

[40] Jakob Mann, Ameya Sathe, Julia Gottschall, and Mike Courtney. Lidar turbulence measurements for wind energy. In Martin Oberlack, Joachim Peinke, Alessandro Talamelli, Luciano Castillo, and Michael Hölling, editors, *Progress in Turbulence and Wind Energy IV*, volume 141 of *Springer Proceedings in Physics*, pages 263–270. Springer Berlin Heidelberg, 2012. ISBN 978-3-642-28967-5. doi: 10.1007/978-3-642-28968-2_57. URL http://dx.doi.org/10.1007/978-3-642-28968-2_57.

[41] D. Medici, S. Ivanell, J.-Å. Dahlberg, and P. H. Alfredsson. The upstream flow of a wind turbine: blockage effect. *Wind Energy*, 14(5):691–697, 2011. ISSN 1099-1824. doi: 10.1002/we.451. URL http://dx.doi.org/10.1002/we.451.

[42] Tony Mercer. Lidar-assisted control of wind turbines. Technical report, GL Garrad Hassan, 2012. URL http://www.gl-garradhassan.com/assets/downloads/Turbine_mounted_LiDAR_to_improve_wind_turbine_control.pdf.

[43] T. Mikkelsen, K. Hansen, N. Angelou, M. Sjoholm, M. Harris, P. Hadley, R. Scullion, G. Ellis, and G. Vives. LIDAR wind speed measurements from a rotating spinner. In *EWEC*, 2010. URL http://orbit.dtu.dk/fedora/objects/orbit:58157/datastreams/file_4553836/content.

[44] T. Mikkelsen, N. Angelou, K. Hansen, M. Sjoholm, M. Harris, C. Slinger, P. Hadley, R. Scullion, G. Ellis, and G. Vives. A spinner integrated wind

lidar for enhanced wind turbine control. *Wind Energy*, 16(4):625–643, 2013. doi: 10.1002/we.1564. URL http://dx.doi.org/10.1002/we.1564.

[45] Charles A. Northend. Lidar, a laser radar for meteorological studies. *Naturwissenschaften*, 54(4):77–80, 1967. ISSN 0028-1042. doi: 10.1007/BF00608760. URL http://dx.doi.org/10.1007/BF00608760.

[46] Christian Pavese. Wind energy literature survey no. 33. *Wind Energy*, 17 (11):1789–1795, 2014. ISSN 1099-1824. doi: 10.1002/we.1782. URL http://dx.doi.org/10.1002/we.1782.

[47] T. F. Pedersen. On wind turbine power performance measurements at inclined airflow. *Wind Energy*, 7(3):163–176, 2004. ISSN 1099-1824. doi: 10.1002/we.112. URL http://dx.doi.org/10.1002/we.112.

[48] T.F. Pedersen, N.N. Sørensen, L. Vita, P. Enevoldsen, and Risø National Lab. for Sustainable Energy. Wind Energy Div Technical Univ. of Denmark. *Optimization of Wind Turbine Operation by Use of Spinner Anemometer*. Contract ENS-33032-0040. Risø National Laboratory for Sustainable Energy, 2008. ISBN 9788755036987. URL http://books.google.nl/books?id=2XUmmQEACAAJ.

[49] Troels Friis Pedersen, Søren Gjerding, Peter Ingham, Peder Enevoldsen, Jesper Kjær Hansen, and Henrik Kanstrup Jørgensen Vestas. Wind turbine power performance verification in complex terrain and wind farms. Technical report, Risø National Laboratory, Roskilde, April 2002.

[50] W.G. Rees. *Physical Principles of Remote Sensing*. Topics in remote sensing. Cambridge University Press, 2001. ISBN 9780521660341. URL http://books.google.nl/books?id=dWgdQwAACAAJ.

[51] Michael E. Rhodes and Julie K. Lundquist. The Effect of Wind-Turbine Wakes on Summertime US Midwest Atmospheric Wind Profiles as Observed with Ground-Based Doppler Lidar. *Boundary-Layer Meteorology*, 149 (1):85–103, 2013. ISSN 0006-8314. doi: 10.1007/s10546-013-9834-x. URL http://dx.doi.org/10.1007/s10546-013-9834-x.

[52] J. Sanz Rodrigo, F. Borbón Guillén, P. Gómez Arranz, M.S. Courtney, R. Wagner, and E. Dupont. Multi-site testing and evaluation of remote sensing instruments for wind energy applications. *Renewable Energy*, 53(0): 200 – 210, 2013. ISSN 0960-1481. doi: http://dx.doi.org/10.1016/j.renene.2012.11.020. URL http://www.sciencedirect.com/science/article/pii/S0960148112007379.

[53] David Schlipf, Dominik Johannes Schlipf, and Martin Kühn. Nonlinear model predictive control of wind turbines using LIDAR. *Wind Energy*, 16 (7):1107–1129, 2013. ISSN 1099-1824. doi: 10.1002/we.1533. URL http://dx.doi.org/10.1002/we.1533.

[54] Andrew Scholbrock, Paul Fleming, Alan Wright, Chris Slinger, John Medley, and Michael Harris. Field Test Results from Lidar Measured Yaw Control for Improved Power Capture with the NREL Controls Advanced Re-

search Turbine. *33rd Wind Energy Symposium*, 2015. URL http://dx.doi.org/10.2514/6.2015-1209.

[55] Eric Simley, Lucy Y. Pao, Rod Frehlich, Bonnie Jonkman, and Neil Kelley. Analysis of light detection and ranging wind speed measurements for wind turbine control. *Wind Energy*, 17(3):413–433, 2014. ISSN 1099-1824. doi: 10.1002/we.1584. URL http://dx.doi.org/10.1002/we.1584.

[56] Rob Sluijter. Seizoensoverzicht Herfst 2014 (september, oktober, november): Uitzonderlijk zacht, droog en zeer zonnig - Herfst op een na zachtste in ruim 300 jaar, 2014. URL http://www.knmi.nl/klimatologie/maand_en_seizoensoverzichten/seizoen/her14.html. Koninklijk Nederlands Meteorologisch Instituut.

[57] David A. Smith, Michael Harris, Adrian S. Coffey, Torben Mikkelsen, Hans E. Jørgensen, Jakob Mann, and Régis Danielian. Wind lidar evaluation at the Danish wind test site in Høvsøre. *Wind Energy*, 9(1–2):87–93, 2006. doi: 10.1002/we.193. URL http://dx.doi.org/10.1002/we.193.

[58] Lasse Svenningsen. Power Curve Air Density Correction And Other Power Curve Options In WindPRO. Technical report, EMD International A/S, 2010. URL www.emd.dk/files/windpro/WindPRO_Power_Curve_Options.pdf.

[59] Lasse Svenningsen. Proposal of an Improved Power Curve Correction. In *EWEC*, 2010. URL http://proceedings.ewea.org/ewec2010/posters/PO.310_EWEC2010presentation.pdf.

[60] Pierre-Julien Trombe, Pierre Pinson, Claire Vincent, Thomas Bøvith, Nicolaos A. Cutululis, Caroline Draxl, Gregor Giebel, Andrea N. Hahmann, Niels E. Jensen, Bo P. Jensen, Nina F. Le, Henrik Madsen, Lisbeth B. Pedersen, and Anders Sommer. Weather radars – the new eyes for offshore wind farms? *Wind Energy*, 2013. ISSN 1099-1824. doi: 10.1002/we.1659. URL http://dx.doi.org/10.1002/we.1659.

[61] Juan-José Trujillo, Ferhat Bingöl, Gunner C. Larsen, Jakob Mann, and Martin Kühn. Light detection and ranging measurements of wake dynamics. Part II: two-dimensional scanning. *Wind Energy*, 14(1):61–75, 2011. ISSN 1099-1824. doi: 10.1002/we.402. URL http://dx.doi.org/10.1002/we.402.

[62] L. van den Brink and E. Holtslag. Shorter LiDAR campaigns without seasonal bias. In *EWEA*, March 2014. URL http://proceedings.ewea.org/annual2014/conference/posters/PO_116_EWEApresentation2014.pdf.

[63] N. W. Verwaal, G. J. Veen, and J. W. Wingerden. Predictive control of an experimental wind turbine using preview wind speed measurements. *Wind Energy*, 2014. doi: 10.1002/we.1702. URL http://onlinelibrary.wiley.com/doi/10.1002/we.1702/abstract.

[64] H.M. Villanueva Lopez. The Illusion of Power Curves. Master's thesis, Delft University of Technology - Department of Wind Energy, 2014.

[65] J.W. Wagenaar, S. Davoust, A. Medawar, G. Coubard-Millet, and K. Boorsma. Turbine performance validation; the application of nacelle LiDAR. In *EWEA*, March 2014. URL http://proceedings.ewea.org/annual2014/conference/posters/PO_081_EWEApresentation2014.pdf.

[66] R. Wagner, M. Courtney, J. Gottschall, and P. Lindelöw-Marsden. Accounting for the speed shear in wind turbine power performance measurement. *Wind Energy*, 14(8):993–1004, 2011. ISSN 1099-1824. doi: 10.1002/we.509. URL http://dx.doi.org/10.1002/we.509.

[67] R. Wagner, T.F. Pedersen, M. Courtney, I. Antoniou, S. Davoust, and R.L. Rivera. Power curve measurement with a nacelle mounted lidar. *Wind Energy*, 2013. doi: 10.1002/we.1643. URL http://dx.doi.org/10.1002/we.1643.

[68] R. Wagner, B. Cañadillas, A. Clifton, S. Feeney, N. Nygaard, M. Poodt, C. St Martin, E. Tüxen, and J. W. Wagenaar. Rotor equivalent wind speed for power curve measurement - comparative exercise for IEA Wind Annex 32. *Journal of Physics: Conference Series*, 524(1):012108, 2014. URL http://stacks.iop.org/1742-6596/524/i=1/a=012108.

[69] R. Wagner, M. Courtney, T.F. Pedersen, S. Davoust, and R.L. Rivera. What makes a nacelle mounted lidar a suitable tool for power performance measurement? In *EWEA*, March 2014. URL http://proceedings.ewea.org/annual2014/conference/posters/PO_179_EWEApresentation2014.pdf.

[70] Rozenn Wagner and Samuel Davoust. Nacelle lidar for power curve measurement - Avendøre campaign. Technical report, DTU Wind Energy, 2013.

[71] Rozenn Wagner, Ioannis Antoniou, Søren M. Pedersen, Michael S. Courtney, and Hans E. Jørgensen. The influence of the wind speed profile on wind turbine performance measurements. *Wind Energy*, 12(4):348–362, 2009. ISSN 1099-1824. doi: 10.1002/we.297. URL http://dx.doi.org/10.1002/we.297.

[72] Rozenn Wagner, Rebeca L. Rivera, Ioannis Antoniou, Samuel Davoust, Troels Friis Pedersen, Michael Courtney, and Babak Diznabi. *Procedure for wind turbine power performance measurement with a two-beam nacelle lidar*. DTU Wind Energy E. DTU Wind Energy, 2013.

[73] Na Wang, K.E. Johnson, and A.D. Wright. FX-RLS-Based Feedforward Control for LIDAR-Enabled Wind Turbine Load Mitigation. *Control Systems Technology, IEEE Transactions on*, 20(5):1212–1222, Sept 2012. ISSN 1063-6536. doi: 10.1109/TCST.2011.2163515.

[74] Na Wang, K.E. Johnson, and A.D. Wright. Comparison of Strategies for Enhancing Energy Capture and Reducing Loads Using LIDAR and Feedforward Control. *Control Systems Technology, IEEE Transactions on*, 21(4):1129–1142, July 2013. ISSN 1063-6536. doi: 10.1109/TCST.2013.2258670.

[75] J. Wieringa and P. J. Rijkoort. *Windklimaat van Nederland*. Staatsuitgeverij 's-Gravenhage, 1983. ISBN 90 12 044669.

[76] A.H.J. Winnemuller. Matlab function: FFT analysis of a data sequence using the Welch method of power spectrum estimation., 1995.

Part IV

APPENDICES

A

DERIVATION OF LIDAR RELATIONS

Chapter 10 discusses how lidar works, and how the wind direction and velocity can be computed with a two beam lidar. However, Equation 6 is not derived in the original paper[72]. Therefore a derivation is made in this thesis with help of Figure 128. In this figure, the line-of-sight velocity vectors are rearranged, making trigonometric relations clearer.

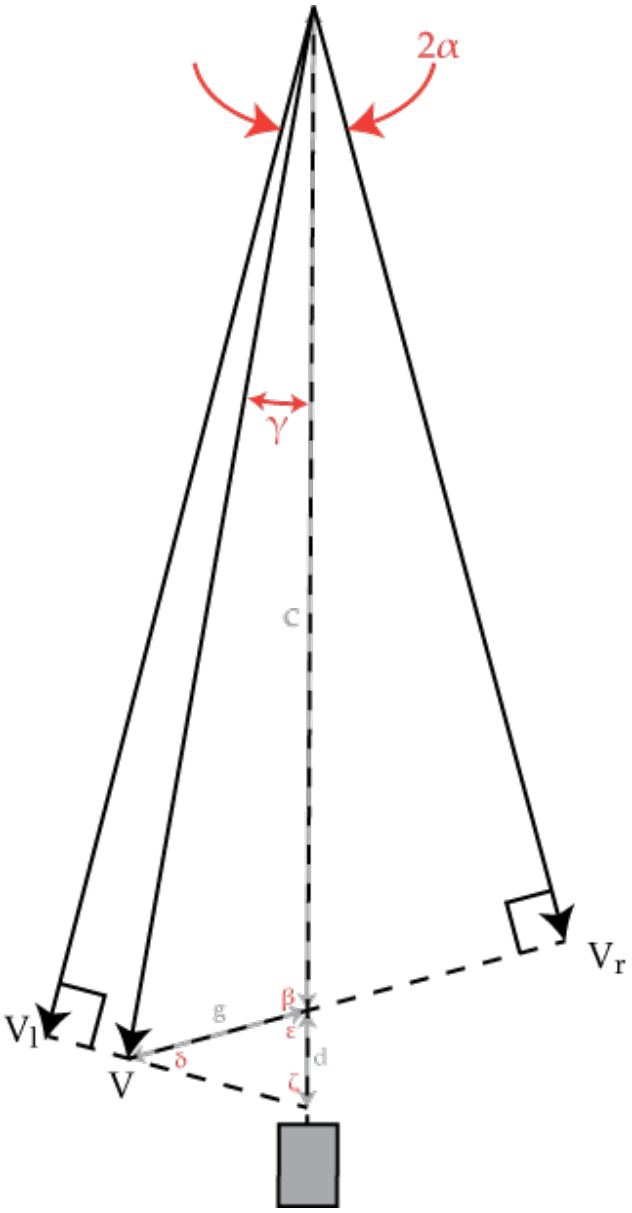

Figure 128: Derivation of wind direction (γ) and wind velocity (V) for a two beam lidar

From Figure 128, Equation 24 can be derived:

$$
\begin{aligned}
c &= \frac{V_r}{\cos\alpha} \\
c + d &= \frac{V_l}{\cos\alpha} \\
\rightarrow d &= \frac{V_l - V_r}{\cos\alpha} \\
g &= \frac{d\sin\zeta}{\sin\delta} = \frac{V_l - V_r}{\cos\alpha}\frac{\sin\zeta}{\sin\delta}
\end{aligned}
\tag{24}
$$

where

$$
\begin{aligned}
\zeta &= 180° - 90° - \alpha = 90° - \alpha \\
\delta &= 180° - 2(90° - \alpha) = 2\alpha \\
\rightarrow g &= \frac{V_l - V_r}{\cos\alpha}\frac{\cos\alpha}{\sin 2\alpha} = \frac{V_l - V_r}{\sin 2\alpha}
\end{aligned}
\tag{25}
$$

Applying the cosine rule to find V^2:

$$
V^2 = g^2 + c^2 - 2gc\cos\beta \tag{26}
$$

where

$$
\begin{aligned}
\beta &= 180° - \epsilon = 180° - (90° - \alpha) = 90° + \alpha \\
\rightarrow V^2 &= \left(\frac{V_l - V_r}{\sin 2\alpha}\right)^2 + \left(\frac{V_r}{\cos\alpha}\right)^2 + 2\left(\frac{V_l - V_r}{\sin 2\alpha}\right)\left(\frac{V_r}{\cos\alpha}\right)\sin\alpha \\
V^2 &= \left(\frac{V_l - V_r}{\sin 2\alpha}\right)^2 + \left(\frac{V_r}{\cos\alpha}\right)^2 + 2\left(\frac{V_l - V_r}{\sin 2\alpha}\right)V_r\tan\alpha
\end{aligned}
\tag{27}
$$

Using the identity $\sin 2\alpha = 2\sin\alpha\cos\alpha$ this can be written as:

$$
V^2 = \left(\frac{V_l - V_r}{\sin 2\alpha}\right)^2 + \left(\frac{V_r}{\cos\alpha}\right)^2 + 2\left(\frac{V_l - V_r}{2\sin\alpha\cos\alpha}\right)V_r\frac{\sin\alpha}{\cos\alpha} \tag{28}
$$

$$
V^2 = \left(\frac{V_l - V_r}{\sin 2\alpha}\right)^2 + \left(\frac{V_r}{\cos\alpha}\right)^2 + \frac{V_l V_r - V_r^2}{\cos^2\alpha}
$$

$$
V^2 = \left(\frac{V_l - V_r}{\sin 2\alpha}\right)^2 + \frac{V_l V_r}{\cos^2\alpha} \tag{29}
$$

The wind direction can be calculated similarly:

$$
\gamma = \arcsin\left(\frac{g\sin\beta}{V}\right) = \arcsin\left(\frac{V_l - V_r}{\sin 2\alpha}\frac{\sin\beta}{V}\right) \tag{30}
$$

$$
\gamma = \arcsin\left(\frac{V_l - V_r}{\sin 2\alpha}\frac{\cos\alpha}{V}\right)
$$

$$
\gamma = \arcsin\left(\frac{V_l - V_r}{2\sin\alpha\cos\alpha}\frac{\cos\alpha}{V}\right)
$$

$$
\gamma = \arcsin\left(\frac{V_l - V_r}{2V\sin\alpha}\right) \tag{31}
$$

These equations are not the same as Equation 6, but they rewritten as such. First, Equation 29 is rewritten as Equation 32:

$$
\begin{aligned}
V^2 &= \left(\frac{V_l - V_r}{2sin\alpha cos\alpha}\right)^2 + \frac{V_l V_r}{cos^2\alpha} \\
V^2 &= \frac{V_l^2 - 2V_l V_r + V_r^2}{4sin^2\alpha cos^2\alpha} + \frac{V_l V_r}{cos^2\alpha}
\end{aligned}
\tag{32}
$$

using $\frac{1}{cos^2\alpha} = tan^2\alpha + 1$:

$$
\begin{aligned}
V^2 &= \frac{V_l^2 - 2V_l V_r + V_r^2}{4sin^2\alpha}\left(tan^2\alpha + 1\right) + \frac{V_l V_r}{cos^2\alpha} \\
V^2 &= \frac{V_l^2 - 2V_l V_r + V_r^2}{4cos^2\alpha} + \frac{V_l^2 - 2V_l V_r + V_r^2}{4sin^2\alpha} + \frac{V_l V_r}{cos^2\alpha} \\
V^2 &= \frac{V_l^2 + 2V_l V_r + V_r^2}{4cos^2\alpha} + \frac{V_l^2 - 2V_l V_r + V_r^2}{4sin^2\alpha} \\
V^2 &= \frac{(V_l + V_r)^2}{4cos^2\alpha} + \frac{(V_l - V_r)^2}{4sin^2\alpha} \\
V^2 &= \left(\frac{V_l + V_r}{2cos\alpha}\right)^2 + \left(\frac{V_l - V_r}{2sin\alpha}\right)^2 \\
V^2 &= V_x^2 + V_y^2
\end{aligned}
\tag{33}
$$

The parameters V_x and V_y are the wind components parallel and orthogonal to the rotor axis respectively. Hence the wind direction (i.e. yaw misalignment) can be computed according to Equation 34, in accordance with Wagner et al.[67].

$$
\gamma = \arctan\frac{V_y}{V_x} \tag{34}
$$

This can also be verified combining $V_y = \frac{V_l - V_r}{2sin\alpha}$ and Equation 31:

$$
\gamma = \arcsin\frac{V_y}{V} \tag{35}
$$

B

WIND ROSES

Working with wind roses in both Matlab and WindPro, one can run into the following problem: the Matlab function *rose* plots o facing East and plots counterclockwise positive, whereas the convention for wind roses (hence also the results from WindPro) is to plot o facing North and clockwise positive. The different results are shown in Figure 129. Essentially the plots are the same, but flipped along the axis pointed at 45°.

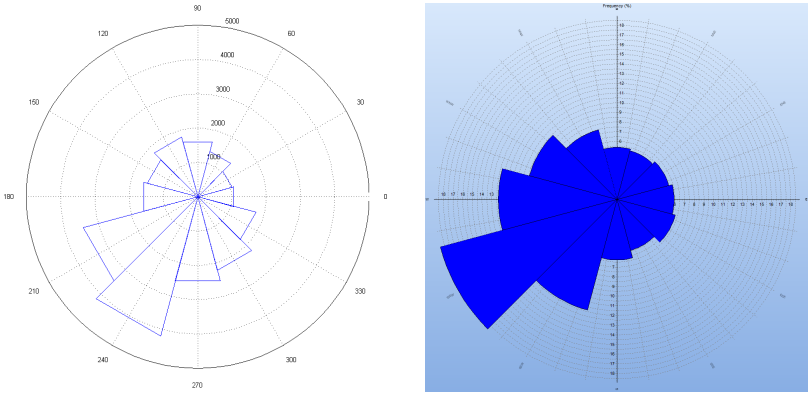

Figure 129: Wind roses plotted with the same data, but using different axes. Left: Matlab, right: WindPro

This problem can be solved in Matlab by adding the line *view(90,-90);* or using the function *fcnwindrose.m* using dtype *'meteo'*. The former is illustrated in the test script below:

```
clc; clear all; close all;
%%

winddirection = [359 1 1 40 45 3 360 25 75 270]; % Test data in degrees
%%
% Rose plot of # incidents
figure()
winddirection = pi*winddirection/180; % convert to radians
nsteps = 12; % 12 bins is the convention
windbins = 0:(2*pi/nsteps):(2*pi-(2*pi/nsteps)); % create windbins,
    convention is 12 bins
rose(winddirection,windbins);
view(90,-90); % normally rose plots 0 on the right and positive
    counterclockwise. But the wind convention is 0 on top and positive
    clockwise
```

C

VERIFICATION OF THE FAST FOURIER TRANSFORM ACCORDING TO WELCH'S METHOD

To gain more trust in the Fast Fourier Transform analysis[76] performed in Chapter 21, a small experiment is conducted to validate the results. More specifically, a signal is created, sampled at 1Hz and analyzed with a FFT.

Figure 130 shows the signal that has been created using Equation 36. The signal has similar frequencies and amplitudes as the tilt and roll signals of Chapter 21. Just like the real tilt and roll signals used in the analysis, the created signal also has a duration of one hour. The frequencies of the test signal are 0.4023Hz, 0.05Hz and 0.24Hz.

$$y = 0.3\sin(2\pi 0.4023t) + 0.3\sin(2\pi 0.05t) + 0.3\sin(2\pi 0.24t) \tag{36}$$

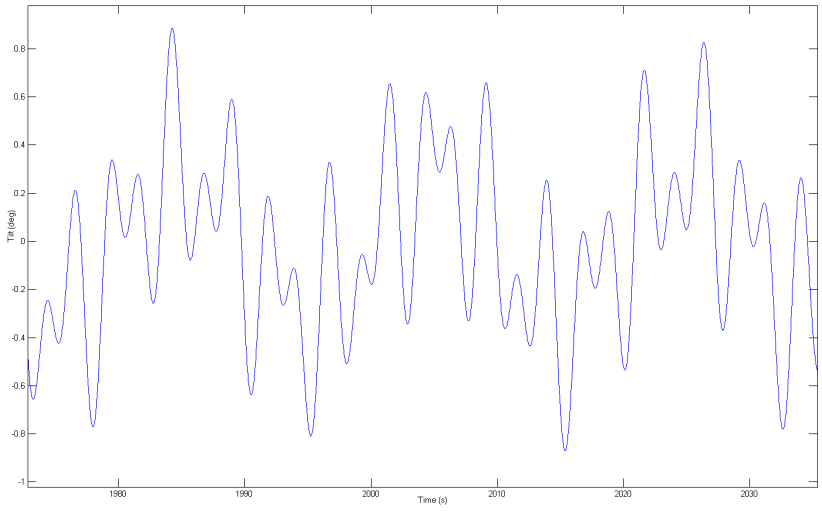

Figure 130: Test tilt signal

The next step is to sample this signal at 1Hz, so it matches the sample rate of the original signal. The result is shown in Figure 131. The result looks random and chaotic and one would not suspect this to be the result of sampling three sinusoids at 1Hz. However, the FFT analysis according to Welch's method clearly shows the three peaks at the right frequencies, as shown in Figure 132. This shows that the analysis in Chapter 21 and that the FFT according to Welch's method are trustworthy.

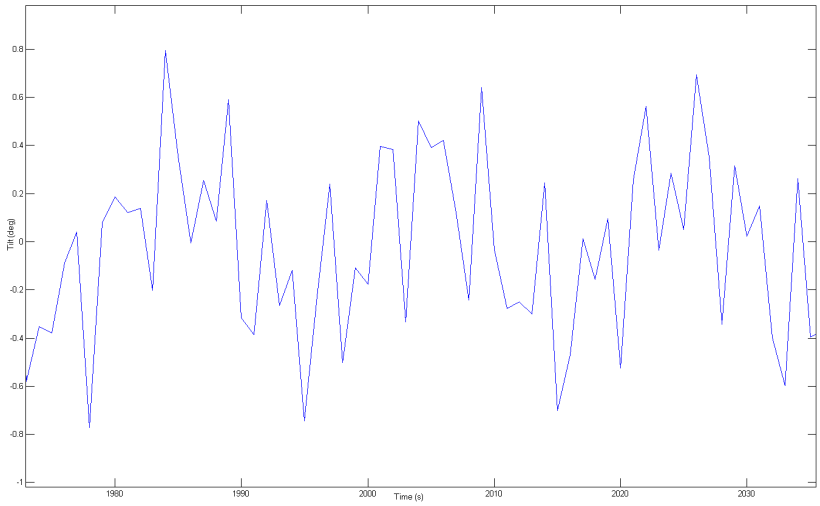

Figure 131: Test tilt signal sampled at 1 Hz

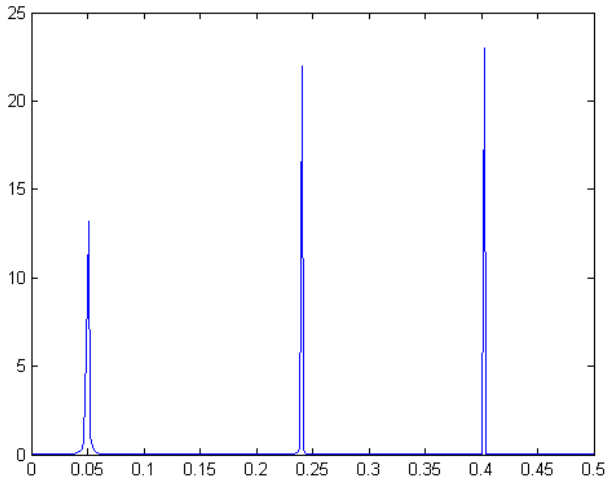

Figure 132: Spectral Density estimation of 1Hz test tilt signal (Welch's method, $m = 512$)

D

SIMULATION OF YAW MISALIGNMENT AND ITS MEASUREMENT WITH LIDAR AND SODAR

Figure 58 in Section 15.4 revealed that there is little correlation between the two methods of measuring yaw misalignment. The first method is a direct measurement of yaw misalignment by means of a nacelle-based lidar. The second method uses wind direction using sodar and nacelle direction measurement. Subtracting the two signals should also result in yaw misalignment, but the two methods show little correlation.

To gain more insight, yaw misalignment and its measurements are simulated in Matlab, to try and reproduce the results from Section 15.4. First, a wind direction signal is created using Matlab's random generator *normrnd*. The nacelle responds to the wind, but has a constant and variable yaw misalignment, *meanyawmisalignment* and *nacellemisalignmentspread* respectively. This yaw misalignment is detected by the nacelle-based lidar (*YMwindiris*), but with a measurement error *windirisaccuracy*. The wind direction is measured by the sodar (*sodardirection*) and the nacelle direction is logged (*nacelledirection*), both in integers, just like the real signals. Subtracting the two also creates a yaw misalignment signal called *YMscadasodar*. The script for this simulation is shown below.

```
simlength = 6000;                % in 10min points
windvariability = 5;             % in degrees
meanyawmisalignment = 2;         % in degrees
nacellemisalignmentspread = 1.5; % in degrees
sodaraccuracy = 5;               % in degrees. Manual says "accuracy < 5
    degrees"
windirisaccuracy = 4;            % in degrees. Manual says 0.5 degrees
offset = -5;                     % nacelle dir - wind dir constant offset

time = 10*linspace(0,simlength,simlength); % in minutes
meanwinddirection = linspace(90,20,simlength);
winddirection = normrnd(meanwinddirection,windvariability);
nacelledirection = normrnd(winddirection+meanyawmisalignment,
    nacellemisalignmentspread);
nacelledirectionlogged = round(nacelledirection)+offset;
sodardirection = round(normrnd(winddirection,sodaraccuracy));
YM = nacelledirection - winddirection;
YMwindiris = normrnd(YM,windirisaccuracy);
YMscadasodar = nacelledirectionlogged-sodardirection;
```

Consequently, similar plots to that of Section 15.4 are created, shown in Figure 133 and Figure 134. By experimenting with the input variables, it is possible to get an idea of the measurement uncertainties and their effect on the results. As can be seen by comparing Figure 58 to Figure 133, the simulation is able to produce very similar results. These results are found for $\sigma_{YM} = 1.5$,

$\sigma_{windiris} = 4$, and $\sigma_{sodar} = 5$. It turns out that the correlation (i.e. slope and R^2 in Figure 133) strongly depends on the actual yaw misalignment spread σ_{YM}. The spread of the cloud in x and y direction depend mostly on the sodar and lidar measurement accuracy, σ_{sodar} and $\sigma_{windiris}$ respectively. The histograms resulting from the simulation are also very similar to those found from the measurements (i.e. Figure 59 and Figure 134).

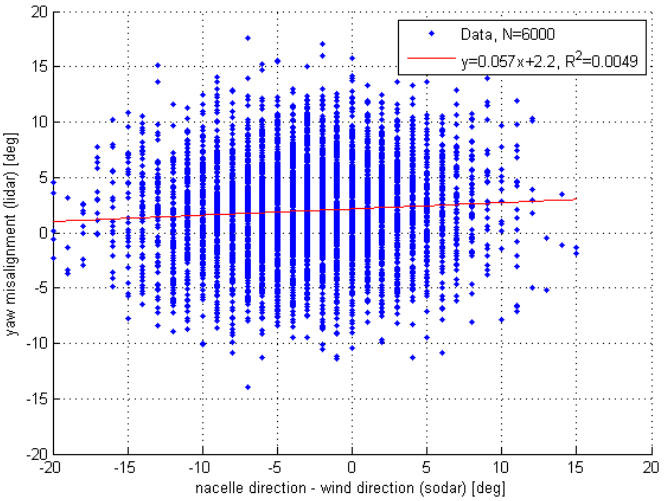

Figure 133: Scatter plot of yaw misalignment (simulation)

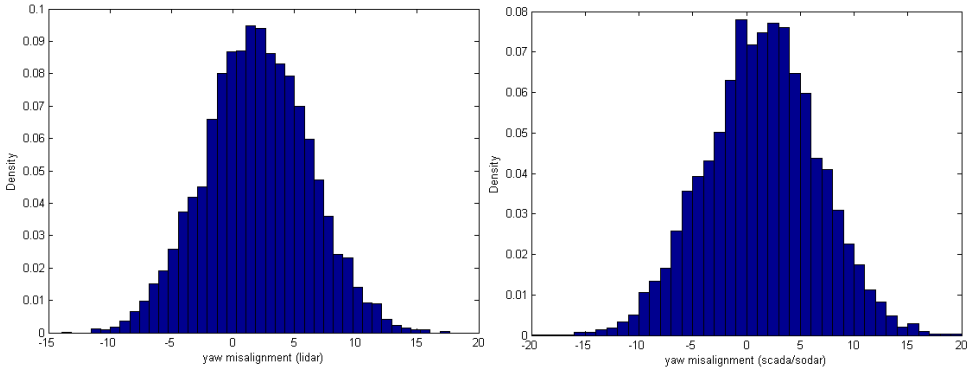

Figure 134: Histograms of yaw misalignment (simulation)

However, now that the directions are simulated, it is possible to plot the actual yaw misalignment histogram, as shown in Figure 135. As expected, there is relatively little spread, since the standard deviation was set to 1.5 degrees ($\sigma_{YM} = 1.5$). Interestingly, the spread as found from the lidar and scada/sodar method is significantly more, and this effect should be taken into account when considering yaw misalignment histograms. Furthermore, the Wind Iris manual lists the accuracy as 0.5 degrees, but in the simulation the standard deviation was set to 4 degrees to achieve a similar scatter plot and histogram. More specifically, with a lower standard deviation in the simulation, the spread of Figure 133 was found to be compressed in y-direction.

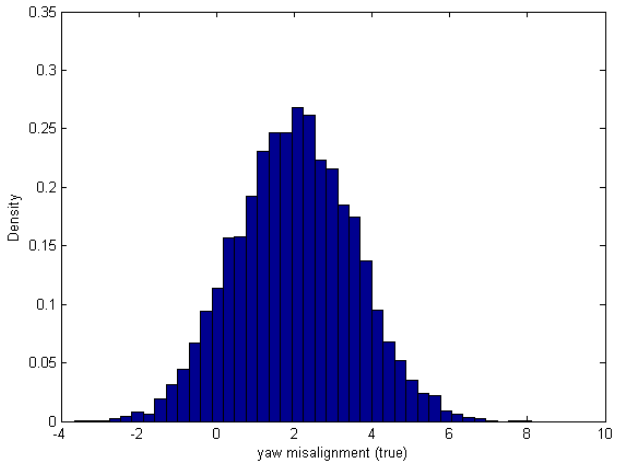

Figure 135: Histogram of actual yaw misalignment (simulation)

To illustrate how the input parameters affect the scatter plot, Figure 136 is included below, where $\sigma_{YM} = 5$, $\sigma_{WindIris} = 0.5$ and $\sigma_{sodar} = 8$. The fit now has a steeper gradient (since σ_{YM} is higher), and the horizontal spread is greater (since σ_{sodar} is higher). The vertical spread seems more or less the same as before, even though $\sigma_{WindIris} = 0.5$, but since there is a slope in the overall trend, the horizontal spread can also be interpreted as vertical spread.

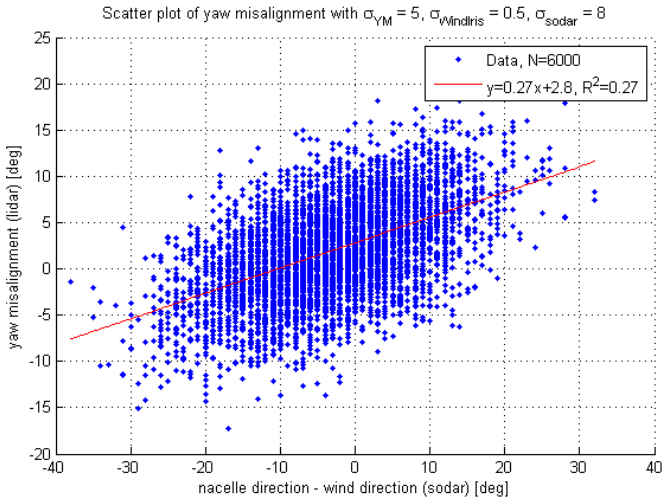

Figure 136: Scatter plot of yaw misalignment (simulation)

To illustrate, Figure 137 has $\sigma_{YM} = 0$, $\sigma_{WindIris} = 0.1$ and $\sigma_{sodar} = 8$. As a result, there is no correlation between x and y (since $\sigma_{YM} = 0$), the vertical spread is very small (since $\sigma_{WindIris} = 0.1$), but the horizontal spread is similar to that in Figure 136.

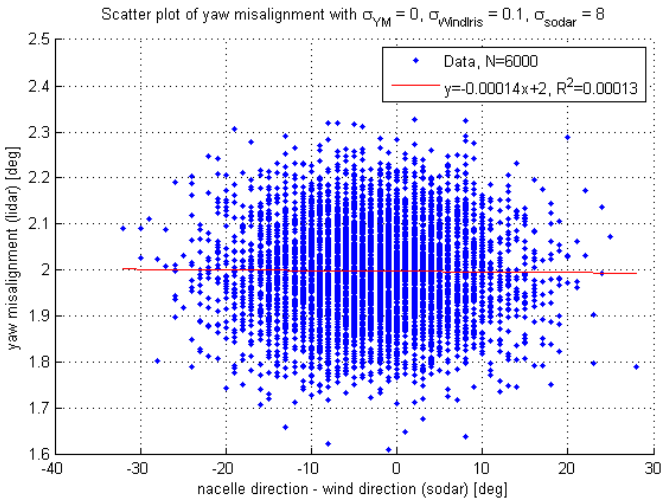

Figure 137: Scatter plot of yaw misalignment (simulation)

An almost ideal case is shown in Figure 138, where $\sigma_{YM} = 2$, $\sigma_{WindIris} = 0.1$ and $\sigma_{sodar} = 0.1$. Now the correlation is clearly visible and the spread around the fit is small, although still larger than one might expect. This is caused by the rounding of the nacelle direction and sodar wind direction. For instance, the wind direction might be 105.5°, which is recorded as 106°, and the nacelle direction could be 105.45°, recorded as 105°. The *scada/sodar* method therefore records a yaw misalignment of 1°, even though in reality it is just 0.05°. This is what causes the relatively large spread in Figure 138, which is no longer present if rounding of the signals is turned off, as shown in Figure 139. With $\sigma_{WindIris} = 0$, $\sigma_{sodar} = 0$ and rounding turned off, all data points form a line, as expected.

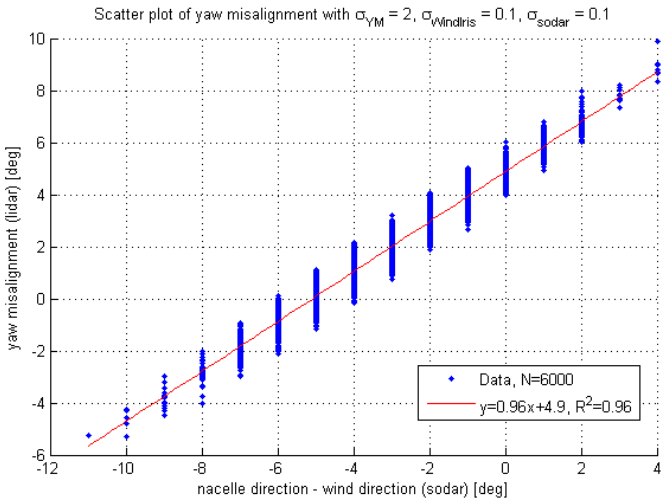

Figure 138: Scatter plot of yaw misalignment (simulation)

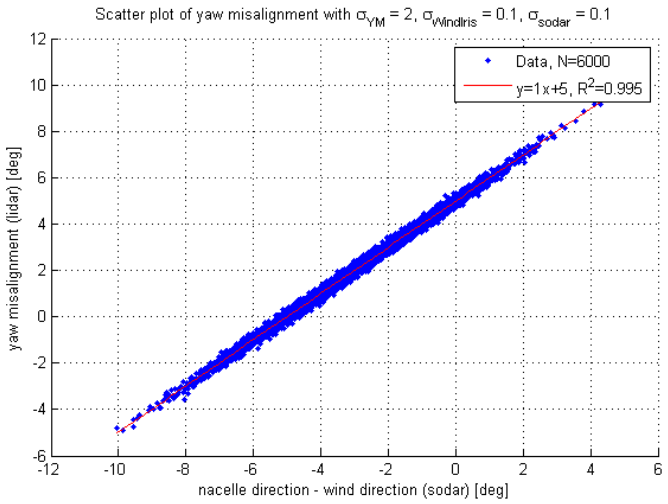

Figure 139: Scatter plot of yaw misalignment (simulation, unrounded signals)

In conclusion, the simulation got closest to the measurements (Figure 58) for $\sigma_{YM} = 1.5$, $\sigma_{WindIris} = 4$ and $\sigma_{sodar} = 5$, as shown in Figure 133. This means that the Wind Iris probably has a larger uncertainty in its direction measurement than anticipated, meaning that the spread in yaw misalignment is overestimated. In other words, the turbine is misaligned less frequently than the Wind Iris suggests. Figure 135 shows the yaw misalignment histogram that is probably closer to the truth.

COLOPHON

This document was typeset using the typographical look-and-feel `classicthesis` developed by André Miede. The style was inspired by Robert Bringhurst's seminal book on typography "*The Elements of Typographic Style*".

Final Version as of April 23, 2015 (version 2.5).